Doctoral Dissertation

Studies on Improving Dynamic Performance of Microgrids by Applying Virtual Synchronous Generator Control to Distributed Generators

劉　佳

Jia Liu

January 2016

Graduate School of Engineering,

Osaka University

Abstract

Recent years, inverter-interfaced distributed generators (DGs) with renewable energy sources (RES), e.g. photovoltaics and wind turbines, have been developed to solve energy crisis and environmental issues. However, the penetration rate of DGs is limited by current regulations and policies, due to concerns about the increased complexity of power system management and protection, and about the lack of inertia support from these inverter-interfaced DGs. To facilitate the integration of DGs in distribution system, the concept of microgrid was proposed. In a microgrid, a cluster of DGs, distributed energy storage systems and loads operate as a single system to reduce the system complexity for the utility and increase the power quality and reliability for local customers. However, inverter-interfaced DGs with conventional control methods, such as droop control, still cannot provide enough inertia to support the frequency of the microgrid. In this dissertation, virtual synchronous generator (VSG) control, a novel control strategy of DG to provide virtual inertia by emulating the swing equation of a synchronous generator (SG), is introduced to inverter-interfaced DGs in microgrids, in order to improve the dynamic performance, especially the transient response of frequency of microgrids.

This dissertation is organized as follows.

In Chapter 1, concepts of inverter-interfaced DGs and microgrids, and major challenges in these emerging technologies are introduced.

In Chapter 2, principles of the basic VSG control are introduced, and other existing control methods providing virtual inertia support are reviewed.

In Chapter 3, VSG control is compared with droop control, which is a conventional DG control method widely adopted in microgrid applications, from the aspect of dynamic characteristics. Two cases are investigated, single inverter operation and parallel operation with a SG. Small-signal models are built to compare transient responses of frequency during a small loading transition, and state-space models are built to analyze oscillation of output active power. Effects of delays in both controls are also studied, and an inertial droop control method is proposed based on the comparison. The results were verified by simulations and experiments. It is shown that VSG control and the proposed inertial droop control inherit the advantages of droop control, and provide extra inertia support for the system.

In Chapter 4, parallel operation of multiple VSGs in microgrids is studied. It is shown that when the basic VSG control is applied, active power oscillation and improper transient active power sharing can be observed. Moreover, the problem of reactive power sharing error, inherited from conventional droop control, should also be addressed to obtain desirable steady-state performance. In this chapter, an enhanced virtual synchronous generator control is proposed, with which oscillation

damping and proper transient active power sharing are achieved by adjusting the virtual stator reactance based on state-space analyses. Furthermore, communication-less accurate reactive power sharing is achieved based on common ac bus voltage estimation. Simulation and experimental results verified the improvement introduced by the proposed enhanced VSG control strategy.

In Chapter 5, a microgrid composed of a VSG and a SG is discussed. Modifications of VSG control are proposed to address specific issues of this kind of microgrids. To prevent unbalanced SG current, double decoupled synchronous reference frame (DDSRF) decomposition and SG negative-sequence current compensation are proposed; and to prevent inverter overcurrent, transient virtual stator impedance is introduced. Tuning methods of main parameters are discussed through theoretical and/or simulation analyses. The effects of the proposed modifications were verified by simulation results, and it is also demonstrated that the presence of VSG alleviates rotor speed deviation of the SG during a loading transition.

In Chapter 6, conclusions are presented and some future challenges are discussed.

Table of Contents

Table of Contents

Chapter 1

Introduction

1.1 Background

Traditional power system is composed of massive power generation plants, in which the primary energy sources are usually from fossil fuels, hydropower or nuclear power, and a centralized transmission and distribution grid, in which the power flow is usually radical and unidirectional in the distribution level.

However, issues of depletion of fossil fuels, geographical and ecological restriction of hydropower and radioactive pollution of nuclear power, have drawn worldwide attentions. Therefore, renewable energy sources (RESs), such as photovoltaics (PVs) and wind turbines, have been considered as the main primary sources of the next generation power system and their penetration ratio in the utility grows year by year. Particularly in Japan, after the Fukushima Daiichi nuclear disaster caused by the Tohoku earthquake and tsunami on 11 March 2011, all nuclear plants have been shut down, which results in a serious shortage of power supply. Therefore, an accelerated growth of RESs is expected in Japan.

Although massive wind farms and PV stations have emerged in recent years, most of RESs are usually of small power ratings (less than 10 MW), and are connected directly to the local distribution network. This kind of generators is called distributed generators (DGs) or distributed energy resources (DERs) [1]. DGs are expected to increase the reliability of the power supply by providing backup power generation for local customers. Meanwhile, as DGs are usually located near the loads, if the penetration ratio of DGs increases, it is expected that the transmission loss can be reduced and the transmission/distribution capacity can be relieved [1]. It should be pointed out that besides of RESs, energy source of DGs may come from other clean energy resources, e.g. gas engines and fuel cells, or even traditional diesel engines.

1.2 Inverter-Interfaced Distributed Generators

1.2.1 Topologies

Most of DGs are equipped with a power-electronics converter at the output terminal, to convert the generated power to desired voltage and frequency. These converters are usually composed of a dc link and two stages: an input-side converter and a grid-side converter, as depicted in Fig. 1.1 [2]. The input-side converter differs according to energy sources and technologies. For example, for PVs and fuel cells, as PV panels and fuel cells offer a low voltage dc output, usually a boost dc-dc converter is needed; whereas for wind turbines and gas engines, an ac-dc rectifier is required. The con-

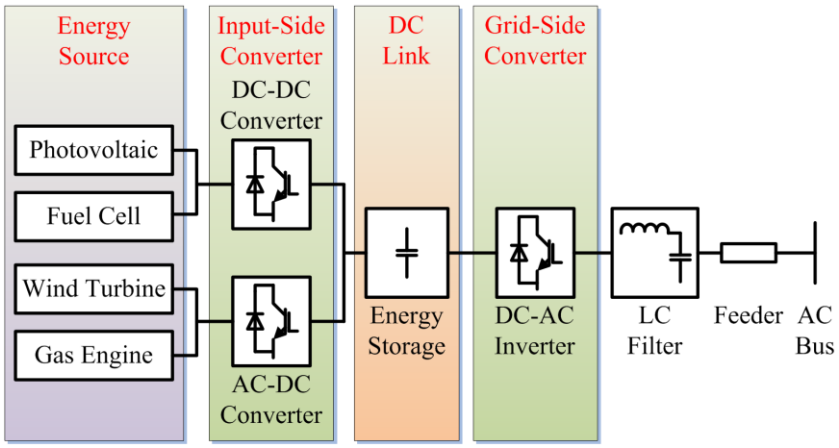

Fig. 1.1 General structure of inverter-interfaced distributed generators.

trol strategy of input-side converter is responsible for the regulation of dc-link or energy source, e.g. maintaining dc-link voltage or tracking the maximum power point.

On the other hand, the grid-side converter is always a dc-ac inverter, no matter what energy source. The control strategy of the grid-side converter is responsible for regulation of generated power, output voltage and frequency and other power quality issues, and is less dependent on the energy source [2]. As a result, this type of DGs can be classified into the same category, called inverter-interfaced DGs.

In most cases, an energy storage system is connected to the dc link, especially for non-dispatchable inverter-interfaced DGs such as wind turbines and photovoltaics, to provide an energy buffer for balancing the active power converted in two stages. The dc-link storage may be an electrolytic capacitor, an electric double-layer capacitor (EDLC) or a battery. A dc-dc converter may be needed for EDLCs and batteries, for conversion of voltage level, regulation of dc-link voltage and/or management of state of charge (SOC).

It should be mentioned that not all DGs are inverter-interfaced DGs. Some DGs can be connected directly or partially directly to the grid. Moreover, some power-electronics-interfaced DGs may only consist of a single stage. These exceptions are not discussed in this dissertation. Furthermore, this dissertation focuses on the control strategy of grid-side converter. In most cases, energy source, input-side converter and energy storage are omitted, and the dc-link is considered as an infinite dc source.

1.2.2 Control Methods

Generally, conventional control methods of the grid-side converter can be classified into two basic types: grid-forming control and grid-feeding control [3].

Grid-forming control is also known as voltage source control or VF control, because it fixes the voltage and frequency at the output terminal to create a voltage source, as shown in Fig. 1.2(a). An

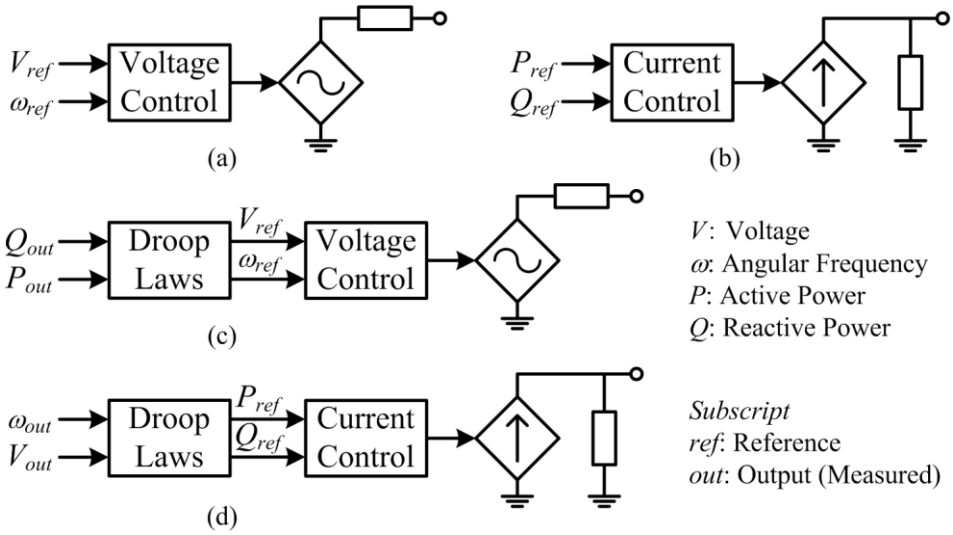

Fig. 1.2 Control methods of grid-side converter. (a) Grid-forming control. (b) Grid-feeding control. (c) Voltage-source-based grid-supporting control. (d) Current-source-based grid-supporting control. [4]

inverter-interfaced DG equipped with this control method is able to form an individual islanded network, but is not suitable for parallel operation with other voltage sources, e.g. with the main grid or with another DG equipped with grid-forming control.

Grid-feeding control is also known as current source control or PQ control, because it controls the output active and reactive power by control the amplitude and phase angle of the current injected into the ac bus, as illustrated in Fig. 1.2(b). Grid-feeding control cannot work individually because it requires a voltage source to provide voltage supporting and phase angle reference. Commonly a phase-locked loop (PLL) is used in this control to synchronize the inverter to the grid. The output active power may be a fixed value for a dispatchable DG, or a variant value determined by maximum power point tracking algorithm of the input-side converter. The output reactive power may be 0 for DGs of unity power factor, and other dispatched value to compensate a known reactive power flow in nearby area.

However, in some applications, e.g. in a microgrid configuration discussed in Section 1.3, multiple DGs are required to operate in both islanded mode and grid-connected mode. Obviously, conventional grid-forming control and grid-feeding control are not competent in this context. Therefore, grid-supporting control is developed to address this issue [3].

In grid-supporting control, usually control laws between frequency and active power, and between voltage and reactive power are predefined in the control strategies, in order to automatically share the active and reactive power between parallel generators. These control laws have been developed in conventional synchronous generator (SG) control, and are adopted for inverters known as droop control [5], [6], because these control laws are generally linear relations with a negative slope.

Grid-supporting control can be further classified into voltage-source-based and current-source-based grid-supporting control. Current-source-based grid-supporting control can be considered as an upgraded grid-feeding control, as its inner control loop is in fact a grid-feeding control, with the added droop control laws only providing automatic power sharing ability, as shown in Fig. 1.2(d). Therefore, like grid-feeding control, DGs with current-source-based grid-supporting control still need to be connected to a voltage source as it cannot provide voltage support for the system.

On the other hand, voltage-source-based grid-supporting control is developed from grid-forming control, as illustrated in Fig. 1.2(c). Therefore, DGs with voltage-source-based grid-supporting control can operate individually owing to the voltage source feature. Moreover, with the added droop control laws, it can even operate in parallel with other voltage sources, no matter whether it is another DG with voltage-source-based grid-supporting control or a fixed voltage source, e.g. the main grid. That is to say, droop control laws provide not only automatic power sharing ability, but also parallel operation ability for a voltage-source-based inverter. Owing to its versatile applicability, voltage-source-based grid-supporting control is arguably the most promising control type for the grid-side converter of inverter-interfaced DGs.

1.2.3 Major Issues

Although the development of DGs is a promising direction of the future "smart grid", the increased penetration of DGs is in fact not friendly to the traditional power system. Major issues caused by inverter-interfaced DGs include the following [1]:

(1) **Unintentional islanding.** Unintentional islanding refers to the situation in which a DG continues to provide power supply for its nearby area unintentionally during a period in which the main grid is not available. It may be dangerous for the utility operators, who may not be aware that the devices are still powered. Moreover, some temporary grid faults can be solved by auto reclosing of relays, and it may become less effective if an unintentional islanding happens. As a result, in current power system regulations, e.g. IEEE Standard 1547 [7], DGs must detect unintentional islanding events and disconnect themselves from the grid. That is to say, DGs cannot be counted as backup power supply during a grid fault under an unintentional islanding.

(2) **Increased complexity of relay protection.** Traditional relay protection in distribution system is designed for a radical configuration. However, the connection of DGs complicates the power flow and makes it bidirectional and unpredictable.

(3) **Lack of inertia.** Traditional power system is supplied mainly by synchronous generators (SGs), which normally have a kinetic energy reservoir in rotating mass. During transient power shortage, this inertia can temporarily provide additional power supply with a fast response, thus maintain the transient frequency. However, inverter-interfaced DGs have very poor inertia. If traditional SGs are gradually replaced by inverter-interfaced DGs, the total inertia of the system will certainly decrease.

A radical solution for the first two issues can be achieved by integrated management of the nearby area of DGs, which is known as the concept of "microgrid" discussed in next section. As for the third one, a promising solution is to apply inverter control methods with virtual inertia, which are presented in detail in Chapter 2.

1.3 Microgrids

1.3.1 Main Concept

The concept of microgrid is originally proposed by Prof. R. H. Lasseter in [8]. In a microgrid, a cluster of DGs, distributed energy storage systems (DESSs) and loads are managed to operate as a single system, as it is illustrated in Fig. 1.3. It is connected to the main grid through a single point, which is called the point of common coupling (PCC), thus it can be considered as a single dispatched load or source by the grid supervisor. Therefore, the system complexity for the utility can be significantly reduced. Loads in a microgrid can be connected to either a dc bus or an ac bus, and can be shed according to a predefined priority in order to guarantee the power supply for sensitive loads.

A microgrid usually has two operation modes: grid-connected mode and islanded mode. During grid-connected mode, the microgrid consumes or supplies a dispatched amount of power through the PCC. If a grid fault happens or the power quality of the grid falls below a predefined level, the microgrid can be switched automatically and seamlessly to islanded mode, i.e., using internal DGs and DESSs to maintain the power supply to internal loads. It should be pointed out that the islanded mode of a microgrid is different from the aforementioned unintentional islanding. It is an intentional islanding which is predictable and under control. Therefore, the power quality and reliability of power supply for local customers can be increased by adopting a microgrid configuration.

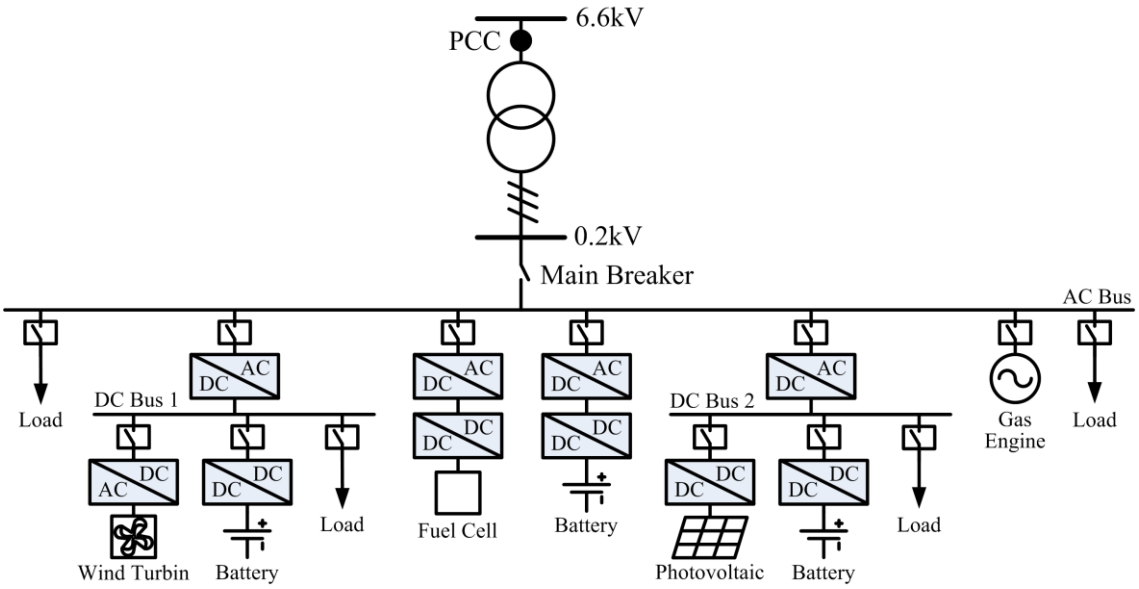

Fig. 1.3 An example of a microgrid configuration.

1.3.2 Control Schemes

The control strategy of a microgrid can be classified into three categories: master-slave control, peer-to-peer control and hierarchical control.

(1) In master-slave control, one DC/AC inverter is chosen as master unit and other inverters are considered as slave units. Grid-feeding control is usually adopted for both master unit and slave units in grid-connected mode. However, in islanded mode, the master unit should be changed into grid-forming control to provide a voltage source for slave units, which are still controlled by grid-feeding control [9]. As a transfer of control method of master unit is inevitable, the transient performances of master-slave control during connection and disconnection are relatively poor. Furthermore, the reliability of master-slave control is also a problem, because the microgrid cannot operate in islanded mode if the master unit is out of service. Another restriction degrading the reliability of microgrid is that communication between the master unit and the main breaker of the microgrid is required.

(2) Peer-to-peer control can be classified into two categories, i.e. with or without communication between inverters. The former is typically based on a multi-agent control scheme [10], [11], and the latter is achieved by applying voltage-source-based grid-supporting control to the inverters [12], [13]. In the peer-to-peer control based on voltage-source-based grid-supporting control, no communication between inverters is required, and no change of inverter control method is needed during microgrid mode transition, because the active and reactive power can be shared coordinately based on the synchronized frequency and local voltage measurement according to the predefined droop control laws. Therefore, communication-less peer-to-peer control is widely adopted in recent microgrid applications.

(3) Hierarchical control is developed from the peer-to-peer control [14], [15]. The primary control level of a hierarchical microgrid control is normally the aforementioned peer-to-peer control installed in inverters, which is responsible for the basic operation of the microgrid. The secondary control and sometimes a tertiary control are installed in a microgrid central controller (MGCC), which usually situates near the main breaker of the microgrid. The secondary control and tertiary control are responsible for optimized operation of the microgrid, e.g., restoring the frequency and voltage deviation, adjusting reactive power sharing error, optimizing power management and controlling power flow at the PCC in grid-connected mode. Communication between MGCC and inverters are required to apply the secondary and tertiary control. However, even during a communication failure, the primary control is still available to maintain the basic operation of the microgrid. In this situation, hierarchical control is downgraded to the aforementioned peer-to-peer control.

1.3.3 Major Challenges

With voltage-source-based grid-supporting control installed in the inverters, the basic operation of a microgrid can be established. However, there are still some challenges to be addressed, in order to achieve better overall performance.

(1) **Proper steady-state active and reactive power sharing.** Generally, active and reactive power is expected to be shared according to the generator power rating ratio in a microgrid. If the microgrid is based on $P-\omega$ and $Q-V$ droop control scheme, the active power can be shared correctly because frequency is auto-synchronized at the output terminal of all inverters in the steady state. However, output voltage may differ due to line voltage drops, which results in inaccurate reactive power sharing. If the microgrid is based on $P-V$ and $Q-\omega$ droop control scheme, the inaccurate power sharing will be observed in active power. In previous studies, this issue is address by improved control schemes at the primary control level [16]–[23], or by adding correction algorithms at secondary control level [24]–[29]. This issue is further discussed in Chapter 4, and a new approach is proposed.

(2) **Transient power sharing.** Even if steady-state power is correctly shared as desired, transient power may not be shared properly due to different dynamic performance of DGs in a microgrid. If this issue is not properly addressed, transient overcurrent may stop inverters. This issue usually occurs during parallel operation of a SG and an inverter-interfaced DG [4], [30], and even during parallel operation of inverters. This issue is discussed in Chapter 4 for the case of parallel inverters, and in Chapter 5 for the case of parallel operation of a SG and an inverter-interfaced DG.

(3) **Frequency and voltage restoration.** As frequency and voltage are drooped against active and reactive power in voltage-source-based grid-supporting control, the deviated frequency and voltage deteriorate power quality of a microgrid. A general approach to address this issue is restoring frequency and voltage by changing the set value of active and reactive power in droop control laws at the secondary control level [13]–[15].

(4) **Optimized power management.** The optimized active and reactive power sharing is not always based on generator power rating ratio. Economic and environmental concerns like fuel consumption and CO_2 emission may require a different power sharing among the DGs. This rearrangement of power sharing can be achieved by changing the set value of active and reactive power in droop control law at the secondary control level [31], [32]. As for reactive power management, a method to fully utilize the power ratings of DGs for reactive power supporting is proposed in [33].

(5) **Unbalanced and nonlinear Load.** When unbalanced and nonlinear loads are connected to a microgrid, proper sharing of negative-sequence and harmonic current becomes important. Additional controllers dedicated to negative-sequence and harmonic current sharing are required, as it is proposed in [34], [35]. Moreover, if a SG is installed in a microgrid, as nega-

tive-sequence and harmonic current will heat the SG, proper control method should be applied in order to prevent negative-sequence and harmonic current in the SG, as it is discussed in Chapter 5.

(6) **Seamless transfer between islanded mode and grid-connected mode.** As mentioned previously, when a grid fault or a deterioration of grid power quality is detected, microgrids should transfer to islanded mode. When high power quality grid power supply is available again, microgrid can be reconnected to the grid through a synchronizing process. The transfer between grid-connected mode and islanded mode should be seamless, i.e. the amplitude, phase, and frequency of bus voltage should be kept stable. This seamless transfer is generally achieved by the secondary or tertiary control in the MGCC, and the synchronizing process is achieved by changing the set value of active and reactive power in droop control laws [14]. An alternative method with less communication requirement is proposed in [36].

(7) **Power flow control in grid-connected mode.** The power flow at the PCC can be controlled to a constant value in grid-connected mode, in order to operate in a grid-friendly manner. This function can be realized at the secondary or tertiary level in the MGCC [14].

(8) **Inertia support.** Conventional voltage-source-based grid-supporting control methods, e.g. droop-control-based methods only emulate the steady-state output characteristics of a SG. The kinetic energy reservoir in the rotating mass of a SG is not emulated in the conventional droop control method. As a result, like most of other inverter control methods, droop control cannot provide enough inertia support. Therefore, a droop-control-based microgrid usually has very poor inertia. After a large disturbance, e.g. connection of a large load or a ground fault, the frequency of microgrid may deviate too fast to be kept within the tolerance by frequency restoration control. Modified droop control method is proposed to address this problem [37]; however, more radical solutions are still expected. Therefore, in this dissertation, a novel voltage-source-based grid-supporting control method, called virtual synchronous generator (VSG) control, mimicking not only the steady-state characteristics of SGs, but also their transient characteristics by applying swing equation, is applied to inverter-interfaced DG, in order to provide inertia support for the microgrid.

1.4 Research Objectives

As it is discussed in the previous parts of this chapter, microgrid is a promising configuration for the integration of DGs into the power system, and voltage-source-based grid-supporting control is currently the most adopted control method for inverter-interfaced DGs in a microgrid. However, conventional voltage-source-based grid-supporting control, e.g. conventional droop control, cannot provide enough inertia support. In this dissertation, the VSG concept is applied to the inverter-interfaced DGs, as shown in Fig. 1.4, in order to enhance the inertia of microgrids and to improve the dynamic performance, especially the transient response of frequency of microgrids. First, it is shown with an analytical approach that VSG control can provide better dynamic performance than

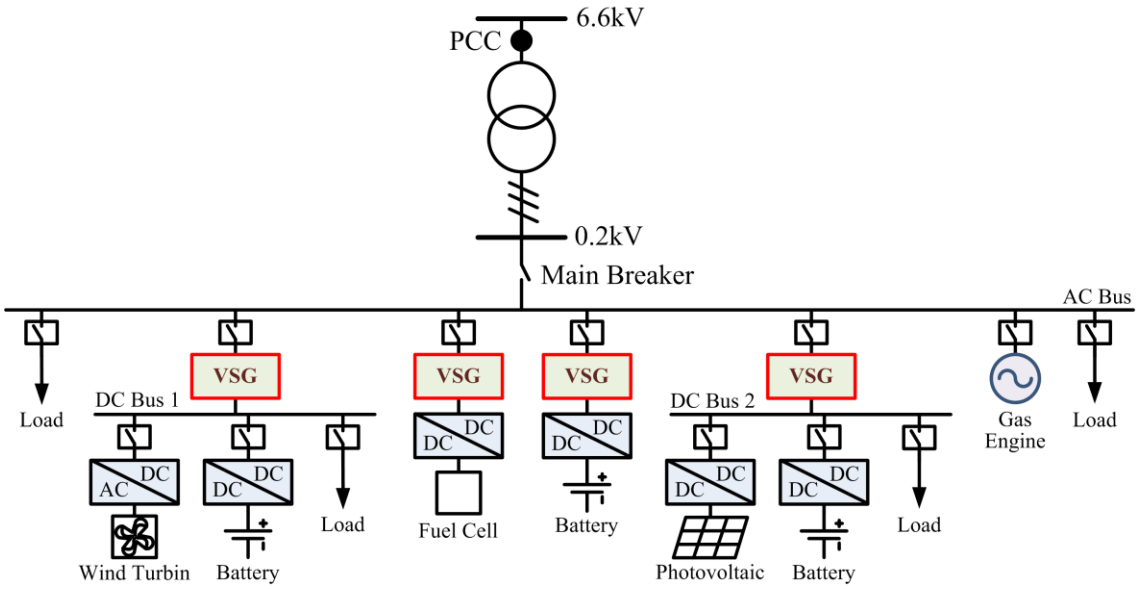

Fig. 1.4 Applying VSG control in a microgrid.

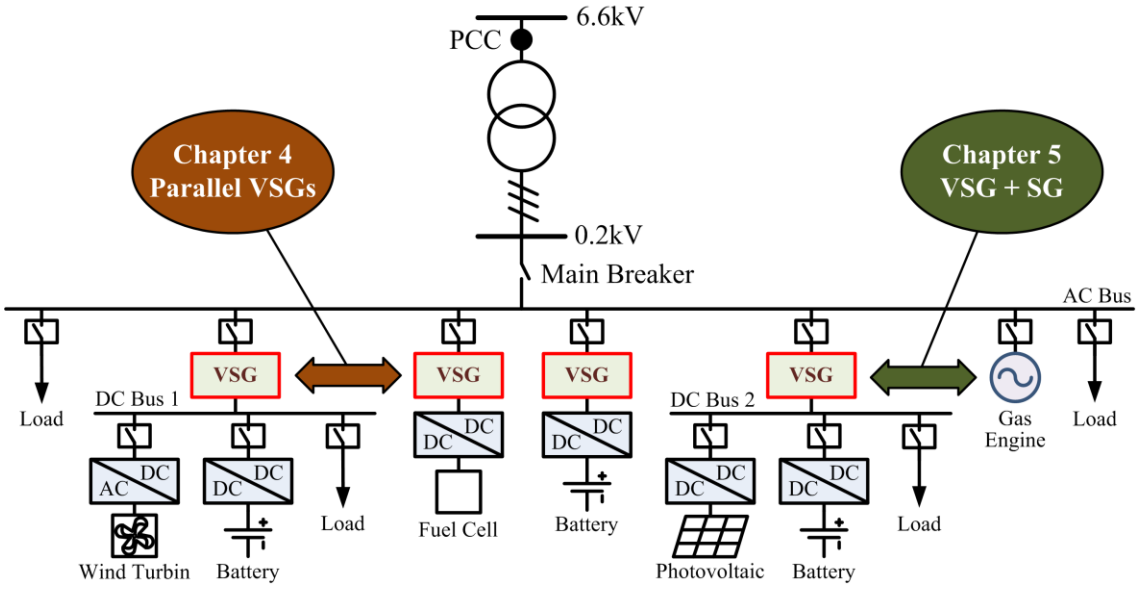

Fig. 1.5 Main themes of Chapter 4 and Chapter 5.

conventional droop control. Afterwards, the operation methods of parallel VSGs and parallel operation of a VSG and a SG are established. Other issues of microgrids, e.g., proper steady-state reactive power sharing, transient power sharing, and unbalanced loading condition are also addressed in this dissertation.

Detailed discussions in following chapters are organized as follows. In Chapter 2, principles of basic VSG control are introduced. In Chapter 3, the dynamic characteristics of VSG are compared with those of droop control, to clarify the advantage and disadvantage of VSG control over conventional inertia-less voltage-source-based grid-supporting control. In Chapter 4 and Chapter 5, parallel

operation of multiple VSGs, and parallel operation of a VSG and a SG are studied, respectively, as it is shown in Fig. 1.5. Special issues introduced by VSG control, such as active power oscillation and transient active power sharing, and other well-known challenges of microgrids, e.g. steady-state reactive power sharing and unbalanced loading condition, are also addressed. With the analyses and the proposed VSG control schemes presented in this dissertation, the basic operation of inertial microgrids based on VSG control can be established.

1.5 Conclusion

In this chapter, the background of this dissertation was introduced. Main concepts, such as inverter-interfaced DG and microgrid were explicated. The control methods equipped in inverter-interfaced DGs and the overall control schemes of microgrids were discussed. Major issues and challenges of inverter-interfaced DGs and microgrids were discussed. Finally, the main research objectives of this dissertation were presented.

References

[1] R. C. Dugan and T. E. McDermott, "Distributed generation," *IEEE Ind. Appl. Mag.*, vol. 8, no. 2, pp. 19–25, Mar./Apr. 2002.

[2] F. Blaabjerg, R. Teodorescu, M. Liserre, and A. V. Timbus, "Overview of control and grid synchronization for distributed power generation systems," *IEEE Trans. Ind. Electron.*, vol. 53, no. 5, pp. 1398–1409, Oct. 2006.

[3] J. Rocabert, A. Luna, F. Blaabjerg, and P. Rodríguez, "Control of power converters in AC microgrids," *IEEE Trans. Power Electron.*, vol. 27, no. 11, pp. 4734–4749, Nov. 2012.

[4] A. D. Paquette and D. M. Divan, "Virtual impedance current limiting for inverters in microgrids with synchronous generators," *IEEE Trans. Ind. Appl.*, vol. 51, no. 2, pp. 1630–1638, Mar./Apr. 2015.

[5] M. C. Chandorkar, D. M. Divan, and R. Adapa, "Control of parallel connected inverters in standalone ac supply systems," *IEEE Trans. Ind. Appl.*, vol. 29, no. 1, pp. 136–143, Jan./Feb. 1993.

[6] K. Debrabandere, B. Bolsens, J. Van den Keybus, A.Woyte, J. Driesen, and R. Belmans, "A voltage and frequency droop control method for parallel inverters," *IEEE Trans. Power Electron.*, vol. 22, no. 4, pp. 1107–1115, Jul. 2007.

[7] IEEE Standard for Interconnecting Distributed Resources with Electric Power Systems, IEEE Standard 1547-2003, Jul. 2003.

[8] R. H. Lasseter, "MicroGrids," in *Proc. 2002 IEEE Power Eng. Soc. Winter Meeting*, pp. 305–308.

[9] B. Zhao, X. Zhang, and J. Chen, "Integrated Microgrid Laboratory System," *IEEE Trans. Power Syst.*, vol. 27, no. 4, pp. 2175–2185, Nov. 2012.

[10] M. E. Baran and I. M. El-Markabi, "A multiagent-based dispatching scheme for distributed generators for voltage support on distribution feeders," *IEEE Trans. Power Syst.*, vol. 22, no. 1, pp. 52–59, Feb. 2007.

[11] A. L. Dimeas and N. D. Hatziargyriou, "Operation of a multiagent system for microgrid control," *IEEE Trans. Power Syst.*, vol. 20, no. 3, pp. 1447–1455, Aug. 2005.

[12] H. Nikkhajoei and R. H. Lasseter, "Distributed generation interface to the CERTS microgrid," *IEEE Trans. Power Del.*, vol. 24, no. 3, pp. 1598–1608, Jul. 2009.

[13] F. Katiraei and M. R. Iravani, "Power management strategies for a microgrid with multiple distributed generation units," *IEEE Trans. Power Syst.*, vol. 21, no. 4, pp. 1821–1831, Nov. 2006.

[14] J. M. Guerrero, J. C. Vasquez, J. Matas, L. G. De Vicuña, and M. Castilla, "Hierarchical control of droop-controlled DC and AC microgrids—A general approach towards standardization," *IEEE Trans. Ind. Electron.*, vol. 58, no. 1, pp. 158–172, Jan. 2011.

[15] A. Bidram and A. Davoudi, "Hierarchical structure of microgrids control system," *IEEE Trans. Smart Grid*, vol. 3, no. 4, pp. 1963–1976, Dec. 2012.

[16] J. He, Y. W. Li, J. M. Guerrero, F. Blaabjerg, and J. C. Vasquez, "An islanding microgrid power sharing approach using enhanced virtual impedance control scheme," *IEEE Trans. Power Electron.*, vol. 28, no. 11, pp. 5272–5282, Nov. 2013.

[17] Y. Zhu, Z. Fang, F. Wang, B. Liu, and Y. Zhao, "A wireless load sharing strategy for islanded microgrid based on feeder current sensing," *IEEE Trans. Power Electron.*, vol. 30, no. 12, pp.6706–6719, Dec. 2015.

[18] Y. W. Li and C.-N. Kao, "An accurate power control strategy for power-electronics-interfaced distributed generation units operating in a low-voltage multibus microgrid," *IEEE Trans. Power Electron.*, vol. 24, no. 12, pp. 2977–2988, Dec. 2009.

[19] Q.-C. Zhong, "Robust droop controller for accurate proportional load sharing among inverters operated in parallel," *IEEE Trans. Ind. Electron.*, vol. 60, no. 4, pp. 1281–1290, Apr. 2013.

[20] C. K. Sao and P. W. Lehn, "Autonomous load sharing of voltage source converters," *IEEE Trans. Power Del.*, vol. 20, no. 2, pp. 1009–1016, Apr. 2005.

[21] C-.T. Lee, C-.C. Chu, and P-.T. Cheng, "A new droop control method for the autonomous operation of distributed energy resource interface converters," *IEEE Trans. Power Electron.*, vol. 28, no. 4, pp. 1980–1993, Apr. 2013.

[22] E. Rokrok and M. E. H. Golshan, "Adaptive voltage droop scheme for voltage source converters in an islanded multibus microgrid," *IET Gener. Transm. Distrib.*, vol. 4, no. 5, pp. 562–578, May 2010.

[23] H. Xu, X. Zhang, F. Liu, R. Shi, C. Yu, W. Zhao, Y. Yu, and W. Cao, "A reactive power sharing method based on virtual capacitor in islanding microgrid," in *Proc. Int. Power Electron. Conf. (IPEC-Hiroshima ECCE-Asia)*, 2014, pp. 567–572.

[24] J. He and Y. W. Li, "An enhanced microgrid load demand sharing strategy," *IEEE Trans. Power Electron.*, vol. 27, no. 9, pp. 3984–3995, Sept. 2012.

[25] J. He, Y. W. Li, and F. Blaabjerg, "An enhanced islanding microgrid reactive power, imbalance power, and harmonic power sharing scheme," *IEEE Trans. Power Electron.*, vol. 30, no. 6, pp. 3389–3401, Jun. 2015.

[26] H. Mahmood, D. Michaelson, and J. Jiang, "Accurate reactive power sharing in an islanded microgrid using adaptive virtual impedances," *IEEE Trans. Power Electron.*, vol. 30, no. 3, pp. 1605–1617, Mar. 2015.

[27] H. Han, Y. Liu, Y. Sun, M. Su, and J. M. Guerrero, "An improved droop control strategy for reactive power sharing in islanded microgrid," *IEEE Trans. Power Electron.*, vol. 30, no. 6, pp. 3133–3141, Jun. 2015.

[28] Q. Shafiee, J. M. Guerrero, and J. C. Vasquez, "Distributed secondary control for islanded microgrids — a novel approach," *IEEE Trans. Power Electron.*, vol. 29, no. 2, pp. 1018–1031, Feb. 2014.

[29] A. Micallef, M. Apap, C. Spiteri-Staines, J. M. Guerrero, and J. C. Vasquez, "Reactive power sharing and voltage harmonic distortion compensation of droop controlled single phase islanded microgrids," *IEEE Trans. Smart Grid*, vol. 5, no. 3, pp. 1149–1158, May 2014.

[30] A. D. Paquette, M. J. Reno, R. G Harley, and D. M. Divan, "Sharing transient loads: causes of unequal transient load sharing in islanded microgrid operation," *IEEE Ind. Appl. Mag.*, vol. 20, no. 2, pp. 23–34, Mar./Apr. 2014.

[31] C. A Hernandez-Aramburo, T. C. Green, and N. Mugniot, "Fuel consumption minimization of a microgrid," *IEEE Trans. Ind. Appl.*, vol. 41, no. 3, pp. 673–681, May/Jun. 2005.

[32] E. Barklund, N. Pogaku, M. Prodanovic, C. Hernandez-Aramburo, and T.C. Green, "Energy management in autonomous microgrid using stability-constrained droop control of inverters," *IEEE Trans. Power Electron.*, vol. 23, no. 5, pp. 2346–2352, Sept. 2008.

[33] A. Milczarek, M. Malinowski, and J. M. Guerrero, "Reactive power management in islanded microgrid—proportional power sharing in hierarchical droop control," *IEEE Trans. Smart Grid*, vol. 6, no. 4, pp. 1631–1638, Jul. 2015.

[34] M. B. Delghavi and A. Yazdani, "Islanded-mode control of electronically coupled distributed-resource units under unbalanced and nonlinear load conditions," *IEEE Trans. Power Del.*, vol. 26, no. 2, pp. 661–673, Apr. 2011.

[35] Q.-C. Zhong, "Harmonic droop controller to reduce the voltage harmonics of inverters," *IEEE Trans. Ind. Electron.*, vol. 60, no. 3, pp. 936–945, Mar.2013.

[36] Y. Jia, D. Liu, and J. Liu, "A novel seamless transfer method for a microgrid based on droop characteristic adjustment," in *Proc. 7th Int. Power Electron. and Motion Control Conf.*, 2012, pp. 362–367.

[37] N. Soni, S. Doolla, and M. C. Chandorkar, "Improvement of transient response in microgrids using virtual inertia," *IEEE Trans. Power Del.*, vol. 28, no. 3, pp. 1830–1838, Jul. 2013.

Chapter 2

Principles of Virtual Synchronous Generator Control

2.1 Introduction

In this chapter, principles of VSG control schemes are introduced, beginning with the swing equation of a real SG shown in Section 2.2. The basic VSG control scheme proposed by Ise Laboratory, Osaka University, from which the control methods in this dissertation are developed, is discussed in detail in Section 2.3. A brief survey of other existing inverter-interfaced DG control methods with virtual inertia support is presented in Section 2.4.

2.2 Swing Equation of a Synchronous Generator

Fig. 2.1 illustrates the dynamic model of a synchronous generator connected to an infinite bus. The input power P_{in} is provided by the shaft torque T_m as shown in (2.1).

$$P_{in} = T_m \omega_m, \tag{2.1}$$

where ω_m is the angular frequency of the rotor. In this dissertation, it is assumed that the number of pairs of poles is 1.

The relation between output power P_{out} and the input power P_{in} is written as

$$P_{in} - P_{out} = J\omega_m \frac{\mathrm{d}\omega_m}{\mathrm{d}t} + D(\omega_m - \omega_g), \tag{2.2}$$

where ω_g is the angular frequency of the bus, J is the moment of inertia of rotating mass, and D is the damping factor of the damping power introduced by the damp winding, which depends on the power angle δ and SG impedance parameters as shown in (2.3) [1].

$$D = V_{bus}^2 \left[\frac{T''_d X'_d (X'_d - X''_d)}{X''_d (X'_d + X_{line})^2} \sin^2\delta + \frac{T''_q X'_q (X'_q - X''_q)}{X''_q (X'_q + X_{line})^2} \cos^2\delta \right], \tag{2.3}$$

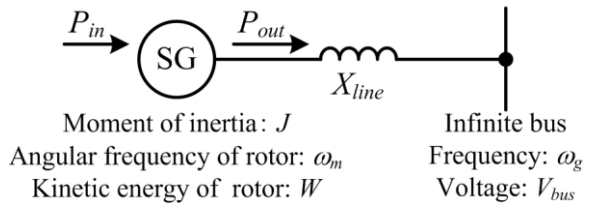

Fig. 2.1 Dynamic model of synchronous generator.

where V_{bus} is the amplitude of bus voltage, X_{line} is the line reactance, X'_d, X''_d, X'_q, X''_q are the d-axis and q-axis transient and sub-transient reactance of the SG, respectively, T''_d and T''_q are the d-axis and q-axis sub-transient short-circuit time constant of the SG, respectively. Knowing that (2.3) is only valid if mechanical losses are neglected and the rotor flux linkage is fixed. The latter is not true if automatic voltage regulator (AVR) is applied. However, (2.3) can be still used to obtain an approximate value.

Equation (2.2) is known as swing equation, which describes the inertia feature of a traditional SG. The kinetic energy W stored in the rotating mass can be deduced as

$$W = \frac{1}{2} J \omega_m^2. \tag{2.4}$$

This kinetic energy reservoir is essential for the transient power balance between P_{in} and P_{out}. According to the swing equation shown in (2.2), if $P_{in} > P_{out}$, ω_m increases, and W increases, the surplus generated power is stored in the rotating mass. If $P_{in} < P_{out}$, ω_m decreases, and W decreases, the stored kinetic energy is fed into the power system to compensate transient power shortage. In steady state, $\omega_m = \omega_g$ and $\mathrm{d}\omega_m/\mathrm{d}t = 0$; therefore, $P_{in} = P_{out}$.

2.3 Basic Virtual Synchronous Generator Control Developed by Ise Laboratory

2.3.1 Control Scheme

Fig. 2.2 shows the basic virtual synchronous generator (VSG) control scheme, developed through [2], [3] by the research team in Ise Laboratory, Osaka University.

The key idea of the VSG control is to emulate the swing equation in the block "Swing Equation Function" in Fig. 2.2. For simplification, the damping factor D is considered as a constant parameter. This simplification does not affect the basic principle of the swing equation. As an inverter does

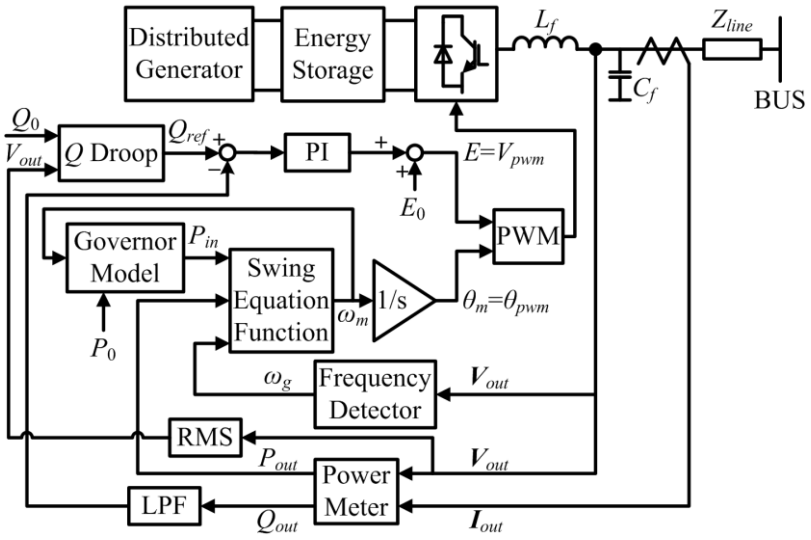

Fig. 2.2 Block diagram of the basic VSG control scheme.

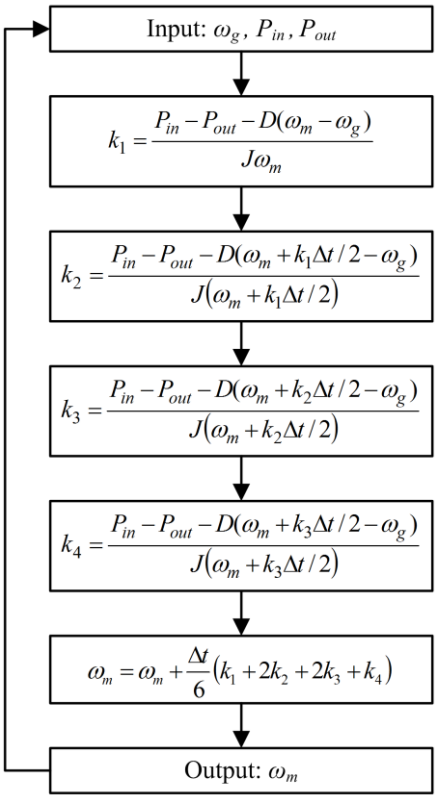

Fig. 2.3 Flow chart of solving swing equation by Runge-Kutta method.

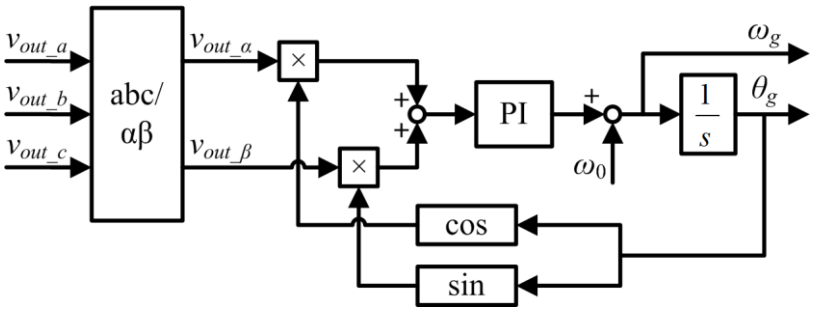

Fig. 2.4 Block diagram of the "Frequency Detector" block of the basic VSG control.

not really have a rotating mass, the moment of inertia J and the damping factor D are in fact virtual parameters defined in the inverter control program.

As the swing equation (2.2) is a differential equation, an algorithm based on Runge-Kutta iterative method is adopted to solve the virtual rotor angular frequency ω_m from (2.2), as shown in Fig. 2.3. The calculated ω_m provides the frequency reference for the governor model and the PWM inverter phase reference θ_{pwm} through an integrator.

The kinetic energy stored in the rotating mass expressed in (2.4) is emulated by the energy storage, which performs as an energy buffer between the input power generated by the DG and the output power distributed to the ac bus. Normally the energy storage is a capacitor. An electric dou-

ble-layer capacitor (EDLC) or a battery can be optionally used combined with the capacitor if large capacity is required.

The block "Frequency Detector" is responsible for the detection of bus frequency ω_g. In this dissertation, a conventional phase-locked loop (PLL) is used to trace the frequency of output voltage $\boldsymbol{V}_{out}$, as shown in Fig. 2.4. The transformation from three-phase components to αβ-frame components is executed through the pre-multiplication by the transformation matrix $\boldsymbol{T}_{abc/\alpha\beta}$ defined as follows.

$$\boldsymbol{T}_{abc/\alpha\beta} = \sqrt{\frac{2}{3}} \cdot \begin{bmatrix} 1 & -\frac{1}{2} & -\frac{1}{2} \\ 0 & \frac{\sqrt{3}}{2} & -\frac{\sqrt{3}}{2} \end{bmatrix} \tag{2.5}$$

It should be pointed out that in transient state, the frequency of output voltage may differ from the bus frequency, especially if the line impedance Z_{line} is very large. However, measurement of bus voltage is usually difficult as the inverter may be installed far away from the ac bus of the microgrid. Normally, the influence of this compromise can be neglected as the line impedance Z_{line} in a microgrid is usually small.

In the block "Power Meter", the output active and reactive power P_{out} and Q_{out} are calculated through (2.6) and (2.7).

$$P_{out} = v_{out\_a} i_{out\_a} + v_{out\_b} i_{out\_b} + v_{out\_c} i_{out\_c} \tag{2.6}$$

$$Q_{out} = \frac{1}{\sqrt{3}} [i_{out\_a}(v_{out\_b} - v_{out\_c}) + i_{out\_b}(v_{out\_c} - v_{out\_a}) + i_{out\_c}(v_{out\_a} - v_{out\_b})] \tag{2.7}$$

The line-to-line RMS value of output voltage is calculated through (2.8) in the block "RMS".

$$V_{out} = \sqrt{v_{out\_a}^2 + v_{out\_b}^2 + v_{out\_c}^2} \tag{2.8}$$

The block "Governor Model" is an $\omega - P$ droop controller, as shown in Fig. 2.5, where ω_0 is the nominal angular frequency, P_0 is the set value of active power, k_p is the $\omega - P$ droop

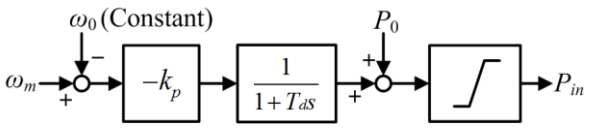

Fig. 2.5 Block diagram of the "Governor Model" block of the basic VSG control.

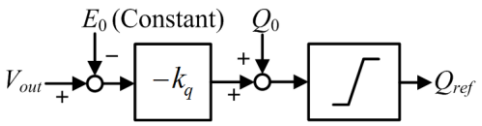

Fig. 2.6 Block diagram of the "*Q* Droop" block of the basic VSG control.

coefficient, and T_d is the time constant of governor delay used to emulate the delayed mechanical response of a real governor of SG. The range of the output limiter for P_{in} is –0.05 ~ 1.05 pu. Fig. 2.5 can be expressed as

$$P_{in} = P_0 - \frac{k_p}{1 + T_d s}(\omega_m - \omega_0). \tag{2.9}$$

The block "Q Droop" is an $V - Q$ droop controller, as shown in Fig. 2.6, where E_0 is the nominal voltage, Q_0 is the set value of reactive power, and k_q is the $V - Q$ droop coefficient. The range of the output limiter for Q_{ref} is –1 ~ 1 pu. Fig. 2.6 can be expressed as

$$Q_{ref} = Q_0 - k_q(V_{out} - E_0). \tag{2.10}$$

The "Governor Model" block creates the linear droop control law between active power and the frequency, and the "Q Droop" block creates the linear droop control law between reactive power and the voltage. As this VSG control operates as a voltage source, it can be classified as a voltage-source-based grid-supporting control discussed in Section 1.2.2. That is to say, like other voltage-source-based grid-supporting controls, VSG-control-based inverter can operate individually, in parallel, and even be connected to the power grid directly, and no change of control is needed during operation mode transitions. Therefore, the VSG control can be considered as an upgraded voltage-source-based grid-supporting control which is able to provide inertia support.

A Proportional-Integral (PI) controller is used to track the output reactive power to the reference value Q_{ref} generated by the "Q Droop" controller. In order to diminish the influence from ripples in measured output power, a 20Hz first-order low-pass filter is applied for Q_{out} as shown in Fig. 2.2. As the output current is measured after the LC filter stage, the reactive power consumed by the LC filter is not included in Q_{out}. Therefore, no specific initial process is required for the reactive power PI controller. The output voltage of PWM inverter V_{pwm} is obtained from the sum of the PI controller output and the nominal voltage E_0. The function of this PI controller is similar to the automatic reactive power regulators (AQR) of the SG, in which the electromotive force (emf) is controlled by regulating the field current. Therefore, the output voltage V_{pwm} can be considered as the virtual internal emf E of the VSG.

It is noteworthy that inner current or voltage loop is not adopted in this control scheme, in order to make the filter inductor L_f contribute to the output impedance and be considered as the stator inductance of the VSG (Note that the filter capacitor C_f is usually negligible at fundamental frequency). This stator inductance results in more inductive output impedance, which is especially important for active and reactive power decoupling in a low voltage microgrid where line resistance is dominant. (Detailed discussion on the active and reactive power decoupling is presented in Section 3.3.1.) Nevertheless, output voltage is still regulated indirectly by the $V - Q$ droop controller and the PI controller of reactive power.

Contrarily, in conventional voltage-source-based grid-supporting control, usually an inner voltage loop is adopted; and in conventional current-source-based grid-supporting control, usually an inner current loop is adopted, as it is discussed in Section 3.2.1. In this case, the LC filter stage is the control plant of the inner voltage/current loop and cannot be counted into the output impedance. Therefore, the output impedance is purely the resistive line impedance. Although methods like virtual impedance have been proposed to address this issue, the output impedance design in conventional voltage/current-source-based grid-supporting control is more difficult than the VSG control. Detailed discussion on this point is presented in Section 4.4.

2.3.2 Per Unit Transformation

In this dissertation, to simplify explications and to facilitate comparisons between inverters of different ratings, some control and hardware parameters are given in per unit values calculated based on respective power ratings of DGs.

The moment of inertia J is given in inertia constant M^* (in second), defined as

$$M^* = \frac{J\omega_0^2}{S_{base}}, \tag{2.11}$$

where S_{base} is the power rating of the DG.

The damping factor D is given in per unit value D^*, defined as

$$D^* = \frac{D\omega_0}{S_{base}}, \tag{2.12}$$

where superscript "$*$" indicates per unit value.

The $\omega - P$ and $V - Q$ droop coefficients k_p and k_q are given in per unit values k_p^* and k_q^*, respectively, defined as

$$k_p^* = \frac{k_p\omega_0}{S_{base}}, \tag{2.13}$$

$$k_q^* = \frac{k_qE_0}{S_{base}}. \tag{2.14}$$

The set values of active and reactive power P_0 and Q_0 are given in per unit values P_0^* and Q_0^*, respectively, defined as

$$P_0^* = \frac{P_0}{S_{base}}, \tag{2.15}$$

$$Q_0^* = \frac{Q_0}{S_{base}}. \tag{2.16}$$

In a microgrid, in order to share the active and reactive power according to the generator power ratings ratio without communication, k_p^*, k_q^*, P_0^* and Q_0^* should be designed equally for each DG in default [4].

The PI controller is defined as (2.17) in this dissertation, and the PI gain K_p is given in per unit value, which means the gain of output in per unit value over input in per unit value. The PI time constant T_i is given in second.

$$G(s) = K_p(1 + \frac{1}{T_i s}) \tag{2.17}$$

The per unit value of impedance $Z = R + jX$ is defined as follows.

$$Z^* = \frac{ZS_{base}}{E_0^2}, \tag{2.18}$$

$$R^* = \frac{RS_{base}}{E_0^2}, \tag{2.19}$$

$$X^* = \frac{XS_{base}}{E_0^2}, \tag{2.20}$$

where R, X are the resistance and reactance, respectively.

2.3.3 Variations of Virtual Synchronous Generator Control

Some variations of the basic VSG control have been proposed to improve the performance and/or address a specific issue. A study on parallel operation of VSGs is presented in [5]. A sophisticated damping method is presented in [6] to increase the active power damping during grid-connected mode under complicated line impedance condition. This problem is also addressed by the method of alternating moment of inertia [7]. Particle swarm optimization (PSO) is proposed to tune the parameter of VSGs in a microgrid consisting of multiple VSGs [8], and a modification of VSG for voltage sag ride-through is presented in [9]. Besides, VSG control can also be used to improve the performance of a traditional SG, as it is proposed in [10], in which VSG is applied to control the grid-side converter.

2.4 Other Existing Inverter Control Methods with Virtual Inertia

The concept of VSG was originally proposed in [11] and has attracted a lot of attention from all over the world. Besides of the VSG control discussed in Section 2.3, several other control methods using virtual inertia have also been developed [12]. In this section, a brief survey of several typical examples is presented, and comparisons between these methods and the VSG control introduced in Section 2.3 are discussed.

2.4.1 VSG Control Developed by VSYNC Project

The VSYNC project under the 6th European Research Framework program is the first research team trying to use virtual inertia control for inverters [11], and their control methods have been developed through [13]–[22]. As the principle of VSYNC project is to regulate the grid frequency, their works focus more on the DESSs rather than DGs, as it is depicted in Fig. 2.7(a).

It can be concluded that this control scheme is a current-source-based grid-supporting control as a current control loop is applied at the output terminal. A PLL unit is used to detect the frequency of the grid and to provide angle reference for the dq transformation. The detailed calculation of current reference based on active and reactive power reference is shown in Fig. 2.7(b). Compared with the basic VSG control discussed in Section 2.3, it can be noticed that the coefficient $K_{inertia}$ in Fig. 2.7(b) is analogous to the virtual inertia J in (2.2), the coefficient K_f is analogous to the $\omega - P$

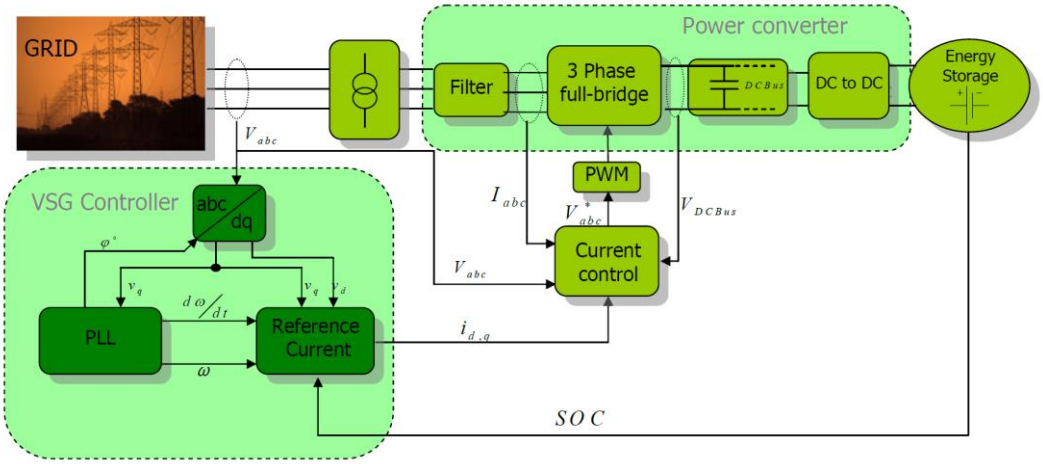

(a)

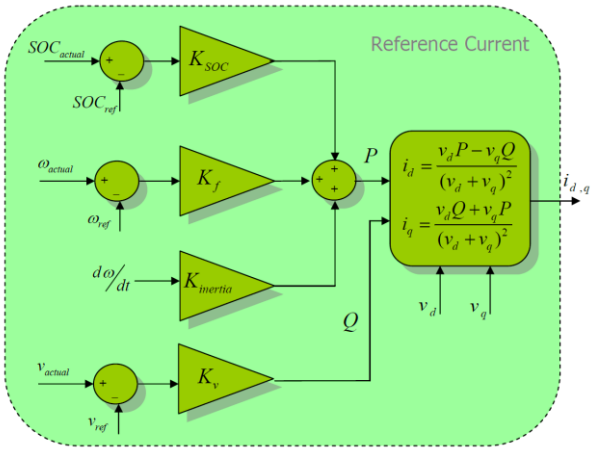

(b)

Fig. 2.7 Typical VSG control scheme developed by VSYNC project [19].
(a) Overall control scheme. (b) Calculation of Reference Current.

droop coefficient k_p in (2.9) and the coefficient K_v is analogous to the $V-Q$ droop coefficient k_q in (2.10). A unique parameter K_{soc} is proposed to share the SOC between parallel DESSs. However, the damping factor is not included in this control scheme. Besides, this control scheme is not suitable for islanded operation without a voltage source reference.

2.4.2 VISMA Control Developed by IEPE

Another inverter control method using virtual inertia is called virtual synchronous machine (VISMA) developed by the Institute of Electrical Power Engineering (IEPE), Clausthal University of Technology, Germany [23]–[28]. Two control methods of VISMA are proposed, one is a current-source-based method, and the other is a voltage-source-based method [27], as illustrated in Figs. 2.8 and 2.9, respectively.

In current-source-based VISMA control, a hysteresis current controller is used to control the

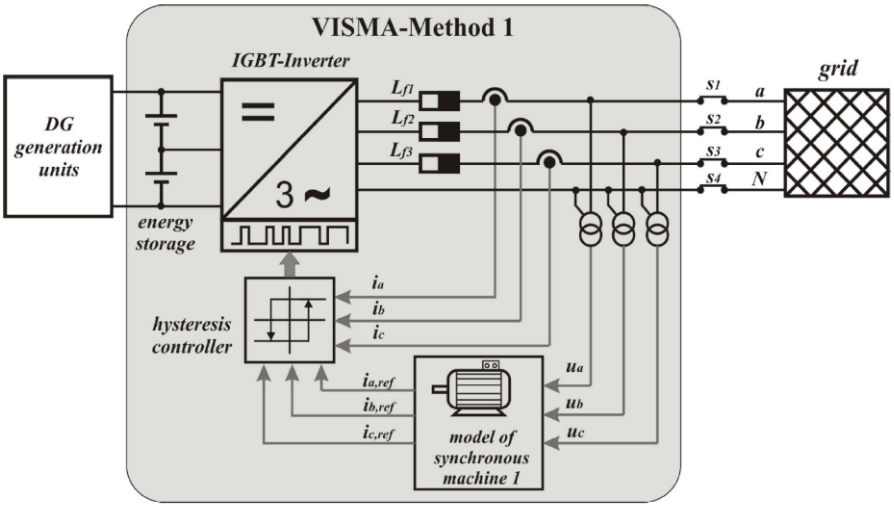

(a)

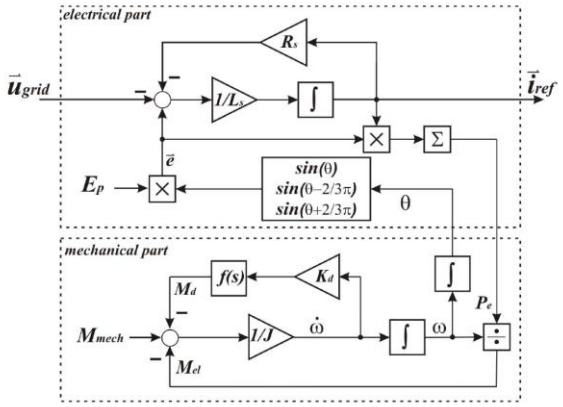

(b)

Fig. 2.8 Current-source-based VISMA control [27].

(a) Overall control scheme. (b) Model of synchronous machine 1.

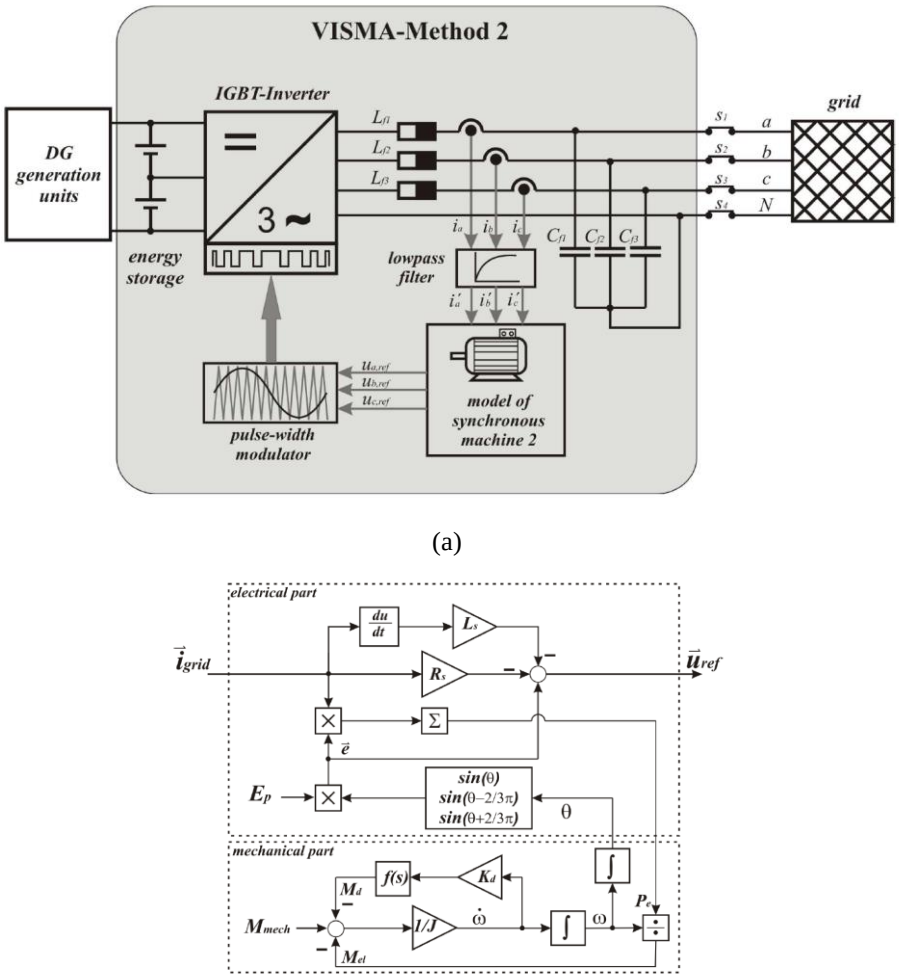

(a)

(b)

Fig. 2.9 Voltage-source-based VISMA control [27].

(a) Overall control scheme. (b) Model of synchronous machine 2.

output current, whereas the voltage-source-based VISMA control uses open-loop voltage source control. Stator impedance models including L_s and R_s are calculated in both control methods in an opposite way, and the mechanical parts in both control methods are the same. M_{mech}, M_{el}, and M_d indicate the mechanical torque, electrical torque and the damping torque, respectively. The virtual inertia J has the same function as that introduced in Section 2.3, but the damping power is emulated in a different way. As droop control laws are not included in both two VISMA control methods, both VISMA controls may not be suitable for parallel operation of inverters. In fact, the voltage-source-based VISMA control can be considered as an upgraded grid-forming control, and the current-source-based VISMA control can be considered as an upgraded grid-feeding control.

2.4.3 VSG Control Developed by KHI

Kawasaki Heavy Industries (KHI) is also an active research group in the area of VSG control. KHI has developed VSG control for both three-phase and single-phase inverters [29]–[31]. The basic

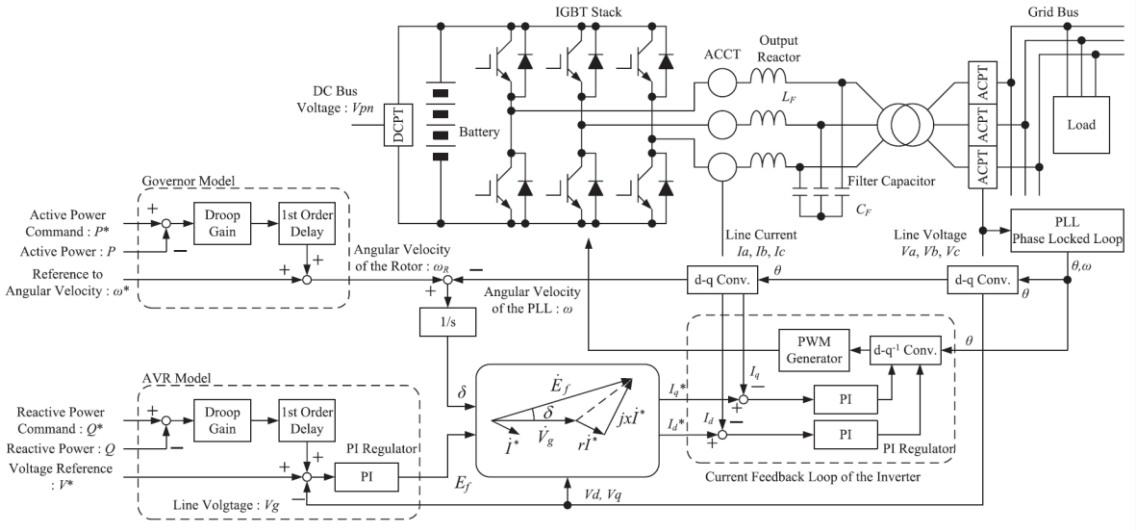

(a)

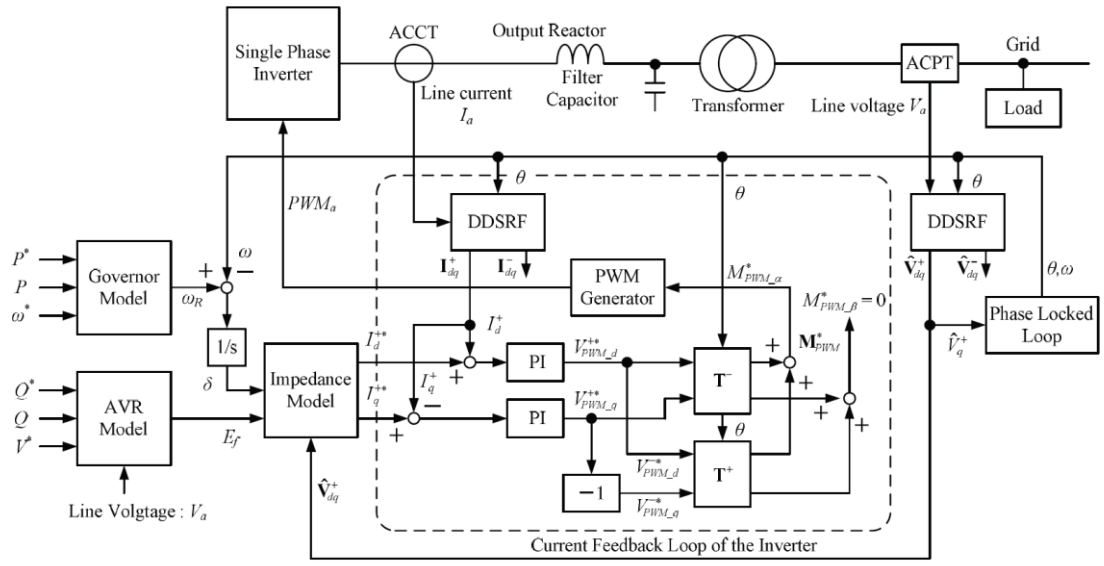

(b)

Fig. 2.10 VSG control developed by KHI

(a) for a three-phase inverter [29], and (b) for a single-phase inverter [30].

VSG control scheme by KHI for a three-phase inverter is shown in Fig. 2.10(a) [29], and that for single-phase inverter is shown in Fig. 2.10(b) [30], which is an adapted version based on double de-coupled synchronous reference frame (DDSRF) decomposition.

As it is depicted in Fig. 2.10(a), the VSG control by KHI is based on dq transformation, in which the phase angle information is acquired by a PLL unit. The Govornor Model and AVR Model in Fig. 2.10(a) create the droop control laws, and a current control loop is presented at the output terminal. Therefore, the VSG control by KHI is a current-source-based grid-supporting control. It should be

pointed out that the inputs and outputs of the droop control laws are opposite to the basic VSG control in Section 2.3, i.e. the inputs are active and reactive power and the outputs are frequency and voltage. In this type of droop control laws, a first-order delay can be used to emulate the inertia. Detailed discussion on this point is presented in Chapter 3. Besides, impedance model is also included in KHI's VSG control, to emulate the stator impedance of a SG.

2.4.4 Synchronverter

Another well-known inertial inverter control is called synchronverter, proposed by Prof. Q.-C. Zhong for three-phase inverter in [32], [33], and have been furtherly developed and applied in single-phase inverter [34], three-phase PWM rectifier [35], static synchronous compensator (STATCOM) [36], and HVDC system [37], [38]. The basic topology and control scheme of the original synchronverter for a three-phase inverter are shown in Fig. 2.11 [33]. The formulas of the electromagnetic torque e, the reactive power Q and the electromagnetic torque T_e in the central block of Fig. 2.11(b) are as follows.

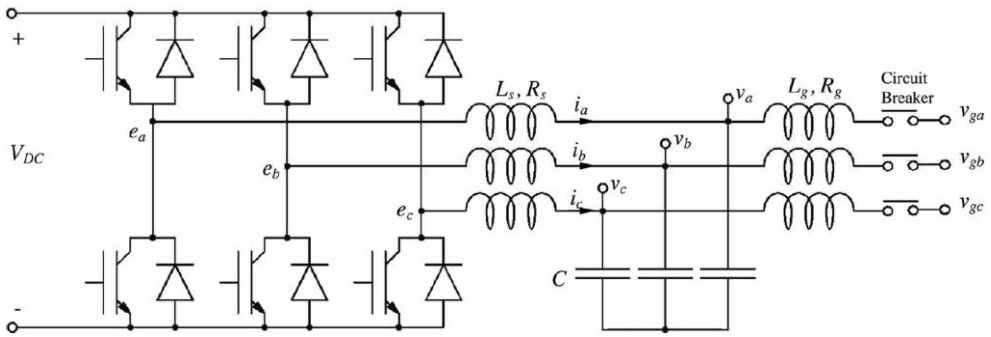

(a)

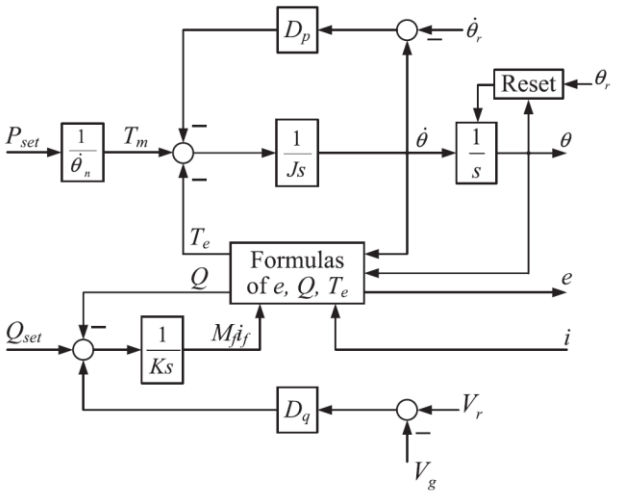

(b)

Fig. 2.11 (a) Synchronverter topology and (b) synchronverter control scheme [33].

$$e = \dot{\theta} M_f i_f \widetilde{\sin}\theta, \tag{2.21}$$

$$T_e = M_f i_f \langle i, \widetilde{\sin}\theta \rangle, \tag{2.22}$$

$$Q = -\dot{\theta} M_f i_f \langle i, \widetilde{\cos}\theta \rangle, \tag{2.23}$$

where i_f is the field excitation current, M_f is the maximum mutual inductance between the stator windings and the field winding. $\dot{\theta}$ is the virtual angular speed of the machine and also the frequency of the control signal e sent to the pulse width modulation (PWM) generator, and i is the stator current (vector) flowing out of the machine. $\widetilde{\sin}\theta$ and $\widetilde{\cos}\theta$ are defined as

$$\widetilde{\sin}\theta = \begin{bmatrix} \sin\theta \\ \sin(\theta - \frac{2}{3}\pi) \\ \sin(\theta + \frac{2}{3}\pi) \end{bmatrix}, \tag{2.24}$$

$$\widetilde{\cos}\theta = \begin{bmatrix} \cos\theta \\ \cos(\theta - \frac{2}{3}\pi) \\ \cos(\theta + \frac{2}{3}\pi) \end{bmatrix}. \tag{2.25}$$

The upper part of Fig. 2.11(b) can be expressed as

$$\ddot{\theta} = \frac{1}{J}\left[T_m - T_e - D_p\left(\dot{\theta} - \dot{\theta}_r\right)\right], \tag{2.26}$$

where T_m is the mechanical torque applied to the rotor, J is the imaginary moment of inertia, D_p is the mechanical friction coefficient and $\dot{\theta}_r$ is the frequency reference.

The principles of synchronverter are actually very similar to the basic VSG control introduced in Section 2.3, except that the damping power introduced by the damp winding is not emulated in the synchronverter control. The mechanical friction D_p and voltage droop coefficient D_q are analogous to the droop coefficients k_p and k_q in Section 2.3, respectively. Therefore, the synchronverter control is also a voltage-source-based grid-supporting control method.

2.4.5 Other Typical Virtual Inertia Control Methods

Besides of abovementioned research groups, several other virtual inertia control methods have been developed. Similar to the VSYNC project, some researchers focus on the kinetic energy only and therefore propose virtual inertia control methods for DESSs [39]–[40]. Some virtual inertia control methods for inverter-interfaced DGs are based on modifications on droop control, e.g. adding a first-order delay [41], [42] or modifying the $P - \omega$ droop coefficient [43]. However, in [41], [42], the angular frequency of the bus ω_g, which provides the synchronous frequency for damping power calculation in (2.2), is replaced by a constant value, i.e., nominal frequency ω_0, thus the damping

factor D becomes equivalent to droop coefficient k_p. This modification of swing equation results in a simpler model, and as a result, the dedicated governor can even be omitted, as it is presented in [42]. In this case, however, no damping effect caused by damper winding is emulated, which may result in larger output power oscillation.

2.5 Conclusion

In this chapter, principles of VSG controls were introduced. The basic VSG control developed by Ise Laboratory was presented in detail, and other inverter control methods providing virtual inertia were briefly reviewed.

References

[1] J. Machowski, J. Bialek, and J. R. Bumby, *Power System Dynamics and Stability*. New York: John Wiley & Sons, 1997, pp. 141–182.

[2] K. Sakimoto, Y. Miura, and T. Ise, "Stabilization of a power system including inverter type distributed generators by the virtual synchronous generator," *IEEJ Trans. Power and Energy*, vol. 132, no. 4, pp. 341–349, Apr. 2012 (in Japanese). or *Electrical Engineering in Japan*, vol. 187, no. 3, pp. 7–17, May 2014 (in English).

[3] T. Shintai, Y. Miura, and T. Ise, "Reactive power control for load sharing with virtual synchronous generator control," in *Proc. 7th Int. Power Electron. Motion Control Conf.*, 2012, pp. 846–853.

[4] J. Rocabert, A. Luna, F. Blaabjerg, and P. Rodríguez, "Control of power converters in AC microgrids," *IEEE Trans. Power Electron.*, vol. 27, no. 11, pp. 4734–4749, Nov. 2012.

[5] K. Sakimoto, Y. Miura, and T. Ise, "Characteristics of parallel operation of inverter-type distributed generators operated by a virtual synchronous generator," *IEEJ Trans. Power and Energy*, vol. 133, no. 2, pp. 186–194, Feb. 2013 (in Japanese). or *Electrical Engineering in Japan*, vol. 192, no. 4, pp. 9–19, Sep. 2015 (in English).

[6] T. Shintai, Y. Miura, and T. Ise, "Oscillation damping of a distributed generator using a virtual synchronous generator," *IEEE Trans. Power Del.*, vol. 29, no. 2, pp. 668–676, Apr. 2014.

[7] J. Alipoor, Y. Miura, and T. Ise, "Power system stabilization using virtual synchronous generator with alternating moment of inertia," *IEEE J. Emerg. Sel. Topics Power Electron.*, vol. 3, no. 2, pp. 451–458, Jun. 2015.

[8] J. Alipoor, Y. Miura, and T. Ise, "Optimazation of microgrid with multiple VSG units," 電気学会電力技術・電力系統技術合同研究会, PE–14–125, PSE–14–125, pp.51–56 (2014).

[9] J. Alipoor, Y. Miura, and T. Ise, "Voltage sag ride-through performance of Virtual Synchronous Generator," in *Proc. Int. Power Electron. Conf. (IPEC-Hiroshima ECCE-Asia)*, 2014, pp. 3298–3305.

[10] Y., Banjo, Y. Miura, T. Ise, and T. Shintai, “Enhanced stand-alone operating characteristics of an engine generator interconnected through the inverter using virtual synchronous generator control,” in *Proc. Int. Conf. Power Electron.*, 2015, pp.1003–1010.

[11] J. Driesen and K. Visscher “Virtual synchronous generators,” in Proc. IEEE Power Energy Soc. Gen. Meeting—Convers. Del. Elect. Energy 21st Century, 2008, pp. 1–3.

[12] H. Bevrani, T. Ise, and Y. Miura, “Virtual synchronous generators: A survey and new perspectives,” *Int. J. Elect. Power Energy Syst.*, vol. 54, no. 1, pp. 244–254, Jan. 2014.

[13] K. Visscher and S. W. H. de Haan, “Virtual synchronous machines (VSG’s) for frequency stabilisation in future grids with a significant share of decentralized generation,” in *Proc. IET-CIRED Seminar SmartGrids for Distribution*, 2008, pp. 1–4.

[14] M.P.N. van Wesenbeeck, S.W.H. de Haan, P. Varela, and K. Visscher, “Grid tied converter with virtual kinetic storage,” in *Proc. IEEE Bucharest PowerTech*, 2009, pp.1–7.

[15] T. Loix, S. de Breucker, P. Vanassche, J. van den Keybus, J. Driesen, and K. Visscher, “Layout and performance of the power electronic converter platform for the VSYNC project,” in *Proc. IEEE Bucharest PowerTech*, 2009, pp. 1–8.

[16] M. Albu, K. Visscher, D. Creanga, A. Nechifor, and N. Golovanov, “Storage selection for DG applications containing virtual synchronous generators,” in *Proc. IEEE Bucharest PowerTech*, 2009, pp.1–6.

[17] T. Vu Van, A. Woyte, M. Albu, M. van Hest, J. Bozelie, J. Diaz, T. Loix, D. Stanculescu, and K. Visscher, “Virtual synchronous generator: Laboratory scale results and field demonstration,” in *Proc. IEEE Bucharest PowerTech*, 2009, pp.1–6.

[18] M. Albu, J. Diaz, V. Thong, R. Neurohr, D. Federenciuc, M. Popa, and M. Calin, “Measurement and remote monitoring for virtual synchronous generator design,” in *Proc. IEEE Int. Workshop Appl. Measurements for Power Syst.*, 2010, pp.7–11.

[19] V. Karapanos, Z. Yuan, and S. W. H. de Haan, “SOC maintenance and coordination of multiple VSG units for grid support and transient stability,” presented at the 3rd VSYNC workshop, Cheia, Romania, 2010. [Online]. Available: http://www.vsync.eu/fileadmin/vsync/user/docs/ Workshop3/Karapanos.pdf

[20] M. Albu, M. Calin, D. Federenciuc, and J. Diaz, “The measurement layer of the Virtual Synchronous Generator operation in the field test,” in *Proc. IEEE Int. Workshop Appl. Measurements for Power Syst.*, 2011, pp.85–89.

[21] V. Karapanos, S. W. H. de Haan, and K. H. Zwetsloot, “Testing a virtual synchronous generator in a real time simulated power system,” in *Proc. Int. Conf. Power Syst. Transients*, 2011.

[22] V. Karapanos, S. W. H. de Haan, and K. H. Zwetsloot, “Real time simulation of a power system with VSG hardware in the loop," in *Proc. Annu. Conf. IEEE Ind. Electron. Soc.*, 2011, pp. 3748–3754.

[23] H.-P. Beck and R. Hesse, "Virtual synchronous machine," in *Proc. Int. Conf. Elect. Power Quality and Utilisation*, 2007, pp. 1–6.

[24] R. Hesse, D. Turschner, and H.-P. Beck, "Micro grid stabilization using the virtual synchronous machine (VISMA)," in *Proc. Int. Conf. Renewable Energies and Power Quality*, 2009, pp. 1–6.

[25] Y. Chen, R. Hesse, D. Turschner, and H.-P. Beck, "Dynamic properties of the virtual synchronous machine (VISMA)," in *Proc. Int. Conf. Renewable Energies and Power Quality*, 2011, pp. 1–5.

[26] Y. Chen, R. Hesse, D. Turschner, and H.-P. Beck, "Improving the grid power quality using virtual synchronous machines," in *Proc. Int. Conf. Power Eng., Energy and Elect. Drives*, 2011, pp.1–6.

[27] Y. Chen, R. Hesse, D. Turschner, and H.-P. Beck, "Comparison of methods for implementing virtual synchronous machine on inverters," in *Proc. Int. Conf. Renewable Energies and Power Quality*, 2012, pp. 1–6.

[28] Y. Chen, R. Hesse, D. Turschner, and H.-P. Beck, "Investigation of the Virtual Synchronous Machine in the island mode," in *Proc. IEEE PES Int. Conf. and Exhibition on Innovative Smart Grid Technologies*, 2012, pp.1–6.

[29] Y. Hirase, A. Kazuhiro, K. Sugimoto, and Y. Shindo, "A grid-connected inverter with virtual synchronous generator model of algebraic type," *IEEJ Trans. Power and Energy*, vol. 132, no. 4, pp. 371–380, Apr. 2012 (in Japanese). or *Electrical Engineering in Japan*, vol. 184, no. 4, pp. 10–21, Sep. 2013 (in English).

[30] Y. Hirase, O. Noro, E. Yoshimura, H. Nakagawa, K. Sakimoto, and Y. Shindo, "Virtual synchronous generator control with double decoupled synchronous reference frame for single-phase inverter," *IEEJ J. Ind. Appl.*, vol. 4, no. 3, pp. 143–151, May 2015.

[31] Y. Hirase, O. Noro, K. Sugimoto, K. Sakimoto, Y. Shindo, and T. Ise, "Effects of suppressing frequency fluctuations by parallel operation of virtual synchronous generator in microgrids," in *Proc. IEEE Energy Convers. Congr. and Expo.*, 2015, pp. 3694–3701.

[32] Q.-C. Zhong and G. Weiss, "Synchronverters: inverters that mimic synchronous generators," *IEEE Trans. Ind. Electron.*, vol. 58, no. 4, pp. 1259–1267, Apr. 2011.

[33] Q.-C. Zhong, P.-L. Nguyen, Z. Ma, and W. Sheng, "Self-synchronized synchronverters: inverters without a dedicated synchronization unit," *IEEE Trans. Power Electron.*, vol. 29, no. 2, pp. 617–630, Feb. 2014.

[34] W.-L. Ming and Q.-C. Zhong, "Synchronverter-based transformerless PV inverters," in *Proc. Annu. Conf. IEEE Ind. Electron. Soc.*, 2014, pp. 4396–4401.

[35] Z. Ma; Q.-C. Zhong, and J. D. Yan, "Synchronverter-based control strategies for three-phase PWM rectifiers in *Proc. IEEE Conf. on Ind. Electron. and Appl.*, 2012, pp. 225–230.

[36] P.-L. Nguyen, Q.-C. Zhong, F. Blaabjerg, and J.M. Guerrero, "Synchronverter-based operation of STATCOM to mimic synchronous condensers," in *Proc. IEEE Conf. on Ind. Electron. and Appl.*, 2012, pp. 942–947.

[37] R. Aouini, B. Marinescu, K. Ben Kilani, and M. Elleuch, "Synchronverter-based emulation and control of HVDC transmission," *IEEE Trans. Power Syst.*, vol. 31, no. 1, pp. 278–286, Jan. 2016.

[38] S. Dong, Y.-N. Chi, and Y. Li, "Active voltage feedback control for hybrid multi-terminal hvdc system adopting improved synchronverters," *IEEE Trans. Power Del.*, doi: 10.1109/ TPWRD.2015.2420657.

[39] G. Delille, B. Francois, and G Malarange, "Dynamic frequency control support by energy storage to reduce the impact of wind and solar generation on isolated power system's inertia," *IEEE Trans. Sustain. Energy*, vol. 3, no. 4, pp. 931–939, Oct. 2012.

[40] M. A. Torres L., L. A. C. Lopes, L. A. Moran T., and J. R. Espinoza C., "Self-tuning virtual synchronous machine: A control strategy for energy storage systems to support dynamic frequency control," *IEEE Trans. Energy Convers.*, vol. 29, no. 4, pp. 833–840, Dec. 2014.

[41] M. Guan, W. Pan, J. Zhang, Q. Hao, J. Cheng, and X. Zheng, "Synchronous generator emulation control strategy for voltage source converter (VSC) stations," *IEEE Trans. Power Syst.*, vol. 30, no. 6, pp. 3093–3101, Nov. 2015.

[42] Y. Du, J. M. Guerrero, L. Chang, J. Su, and M. Mao, "Modeling, analysis, and design of a frequency-droop-based virtual synchronous generator for microgrid applications," in *Proc. IEEE ECCE Asia Downunder*, 2013, pp. 643–649.

[43] N. Soni, S. Doolla, and M. C. Chandorkar, "Improvement of transient response in microgrids using virtual inertia," *IEEE Trans. Power Del.*, vol. 28, no. 3, pp. 1830–1838, Jul. 2013.

Chapter 3

Dynamic Characteristics Comparisons Between Droop Control and VSG Control

3.1 Introduction

In this chapter, a comprehensive comparison of dynamic characteristics between droop control and VSG control is presented, in order to understand the difference of the two control methods caused by the presence of swing equation, and the advantage and disadvantage of VSG control over traditional voltage-source-based grid-supporting control [1], [2].

Small-signal models of both methods are built, for the case of single inverter operation and that of parallel operation with a SG, to calculate theoretical step responses of frequency change, in order to understand the inertia effect caused by the virtual inertia. Effects of delays in governor of VSG and *P* droop controller of droop control are also evaluated, and an approximated VSG control based on droop control, i.e. inertial droop control, is proposed. State-space models of both methods are constructed to study oscillation of output active power. Theoretical results are verified by simulations using PSCAD/EMTDC and by experiments of a scale-down system.

Comparison between droop control and VSG control in a VSC-HVDC transmission system is demonstrated in [3], to show that the virtual inertia helps to reduce maximum frequency excursion during a short-time fault, and during loading transition when secondary frequency control is applied; however, detailed theoretical analysis is not provided. A comparison on transient active power performance is presented in [4], but the differences on inertia and transient frequency are not discussed. Moreover, although the idea of using a first-order lag unit in droop control to emulate virtual inertia is already mentioned in [3], [4], it is further developed in this dissertation by adding a first-order lag unit to emulate the damping factor.

It should be pointed out that although the VSG control scheme studied in this chapter is based on the basic VSG control introduced in Section 2.3, several results should also be valid for other voltage-source-based grid-supporting control with virtual inertia. Moreover, the small-signal models and state-space models presented in this chapter provide a general method for analyses of dynamic performances of VSG and droop control, which smooth the path of future studies on this topic. Actually, several improvements and modifications on VSG control proposed in Chapters 4 and 5 are based on the state-space analyses presented in this chapter.

3.2 Droop Control

3.2.1 Overview of Droop Control

Droop control is a control method for real and reactive power regulation by imitating the parallel operation characteristics of synchronous generators (SGs). It is initially proposed for uninterruptible power supply (UPS) systems [5], and has been developed into a general approach for parallel inverters [6], especially in microgrids [7]–[33] and UPS systems [34], [35].

There are several variants of droop control. To be applied in low voltage (LV) network, in which the line impedance is mainly resistive, $P-V$ and $Q-\omega$ droop control [8]–[11], instead of traditional $P-\omega$ and $Q-V$ droop [5]–[7], has been proposed to improve power sharing and stability. Moreover, a virtual frequency-voltage frame method is proposed to solve this problem in any giving condition of line impedance R/X ratio [12]. On the other hand, $P-\omega$ and $Q-V$ droop can still be applied in LV network by adding virtual output impedance to make the total line impedance inductive [14]–[16], [34], [35].

In a hierarchical microgrid control structure, droop control usually plays the role of primary control, in which secondary control is designed to keep the frequency and voltage around the nominal value [13]–[18], and/or to obtain accurate reactive power [17]–[22], harmonic and unbalance power sharing [20] and voltage harmonic compensation [18], [23] in islanded mode, and tertiary control is designed to manage synchronization to the main grid, power-flow control in grid-connected mode and optimal operation [15], [16]. As secondary and tertiary control need communication command from a central controller, issues are still encouraged to be solved with a wireless manner, such as it is proposed in [23]–[28] for accurate power sharing, in [29] for operation with unbalance load and nonlinear load, in [30] for harmonic components dispatch, and in [31] for reducing frequency and voltage deviation. It has also been demonstrated that optimization of droop coefficients [32] and supplementary droop control loop [33] can help to enhance system stability.

As current-source-based droop control cannot provide voltage support for islanded microgrid, most droop control methods proposed in the literature are voltage-source-based droop control. A typical voltage-source-based droop control using $P-\omega$ and $Q-V$ is depicted in Fig. 3.1.

The blocks "*P* Droop" and "*Q* Droop", as shown in Figs. 3.2 and 3.3, are based on $P-\omega$ and $Q-V$ droop control laws, respectively. The input of the droop controller is the output active and reactive power P_{out} and Q_{out} calculated from output voltage and current, and the output is the output frequency ω_m and output voltage reference V_{ref}. The first lag unit with a time constant T_d is used to filter the high frequency ripples in the calculated P_{out} and Q_{out}

The relations shown in Figs. 3.2 and 3.3 can be expressed as (3.1) and (3.2), respectively.

$$\omega_m = -\frac{P_{out}-P_0}{k_p(1+T_d s)} + \omega_0 \tag{3.1}$$

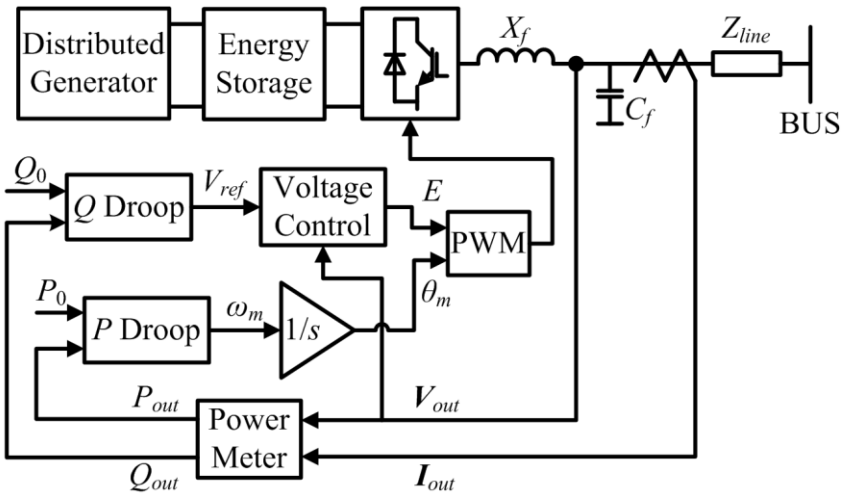

Fig. 3.1 Block diagram of the conventional voltage-source-based droop control scheme.

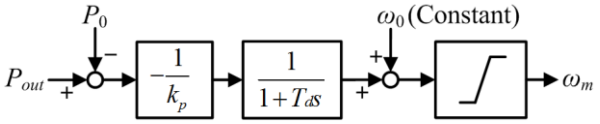

Fig. 3.2 Block diagram of the "*P* Droop" block of conventional droop control.

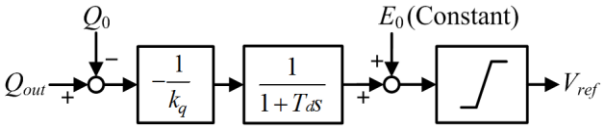

Fig. 3.3 Block diagram of the "*Q* Droop" block of conventional droop control.

$$V_{ref} = -\frac{Q_{out} - Q_0}{k_q(1 + T_d s)} + E_0 \tag{3.2}$$

Compared with the "Governor Model" and "*Q* Droop" controller of the basic VSG control (Figs. 2.5 and 2.6), it can be observed that the input and output are inversed. The difference between $P - \omega$ droop and $\omega - P$ droop is discussed in Section 3.3.3, and difference between $Q - V$ droop and $V - Q$ droop is discussed in Section 4.3 of next chapter.

The block "Voltage Control" is used to control the amplitude of output voltage to the voltage reference value V_{ref}. There are a variety of choices for the control method inside the "Voltage Control" block. It can be either a single voltage loop control [7] or a multi-loop control composed of an outer voltage loop and an inner current loop [11]-[13]. Nevertheless, detailed discussion on the voltage controller of droop control is beyond the scope of this dissertation.

3.2.2 Principles of Active Control Part of VSG Control and Droop Control

In this chapter, to simplify the model in order to focus on active power control, reactive power control parts of both VSG control and droop control are inactivated. Therefore, the output voltage of inverter E is fixed to the nominal voltage E_0, as illustrated in Figs. 3.4 and 3.5. Detailed discussion on reactive power control part is presented in Section 4.3 of next chapter.

From (2.2) and (2.9), the active power control of VSG control can be expressed in a single equation by eliminating P_{in}, as shown in (3.3).

$$P_0 - \frac{k_p}{1+T_d s}(\omega_m - \omega_0) - P_{out} = J\omega_m \frac{\mathrm{d}\omega_m}{\mathrm{d}t} + D(\omega_m - \omega_g) \tag{3.3}$$

It is simpler to neglect the effect of first-order delay at the beginning of the comparison. There-

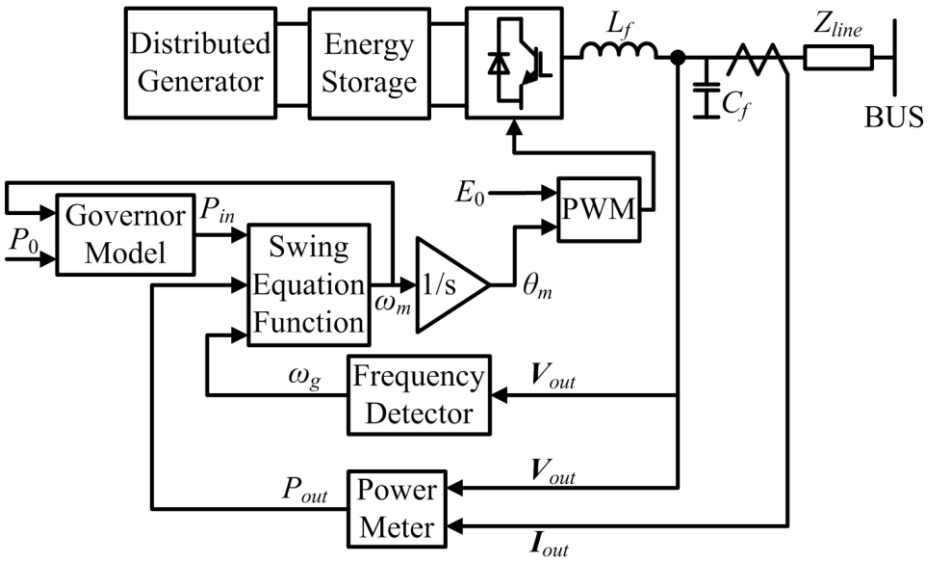

Fig. 3.4 Simplified VSG control without reactive power control.

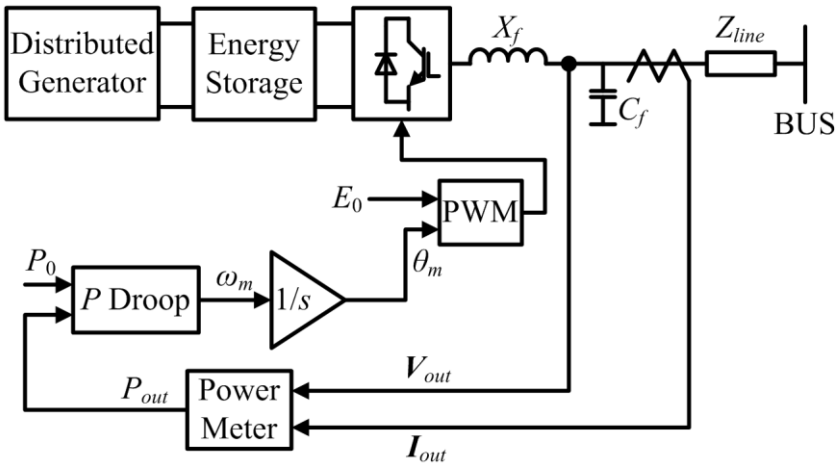

Fig. 3.5 Simplified droop control without reactive power control.

fore, (3.3) and (3.1) can be simplified as (3.4) and (3.5), respectively.

$$P_0 - k_p(\omega_m - \omega_0) - P_{out} = J\omega_m \frac{\mathrm{d}\omega_m}{\mathrm{d}t} + D\left(\omega_m - \omega_g\right) \tag{3.4}$$

$$\omega_m = -\frac{P_{out} - P_0}{k_p} + \omega_0 \tag{3.5}$$

Letting $J = 0,\ D = 0$, (3.4) is equivalent to (3.5). In other words, droop control can be considered as a particular case of VSG control, in which both inertia and damping factor are set to zero.

3.3 Comparisons of Transient Responses of Frequency

In this section, first, small-signal models of VSG and droop control are built for both single inverter operation and parallel operation with a SG. Then, based on these models, step responses of frequency change during a loading transition are calculated. The system with slower change of frequency is preferable, because lower $\mathrm{d}f/\mathrm{d}t$ indicates larger inertia. System with smaller inertia is prone to exceed the $\mathrm{d}f/\mathrm{d}t$ threshold of relays during a large loading transition, which may lead to unnecessary tripping and load shedding. Moreover, system with larger inertia suffers smaller maximum frequency excursion during a short time fault, and during a loading transition when secondary control is applied, as it is demonstrated in [3].

3.3.1 Single Inverter Operation

First of all, single inverter operation model shown in Fig. 3.6 is studied. The capacitor of the DG output filter shown in Figs. 3.4 and 3.5 is neglected as its susceptance is usually negligible at fundamental frequency.

The power flow S_{e_dg} out of the virtual internal emf $E_{dg}\angle\delta_{dg}$ can be expressed as

$$\begin{aligned} S_{e\_dg} &= P_{e\_dg} + jQ_{e\_dg} \\ &= \frac{E_{dg}}{R_{dg}^2 + X_{dg}^2}\left[R_{dg}\left(E_{dg} - V_{bus}\cos\delta_{dg}\right) + X_{dg}V_{bus}\sin\delta_{dg}\right] \\ &+ j\frac{E_{dg}}{R_{dg}^2 + X_{dg}^2}\left[-R_{dg}V_{bus}\sin\delta_{dg} + X_{dg}\left(E_{dg} - V_{bus}\cos\delta_{dg}\right)\right], \end{aligned} \tag{3.6}$$

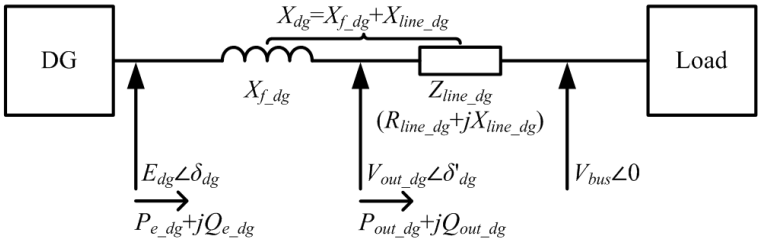

Fig. 3.6 System model of the case of single inverter operation.

where subscript "*dg*" indicates parameters related to DG, $X_{dg} = X_{f\_dg} + X_{line\_dg}$ and $R_{dg} \approx R_{line\_dg}$ are the total output reactance and resistance of DG, respectively, V_{bus} is the RMS value of bus voltage, δ_{dg} is the power angle of DG (angle difference between the virtual internal emf and bus voltage).

Equation (3.6) can be simplified to (3.7) if $R_{dg} \ll X_{dg}$. It is always the case in high voltage (HV) network because a transmission line is mainly inductive. In low voltage (LV) network where distribution line is mainly resistive, the filter inductance X_{f_dg} is usually large enough to make the output impedance inductive. Even it is not the case, the total output impedance can be adjusted to be inductive by the stator impedance adjuster presented in Section 4.4.

$$S_{e\_dg} = P_{e\_dg} + jQ_{e\_dg} = \frac{E_{dg}V_{bus}\sin\delta_{dg}}{X_{dg}} + j\frac{E_{dg}(E_{dg} - V_{bus}\cos\delta_{dg})}{X_{dg}} \tag{3.7}$$

If the power loss in the power devices of inverter and in the output LC filter is neglected, $P_{e\_dg} \approx$ ed, $P_{e\_dg} \approx P_{out\_dg}$. Therefore, the small-signal relation of ΔP_{out_dg} can be deduced from (3.7) as

$$\Delta P_{out\_dg} = K_{dg}\Delta\delta_{dg}, \tag{3.8}$$

where

$$K_{dg} = \frac{E_{dg}V_{bus}\cos\delta_{dg}}{X_{dg}} \tag{3.9}$$

is the transient synchronizing power coefficient of the DG. For an inverter-interfaced DG, the power angle δ_{dg} is usually small and $\cos\delta_{dg} \approx 1$.

Knowing that $s\Delta\delta_{dg} = \Delta\omega_{m\_dg} - \Delta\omega_g$, so that (3.8) becomes

$$s\Delta P_{out\_dg} \approx K_{dg}\left(\Delta\omega_{m\_dg} - \Delta\omega_g\right). \tag{3.10}$$

The small-signal model of (3.4) can be written as

$$-k_{p\_dg}\Delta\omega_{m\_dg} - \Delta P_{out\_dg} = J_{dg}(\omega_{m\_dg}s\Delta\omega_{m\_dg} + s\Delta\omega_{m\_dg}^2) + D_{dg}\left(\Delta\omega_{m\_dg} - \Delta\omega_g\right). \tag{3.11}$$

As the frequency deviation from nominal frequency is relatively small, $\omega_{m\_dg}s\Delta\omega_{m\_dg} \approx \omega_0 s\Delta\omega_{m\_dg}$. Moreover, second order perturbation terms can be neglected. Therefore, (3.11) becomes

$$-k_{p\_dg}\Delta\omega_{m\_dg} - \Delta P_{out\_dg} = J_{dg}\omega_0 s\Delta\omega_{m\_dg} + D_{dg}\left(\Delta\omega_{m\_dg} - \Delta\omega_g\right). \tag{3.12}$$

If line losses are neglected, $\Delta P_{out\_dg} = \Delta P_{load}$, where P_{load} is the active power consumed by the load. Eliminating $\Delta\omega_g$ from (3.10) and (3.12) gives

$$\frac{\Delta\omega_{m\_dg}}{\Delta P_{load}} = -\frac{1 + \frac{D_{dg}}{K_{dg}}s}{k_{p\_dg} + J_{dg}\omega_0 s}. \tag{3.13}$$

Equation (3.13) is the transfer function of frequency change over a small loading transition for a VSG-control-based DG in the case of single inverter operation. Let $J_{dg} = 0$, $D_{dg} = 0$, and then the transfer function for a droop-control-based DG can be obtained as follows.

$$\frac{\Delta\omega_{m\_dg}}{\Delta P_{load}} = -\frac{1}{k_{p\_dg}} \tag{3.14}$$

Let $s = 0$ in (3.13), and then (3.13) is equivalent to (3.14). This implies that steady-state gain of (3.13) is determined by droop coefficient k_{p_dg} and is independent of swing equation parameters. In other words, steady states of VSG control and droop control are the same if droop coefficients k_{p_dg} are set equally.

It is possible to calculate the step responses of DG frequency change during a small loading transition through (3.13) and (3.14), as illustrated in Fig. 3.7. Parameters used for calculation are listed in Table 3.1. It is shown in Fig. 3.7 that the frequency of VSG control changes slowly, whereas that of droop control suffers a step change. This implies that DG with VSG control has inertia thanks to the swing equation, and that DG with droop control has nearly no inertia. Moreover, larger value of J_{dg} results in slower frequency change, which indicates that inertia of the DG is determined by J_{dg}. On the other hand, D_{dg} has barely any influence on dynamic response in this situation. Besides, steady states of all cases are the same. This verifies previous conclusion that steady states only de-

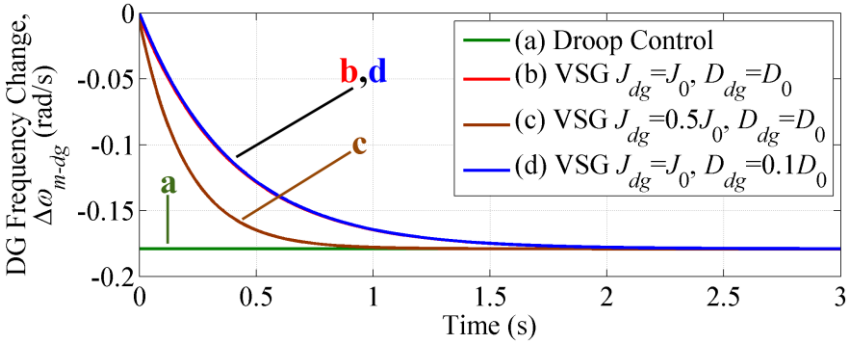

Fig. 3.7 Step responses of DG frequency during a loading transition in the case of single inverter operation with various parameters.

TABLE 3.1 Parameters of the Case of Single Inverter Operation

Parameter	Value	Parameter	Value
$E_{dg} = E_0$	6.6 kV	$k^*_{p\_dg}$	20 pu
S_{base_dg}	1 MVA	$X^*_{f\_dg}$	0.1298 pu
$P^*_{0\_dg}$	1 pu	$X^*_{line\_dg}$	0.0076 pu
ω_0	376.99 rad/s	$\cos\delta_{dg}$	≈1
M^*_0	8 s	V_{bus}	6.57 kV
D^*_0	17 pu	ΔP_{load}	0.0095 MW

pend on k_{p_dg}.

3.3.2 Parallel Operation with a SG

In this section, parallel operation of DG and SG illustrated in Fig. 3.8 is studied to show the importance of inertia in a network with high penetration level of inverter-interfaced DG. It is assumed that the penetration rate of DG in this network is up to 50%, and the rest of power generation comes from a salient-pole SG. In this case, it is preferred to study the rotor frequency change of SG rather than that of DG because the former is considered as the dominant one.

From the law of conservation of energy,

$$\Delta P_{out\_dg} + \Delta P_{out\_sg} = \Delta P_{load}, \tag{3.15}$$

where subscript "sg" indicates parameters related to SG. Let $A = \frac{\Delta P_{out\_dg}}{\Delta \omega_g}$ and $B = \frac{\Delta P_{out\_sg}}{\Delta \omega_g}$, so that (3.15) becomes

$$\Delta P_{out\_sg}\left(1 + \frac{A}{B}\right) = \Delta P_{load}. \tag{3.16}$$

The same equation as (3.10) holds for SG, as shown in (3.17).

$$s\Delta P_{out\_sg} \approx K_{sg}\left(\Delta \omega_{m\_sg} - \Delta \omega_g\right) \tag{3.17}$$

Eliminate ΔP_{out_sg} from (3.16) and (3.17), so that

$$\frac{\Delta \omega_{m\_sg}}{\Delta P_{load}} = \frac{K_{sg} + Bs}{K_{sg}(A + B)}. \tag{3.18}$$

Now if A and B are known, the required transfer function can be obtained.

Eliminate $\Delta \omega_{m\_dg}$ from (3.10) and (3.12), and then

$$A = \frac{\Delta P_{out\_dg}}{\Delta \omega_g} = -\frac{k_{p\_dg} + J_{dg}\omega_0 s}{1 + \frac{k_{p\_dg} + D_{dg}}{K_{dg}} s + \frac{J_{dg}\omega_0}{K_{dg}} s^2}. \tag{3.19}$$

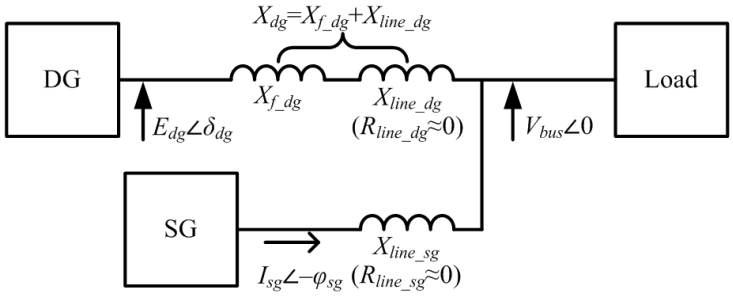

Fig. 3.8 System model of the case of parallel operation with a SG.

Because SG has the same model as VSG, (3.19) is also true for SG, as shown in (3.20).

$$B = \frac{\Delta P_{out\_sg}}{\Delta \omega_g} = -\frac{k_{p\_sg} + J_{sg}\omega_0 s}{1 + \frac{k_{p\_sg} + D_{sg}}{K_{sg}} s + \frac{J_{sg}\omega_0}{K_{sg}} s^2} \tag{3.20}$$

Let $J_{dg} = 0,\ D_{dg} = 0$ in (3.19), and then A for droop control can be obtained as

$$A = \frac{\Delta P_{out\_dg}}{\Delta \omega_g} = -\frac{k_{p\_dg}}{1 + \frac{k_{p\_dg}}{K_{dg}} s}. \tag{3.21}$$

Remember that for SG, K_{sg} and D_{sg} are not constant and are dependent on the power angle δ_{sg} and SG impedance parameters. D_{sg} can be calculated through (2.3) and K_{sg} can be calculated as follows for a salient-pole SG [36].

$$K_{sg} = \frac{E'_q V_{bus}}{X'_d + X_{line\_sg}} \cos\delta_{sg} - \frac{{V_{bus}}^2 (X_q - X'_d)}{(X_q + X_{line\_sg})(X'_d + X_{line\_sg})} \cos(2\delta_{sg}), \tag{3.22}$$

where X_q is the q-axis synchronous reactance of the SG, E'_q is the q-axis transient internal emf.

In order to verify the results through simulation lately, all parameters need to be measurable. Actually, all parameters in (2.3) and (3.22) except power angle δ_{sg}, transient internal emf E'_q and bus voltage V_{bus} are fixed SG parameters which can be found in data sheets. Besides, V_{bus} can be measured directly, while δ_{sg} and E'_q can be calculated through (3.23) and (3.24) with the measurement of the amplitude of SG output current I_{sg} and the angle φ_{sg} which is the phase difference between $\boldsymbol{V_{bus}}$ and $\boldsymbol{I_{sg}}$ as shown in Fig. 3.8.

$$\delta_{sg} = \tan^{-1} \frac{(X_q + X_{line\_sg}) I_{sg} \cos\varphi_{sg}}{V_{bus} + (X_q + X_{line\_sg}) I_{sg} \sin\varphi_{sg}} \tag{3.23}$$

$$E'_q = V_{bus} \cos\delta_{sg} + I_{sg} \sin(\delta_{sg} + \varphi_{sg}) (X'_d + X_{line\_sg}) \tag{3.24}$$

It is noteworthy that unlike inverter-interfaced DG, SG power angle δ_{sg} is normally not negligible.

Based on (3.18)–(3.24), it is possible to calculate the step responses of SG rotor frequency change during a small loading transition, and the results are shown in Fig. 3.9. Note that for the calculation of B, (3.28) is used instead of (3.20), which is explicated in Section 3.3.3. Parameters of SG are listed in Table 3.2, and parameters of DG are the same as those in Table 3.1.

Like the case of single inverter operation, Fig. 3.9 demonstrates that DG with VSG control can contribute more inertia to the system than DG with droop control, since $\mathrm{d}f/\mathrm{d}t$ of the former is slower. Also, larger value of J_{dg} still increases the inertia of the system. In addition, system with larger D_{dg} has slightly smaller oscillation. Similarly, parameters of swing equation have no influence on steady state.

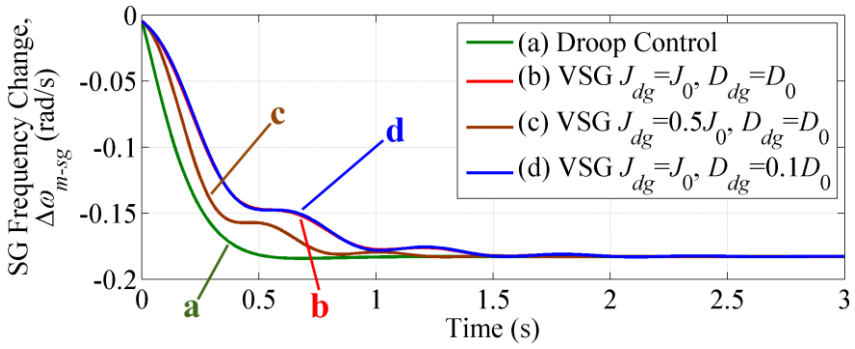

(a)

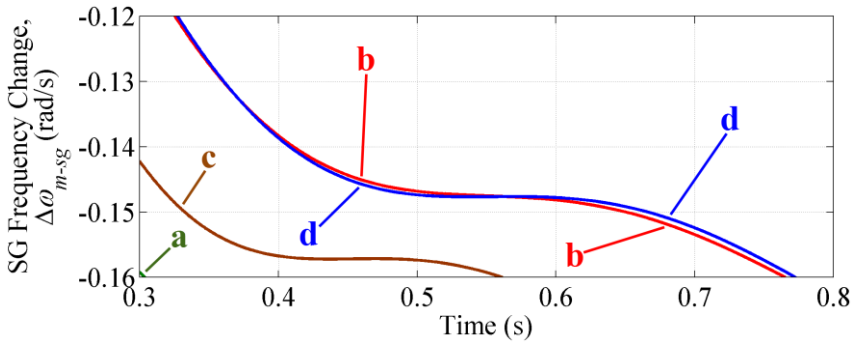

(b)

Fig. 3.9 (a) Step responses of SG rotor frequency during a loading transition in the case of parallel operation with a SG with various parameters. (b) Zoom-in of (a).

TABLE 3.2 Parameters of SG

Parameter	Value	Parameter	Value
V_{base_sg}	6.6 kV	$X_q^* = X'^*_q$	0.770 pu
S_{base_sg}	1 MVA	X''^*_q	0.375 pu
$P^*_{0\_sg}$	1 pu	T''_d	0.0348 s
ω_0	376.99 rad/s	T''_q	0.0346 s
M_0^*	8 s	T_{d_sg}	0.1 s
$k^*_{p\_sg}$	20 pu	I_{sg}	43.1 A
$X^*_{line\_sg}$	0.0076 pu	φ_{sg}	0.00655 rad
X_d^*	1.90 pu	V_{bus}	6.57 kV
X'^*_d	0.314 pu	ΔP_{load}	0.0194 MW
X''^*_d	0.280 pu		

3.3.3 Effects of Delays in Governor Model and *P* Droop Controller

In the analyses presented in Sections 3.3.1 and 3.3.2, the first-order lag units in the "Governor Model" of VSG and the "*P* Droop Controller" of droop control are neglected. In this section, effects of these delays are studied.

Comparing (3.3) with (3.4), it can be concluded that k_p should be replaced by $k_p/(1+T_d\mathrm{s})$ for all equations of VSG control if the first-order lag unit is not neglected. However, comparing (3.1) with (3.5), k_p should be replaced by $k_p(1+T_d\mathrm{s})$ for the equations of droop control. This difference is caused by the inverse of input and output in $P-\omega$ droop regulation as it is mentioned in Section 3.2.1. In VSG control, the input is active power and the output is frequency, whereas in droop control, it is the opposite, as illustrated in Figs. 2.5 and 3.2, respectively.

If this effect is taken into account for VSG, in the case of single inverter operation, (3.13) should be modified as

$$\frac{\Delta\omega_{m\_dg}}{\Delta P_{load}} = -\frac{1+\left(T_{d\_dg}+\frac{D_{dg}}{K_{dg}}\right)s+\frac{D_{dg}T_{d\_dg}}{K_{dg}}s^2}{k_{p\_dg}+J_{dg}\omega_0 s+J_{dg}\omega_0 T_{d\_dg}s^2}, \tag{3.25}$$

and for droop control, (3.14) becomes

$$\frac{\Delta\omega_{m\_dg}}{\Delta P_{load}} = -\frac{1}{k_{p\_dg}+T_{d\_dg}k_{p\_dg}\mathrm{s}}. \tag{3.26}$$

Meanwhile, in the case of parallel operation with a SG, for VSG and SG, (3.19) and (3.20) should be modified as

$$A = \frac{\Delta P_{out\_dg}}{\Delta\omega_g} = -\frac{k_{p\_dg}+J_{dg}\omega_0 s+T_{d\_dg}J_{dg}\omega_0 s^2}{1+\left(T_{d\_dg}+\frac{k_{p\_dg}+D_{dg}}{K_{dg}}\right)s+\frac{T_{d\_dg}D_{dg}+J_{dg}\omega_0}{K_{dg}}s^2+\frac{T_{d\_dg}J_{dg}\omega_0}{K_{dg}}s^3}, \tag{3.27}$$

$$B = \frac{\Delta P_{out\_sg}}{\Delta\omega_g} = -\frac{k_{p\_sg}+J_{sg}\omega_0 s+T_{d\_sg}J_{sg}\omega_0 s^2}{1+\left(T_{d\_sg}+\frac{k_{p\_sg}+D_{sg}}{K_{sg}}\right)s+\frac{T_{d\_sg}D_{sg}+J_{sg}\omega_0}{K_{sg}}s^2+\frac{T_{d\_sg}J_{sg}\omega_0}{K_{sg}}s^3}, \tag{3.28}$$

respectively, and for droop control, (3.21) becomes

$$A = \frac{\Delta P_{out\_dg}}{\Delta\omega_g} = -\frac{k_{p\_dg}+k_{p\_dg}T_{d\_dg}s}{1+\frac{k_{p\_dg}}{K_{dg}}s+\frac{k_{p\_dg}T_{d\_dg}}{K_{dg}}s^2}. \tag{3.29}$$

Based on (3.25)–(3.29), step responses of frequency can be recalculated and then compared with cases without consideration of delays, as shown in Figs. 3.10 and 3.11. The time constant T_{d_dg} is assumed to be 0.1 s.

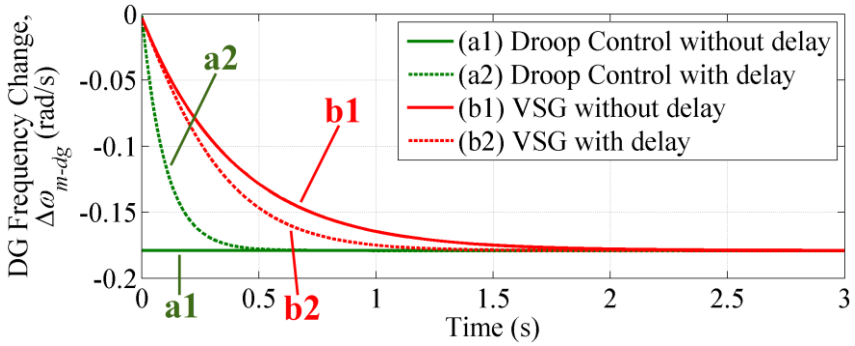

Fig. 3.10 Effects of delays on step responses of DG frequency during a loading transition in the case of single inverter operation.

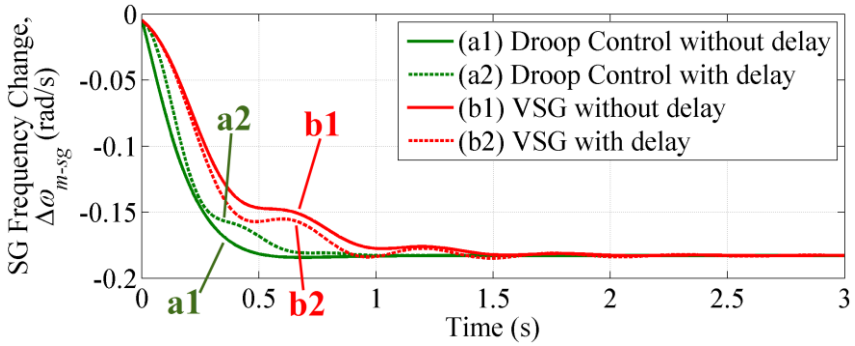

Fig. 3.11 Effects of delays on step responses of SG rotor frequency during a loading transition in the case of parallel operation with a SG.

Figs. 3.10 and 3.11 illustrate the point that inverse of input and output in $P-\omega$ droop control law results in different effect of delay for each control method. The delay makes the frequency of systems with VSG control change faster, but makes that of systems with droop control change more slowly in both the case of single inverter operation and the case of parallel operation with a SG. That is to say, the delay has a positive effect on droop control but a negative effect on VSG control.

3.3.4 Inertial Droop Control

It is interesting to compare (3.13) with (3.26), and (3.19) with (3.29). If T_{d_dg} is increased up to

$$T_{d\_dg} = \frac{J_{dg}\omega_0}{k_{p\_dg}}, \tag{3.30}$$

the only difference between (3.13) and (3.26), or (3.19) and (3.29) is that the equations of VSG control have terms coming from D_{dg}, whereas those of droop control do not. That is to say, by adding a first-order lag unit, with time constant T_{d_dg} specified by (3.30), into P droop controller, droop control can imitate the performance of VSG with a moment of inertia equal to J_{dg}.

Furthermore, if a first-order lead unit with a time constant T_{a_dg} is also added into *P* droop controller, as shown in Fig. 3.12, (3.26) and (3.29) become

$$\frac{\Delta\omega_{m\_dg}}{\Delta P_{load}} = -\frac{1+T_{a\_dg}s}{k_{p\_dg}+T_{d\_dg}k_{p\_dg}s}, \tag{3.31}$$

$$A = \frac{\Delta P_{out\_dg}}{\Delta\omega_g} = -\frac{k_{p\_dg}+k_{p\_dg}T_{d\_dg}s}{1+(\frac{k_{p\_dg}}{K_{dg}}+T_{a\_dg})s+\frac{k_{p\_dg}T_{d\_dg}}{K_{dg}}s^2}, \tag{3.32}$$

respectively. If the time constant T_{a_dg} is set to

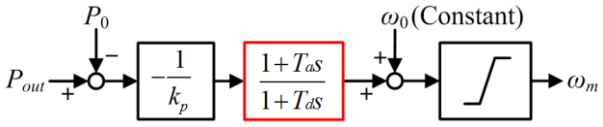

Fig. 3.12 *P* droop controller of droop control with a first-order lead-lag unit.

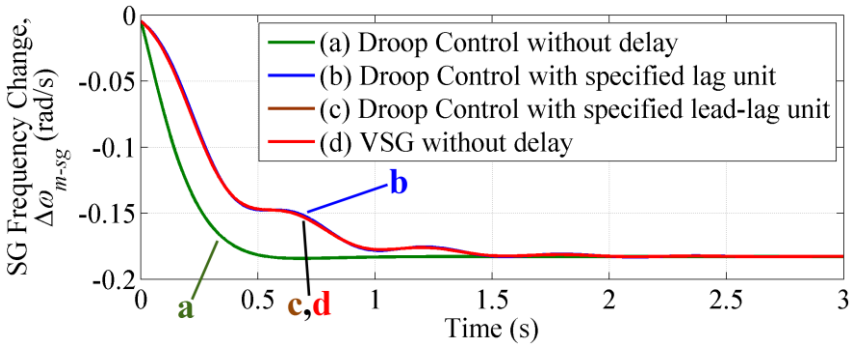

(a)

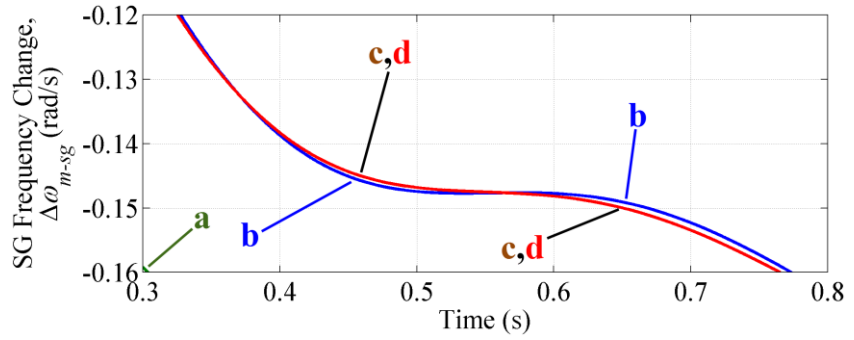

(b)

Fig. 3.13 (a) Step responses of SG rotor frequency during a loading transition in the case of parallel operation with a SG with specified lag or lead-lag unit in droop control. (b) Zoom-in of (a).

$$T_{a\_dg} = \frac{D_{dg}}{K_{dg}}, \tag{3.33}$$

then (3.31) is equivalent to (3.13), and (3.32) is equivalent to (3.19).

This conclusion is proved by Fig. 3.13. By adding a first-order lag unit with the time constant specified by (3.30), droop control results in similar step response to VSG control, with slightly larger oscillation due to lack of damping factor. Additionally, when a first-order lead unit with the time constant specified by (3.33) is also added, droop control leads to exactly the same step response as VSG control. This implies that during small disturbance, VSG can be approximated by droop control, with a first-order lag unit to simulate inertia, and with a first-order lead unit to simulate damping factor. Although similar conclusion on the relation between first-order lag unit and inertia is mentioned in [3], [4], the relation between first-order lead unit and damping factor has not been discussed in the literature.

3.4 Comparisons of Active Power Oscillation

Although VSG control outperforms droop control in the aspect of dynamic frequency performance, it is also known that the swing equation may cause oscillation in output active power during parallel operation. To understand this point, state-space models of the case of parallel operation with a SG are built, for both VSG and droop control, based on small-signal relations developed in Section 3.3.

$$\begin{cases} \dot{\boldsymbol{x}} = \boldsymbol{A}\boldsymbol{x} + \boldsymbol{B}\boldsymbol{w} \\ \boldsymbol{y} = \boldsymbol{C}\boldsymbol{x} + \boldsymbol{D}\boldsymbol{w} \end{cases}, \tag{3.34}$$

where

$$\boldsymbol{w} = [\Delta P_{load}] \tag{3.35}$$

$$\boldsymbol{y} = [\Delta\omega_{m\_sg} \quad \Delta\omega_{m\_dg} \quad \Delta P_{out\_sg} \quad \Delta P_{out\_dg}]^T \tag{3.36}$$

For VSG control:

$$\boldsymbol{x} = \begin{bmatrix} \Delta\omega_{m\_sg} + \dfrac{D_{sg}}{J_{sg}\omega_0(K_{sg}+K_{dg})}\Delta P_{load} \\ \Delta\omega_{m\_dg} + \dfrac{D_{dg}}{J_{dg}\omega_0(K_{sg}+K_{dg})}\Delta P_{load} \\ \Delta\delta_{sg} - \dfrac{1}{K_{sg}+K_{dg}}\Delta P_{load} \\ \Delta P_{in\_sg} \\ \Delta P_{in\_dg} \end{bmatrix} \tag{3.37}$$

$$\boldsymbol{A}=\begin{bmatrix} -\frac{D_{sg}K_{dg}}{J_{sg}\omega_0(K_{sg}+K_{dg})} & \frac{D_{sg}K_{dg}}{J_{sg}\omega_0(K_{sg}+K_{dg})} & -\frac{K_{sg}}{J_{sg}\omega_0} & \frac{1}{J_{sg}\omega_0} & 0 \\ \frac{D_{dg}K_{sg}}{J_{dg}\omega_0(K_{sg}+K_{dg})} & -\frac{D_{dg}K_{sg}}{J_{dg}\omega_0(K_{sg}+K_{dg})} & \frac{K_{sg}}{J_{dg}\omega_0} & 0 & \frac{1}{J_{dg}\omega_0} \\ \frac{K_{dg}}{K_{sg}+K_{dg}} & -\frac{K_{dg}}{K_{sg}+K_{dg}} & 0 & 0 & 0 \\ -\frac{k_{p\_sg}}{T_{d\_sg}} & 0 & 0 & -\frac{1}{T_{d\_sg}} & 0 \\ 0 & -\frac{k_{p\_dg}}{T_{d\_dg}} & 0 & 0 & -\frac{1}{T_{d\_dg}} \end{bmatrix} \tag{3.38}$$

$$\boldsymbol{B}=\begin{bmatrix} -\frac{K_{sg}}{J_{sg}\omega_0(K_{sg}+K_{dg})}-\frac{D_{sg}D_{dg}K_{dg}}{J_{sg}J_{dg}\omega_0^2(K_{sg}+K_{dg})^2}+\frac{D_{sg}^2K_{dg}}{J_{sg}^2\omega_0^2(K_{sg}+K_{dg})^2} \\ -\frac{1}{J_{dg}\omega_0}+\frac{K_{sg}}{J_{dg}\omega_0(K_{sg}+K_{dg})}-\frac{D_{sg}D_{dg}K_{sg}}{J_{sg}J_{dg}\omega_0^2(K_{sg}+K_{dg})^2}+\frac{D_{dg}^2K_{sg}}{J_{dg}^2\omega_0^2(K_{sg}+K_{dg})^2} \\ -\frac{D_{sg}K_{dg}}{J_{sg}\omega_0(K_{sg}+K_{dg})^2}+\frac{D_{dg}K_{dg}}{J_{dg}\omega_0(K_{sg}+K_{dg})^2} \\ \frac{k_{p\_sg}D_{sg}}{T_{d\_sg}J_{sg}\omega_0(K_{sg}+K_{dg})} \\ \frac{k_{p\_dg}D_{dg}}{T_{d\_dg}J_{dg}\omega_0(K_{sg}+K_{dg})} \end{bmatrix} \tag{3.39}$$

$$\boldsymbol{C}=\begin{bmatrix} 1 & 0 & 0 & 0 & 0 \\ 0 & 1 & 0 & 0 & 0 \\ 0 & 0 & K_{sg} & 0 & 0 \\ 0 & 0 & -K_{sg} & 0 & 0 \end{bmatrix} \tag{3.40}$$

$$\boldsymbol{D}=\begin{bmatrix} -\frac{D_{sg}}{J_{sg}\omega_0(K_{sg}+K_{dg})} \\ -\frac{D_{dg}}{J_{dg}\omega_0(K_{sg}+K_{dg})} \\ \frac{K_{sg}}{K_{sg}+K_{dg}} \\ \frac{K_{dg}}{K_{sg}+K_{dg}} \end{bmatrix} \tag{3.41}$$

For droop control:

$$\boldsymbol{x}=\begin{bmatrix} \Delta\omega_{m\_sg}+\frac{D_{sg}}{J_{sg}\omega_0(K_{sg}+K_{dg})}\Delta P_{load} \\ \Delta\omega_{m\_dg} \\ \Delta\delta_{sg}-\frac{1}{K_{sg}+K_{dg}}\Delta P_{load} \\ \Delta P_{in\_sg} \end{bmatrix} \tag{3.42}$$

$$\boldsymbol{A}=\begin{bmatrix} -\dfrac{D_{sg}K_{dg}}{J_{sg}\omega_0\left(K_{sg}+K_{dg}\right)} & \dfrac{D_{sg}K_{dg}}{J_{sg}\omega_0\left(K_{sg}+K_{dg}\right)} & -\dfrac{K_{sg}}{J_{sg}\omega_0} & \dfrac{1}{J_{sg}\omega_0} \\ 0 & -\dfrac{1}{T_{d\_dg}} & \dfrac{K_{sg}}{k_{p\_dg}T_{d\_dg}} & 0 \\ \dfrac{K_{dg}}{K_{sg}+K_{dg}} & -\dfrac{K_{dg}}{K_{sg}+K_{dg}} & 0 & 0 \\ -\dfrac{k_{p\_sg}}{T_{d\_sg}} & 0 & 0 & -\dfrac{1}{T_{d\_sg}} \end{bmatrix} \tag{3.43}$$

$$\boldsymbol{B}=\begin{bmatrix} -\dfrac{K_{sg}}{J_{sg}\omega_0\left(K_{sg}+K_{dg}\right)}+\dfrac{D_{sg}^2K_{dg}}{J_{sg}^2\omega_0^2\left(K_{sg}+K_{dg}\right)^2} \\ -\dfrac{1}{k_{p\_dg}T_{d\_dg}}+\dfrac{K_{sg}}{k_{p\_dg}T_{d\_dg}\left(K_{sg}+K_{dg}\right)} \\ -\dfrac{D_{sg}K_{dg}}{J_{sg}\omega_0\left(K_{sg}+K_{dg}\right)^2} \\ \dfrac{k_{p\_sg}D_{sg}}{T_{d\_sg}J_{sg}\omega_0\left(K_{sg}+K_{dg}\right)} \end{bmatrix} \tag{3.44}$$

$$\boldsymbol{C}=\begin{bmatrix} 1 & 0 & 0 & 0 \\ 0 & 1 & 0 & 0 \\ 0 & 0 & K_{sg} & 0 \\ 0 & 0 & -K_{sg} & 0 \end{bmatrix} \tag{3.45}$$

$$\boldsymbol{D}=\begin{bmatrix} -\dfrac{D_{sg}}{J_{sg}\omega_0\left(K_{sg}+K_{dg}\right)} \\ 0 \\ \dfrac{K_{sg}}{K_{sg}+K_{dg}} \\ \dfrac{K_{dg}}{K_{sg}+K_{dg}} \end{bmatrix} \tag{3.46}$$

It can be proved that the transfer functions of the first output $\Delta\omega_{m\_sg}$ over the input ΔP_{load} deduced from these state-space models are the same as those described by (3.18), (3.27)–(3.29).

Since oscillations in output variables, including DG output power ΔP_{out_dg}, are determined by the eigenvalues of state matrix $\boldsymbol{A}$, it is important to analyze how these eigenvalues vary according to different parameters, as shown in Fig. 3.14. In each diagram, radial lines indicate damping ratio ζ, whereas circle lines indicate undamped nature frequency ω_n. Parameters used for calculation are the same as those listed in Tables 3.1 and 3.2.

It is implied that VSG control is more oscillatory than droop control due to smaller ζ of the complex conjugate eigenvalues. Although oscillation in output power is a common phenomenon in SG, it may cause overcurrent in DG and stop the inverter, because an inverter usually has weaker overload ability than a SG of same rating. However, this problem can be solved by increasing damping factor D_{dg} and/or line reactance X_{dg}, as ζ of the complex conjugate eigenvalues in-

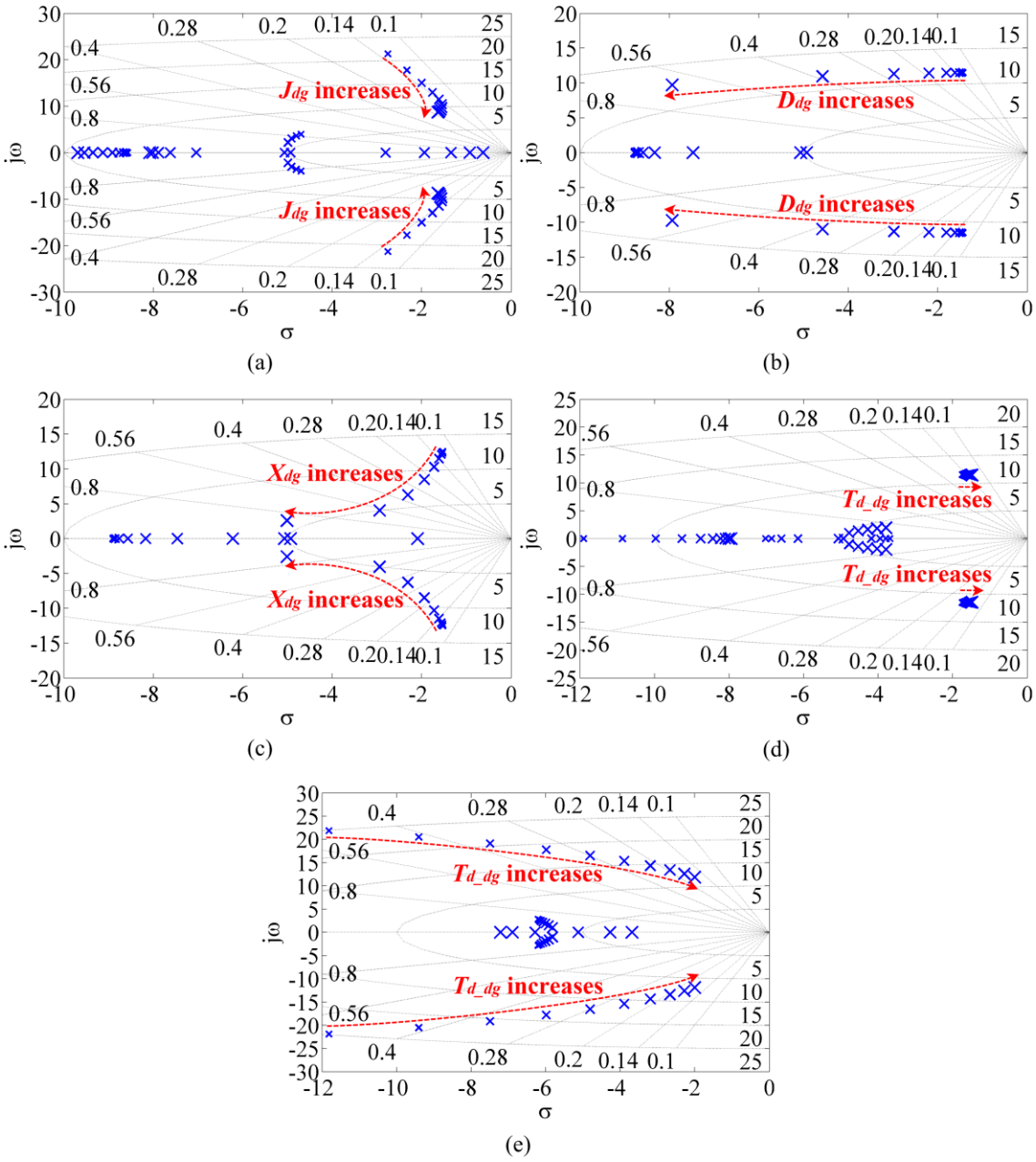

Fig. 3.14 Eigenvalues when (a) J_{dg} of VSG varies from $1.5^{-4}J_0$ to $1.5^{5}J_0$, (b) D_{dg} of VSG varies from $2^{-4}D_0$ to $2^{5}D_0$, (c) X_{dg} of VSG varies from $2.5^{-4}\times0.1374$ pu to $2.5^{5}\times0.1374$ pu, (d) T_{d_dg} of VSG varies from $1.09^{-4}\times0.1$ s to $1.09^{5}\times0.1$ s and (e) T_{d_dg} of droop control varies from $1.25^{-4}\times0.1$ s to $1.25^{5}\times0.1$ s.

creases in these cases as it is shown in Fig. 3.14. For example, a well-designed damping method based on modification of D_{dg} and considering line resistance is presented in [37]. As for X_{dg}, it can be increased by adjusting the stator impedance using virtual impedance control, which is further discussed in next chapter.

In addition, it is shown that J_{dg} affects the damped nature frequency ω_d, which is indicated by the distance between the eigenvalues and the real axis, but has barely any effect on the damping ratio.

It is also shown that the increase of T_{d_dg} not only results in higher $\mathrm{d}f/\mathrm{d}t$ as discussed in last section, but also makes the system more oscillatory. Therefore, it is better not to simulate governor delay in VSG control.

Droop control may also become oscillatory if the lag time constant T_{d_dg} is very large. In this case, its distribution of eigenvalues becomes similar to that of VSG control. This verifies the conclusion in Section 3.3.4, that droop control can be used to simulate VSG by increasing T_{d_dg}.

Moreover, for both control methods, no matter how parameters change, no right-half-plan pole is observed. This implies that parameters evaluated in this section do not influence the stability of active power control in the case of parallel operation with a SG.

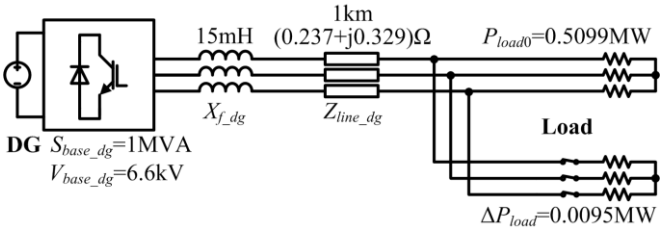

Fig. 3.15 Simulation circuit of the case of single inverter operation.

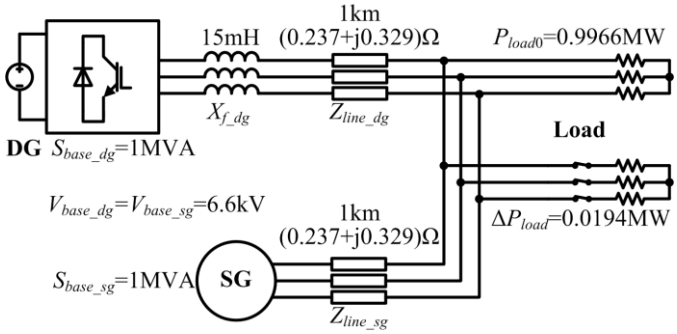

Fig. 3.16 Simulation circuit of the case of parallel operation with a SG.

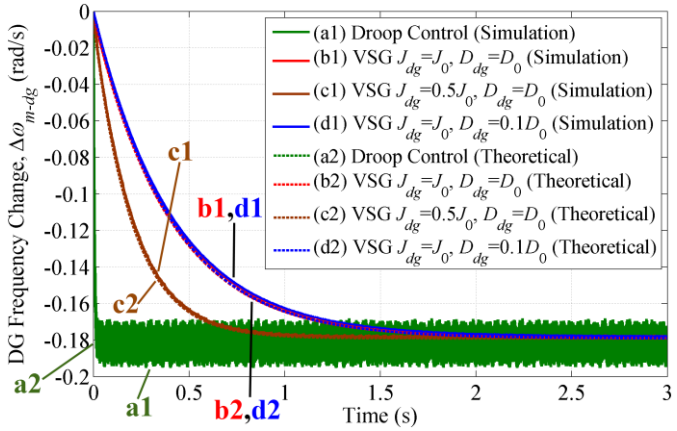

Fig. 3.17 Simulation results for the case of single inverter operation to verify Fig. 3.7.

3.5 Simulation Results

To verify the theoretical results, simulations are performed in PSCAD/EMTDC for all cases discussed in Section 3.3. Simulation circuits for the case of single inverter operation and that of parallel operation with a SG are shown in Figs. 3.15 and 3.16, respectively, and the results are shown in Figs. 3.17–3.21. All parameters are the same as those listed in Tables 3.1 and 3.2, except that resistance of

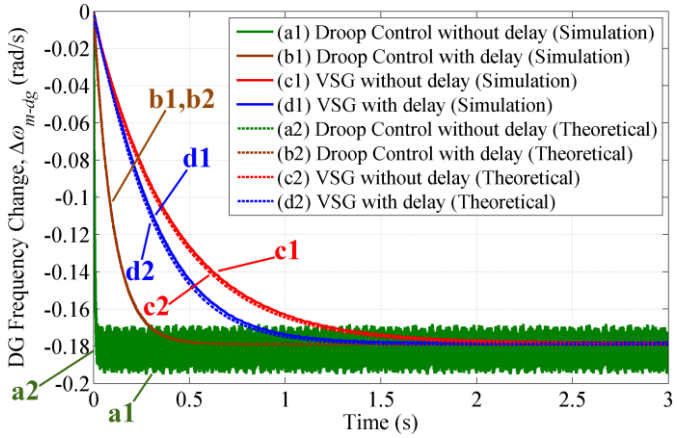

Fig. 3.18 Simulation results for the case of single inverter operation to verify Fig. 3.10.

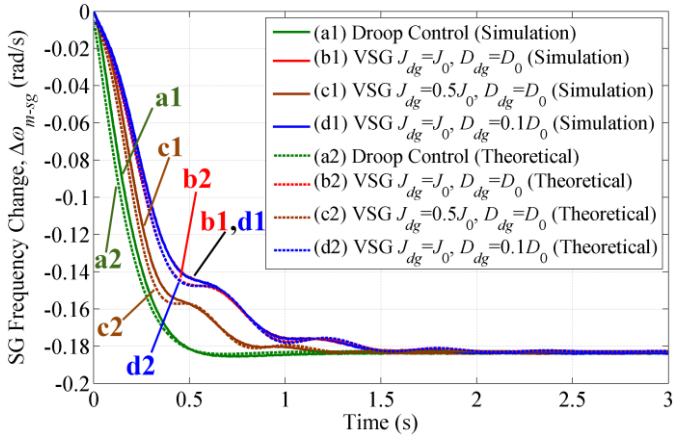

(a)

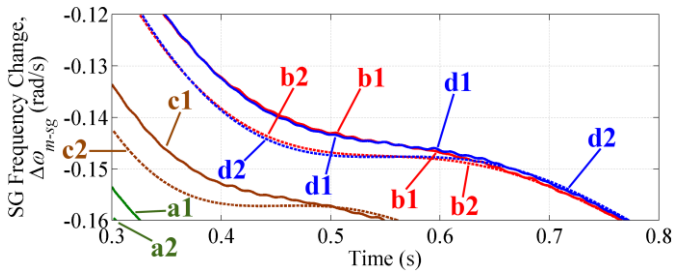

(b)

Fig. 3.19 Simulation results for the case of parallel operation with a SG to verify Fig. 3.9.

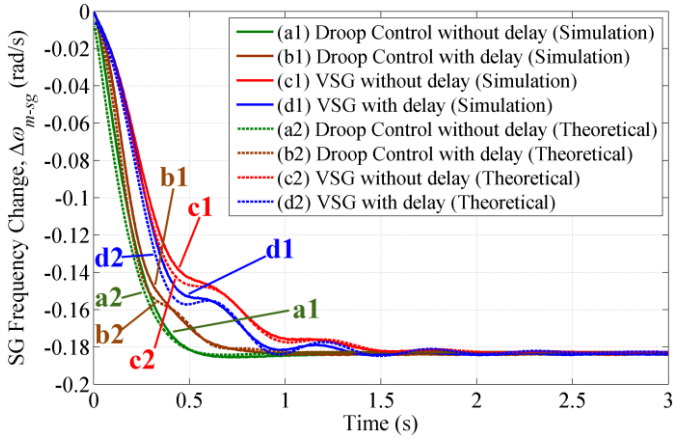

Fig. 3.20 Simulation results for the case of parallel operation with a SG to verify Fig. 3.11.

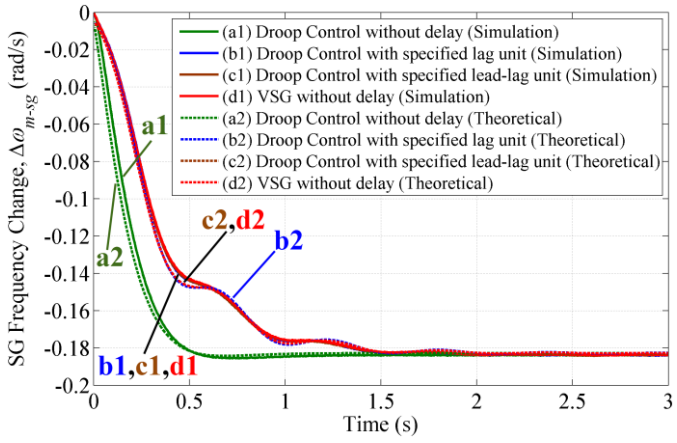

(a)

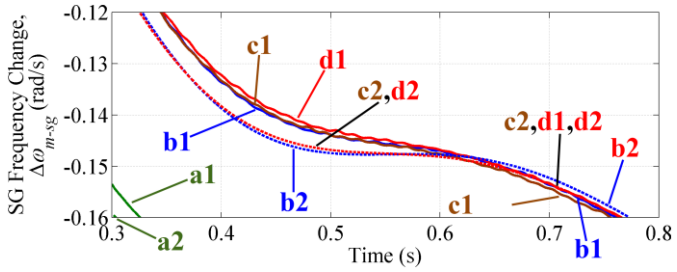

(b)

Fig. 3.21 Simulation results for the case of parallel operation with a SG to verify Fig. 3.13.

transmission lines is taken into account in the simulation, as shown in Figs. 3.15 and 3.16.

It should be noticed that for the case of "droop control without delay", a first-order filter with the time constant set to 0.005 s is applied in simulations (and in experiments discussed in next section), otherwise noises in $\Delta\omega_{m\_dg}$ would be very large. Even with the filter, ripples can still be observed in Figs. 3.17 and 3.19 for this case.

As it can be observed, in all cases, simulation results (solid lines) almost overlap corresponding theoretical results (dotted lines). Therefore, it can be concluded that the small signal models are verified. By comparing the rate of change of frequency and the amplitude of oscillations of each simulation results, same conclusions can be made as in Section 3.3.

Furthermore, for the case of parallel operation with a SG (Figs. 3.19–3.21), simulation results are slightly delayed compared with theoretical results, probably because in simulation, the input disturbance ΔP_{load}, which is realized by switching on additional load, is not an ideal step due to the existence of line reactance. It can also be noted that the amplitude of oscillations in simulation results are smaller than that in theoretical results, probably because simulation circuits include line resistance, which provides additional damping for the system.

In Fig 3.21, there is still slight difference between the simulation result of droop control with specified lead-lag unit (c1) and that of VSG (d1), whereas in theoretical results, the two results should be equivalent as shown by line (c2) and line (d2). This is probably due to the presence of line resistance as mentioned above. However, the damping effect of the first-order lead unit is confirmed by comparing line (b1) with line (c1).

3.6 Experimental Results

Scale-down experiments are also executed to support the points in Section 3.3. Experimental circuits of the case of single inverter operation and that of parallel operation with a SG are shown in Figs. 3.22 and 3.23, respectively. The setup of experiment system is shown in Figs. 3.24–3.26.

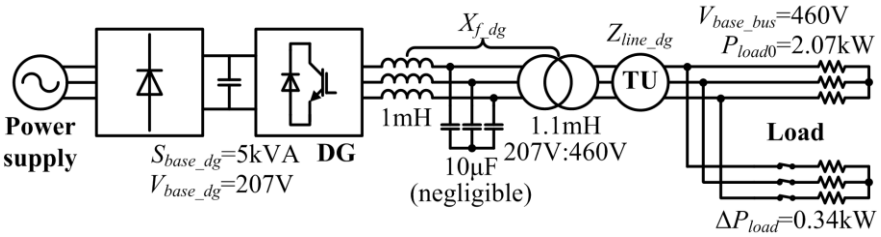

Fig. 3.22 Experimental circuit of the case of single inverter operation.

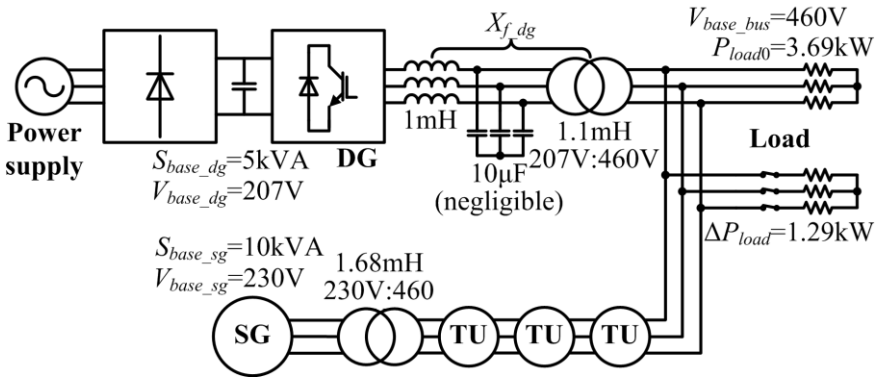

Fig. 3.23 Experimental circuit of the case of parallel operation with a SG.

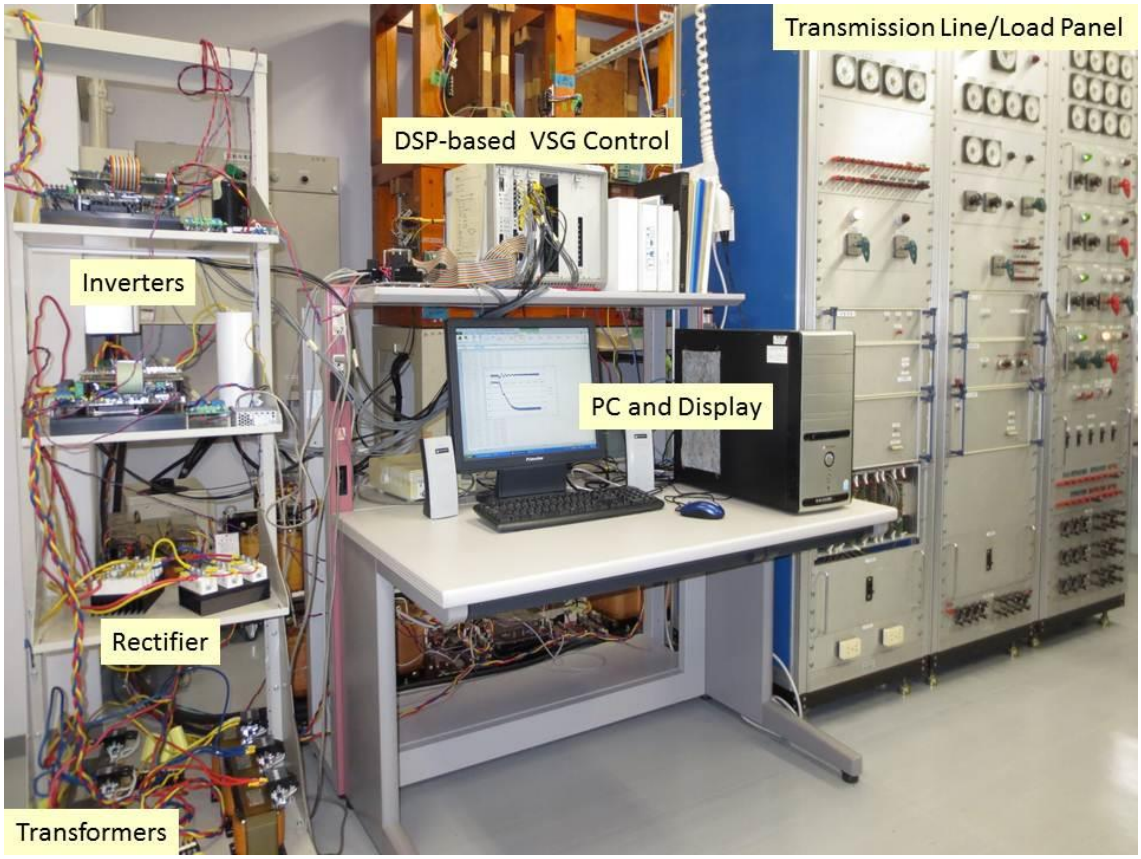

Fig. 3.24 Photo of Inverters and DSP controllers.

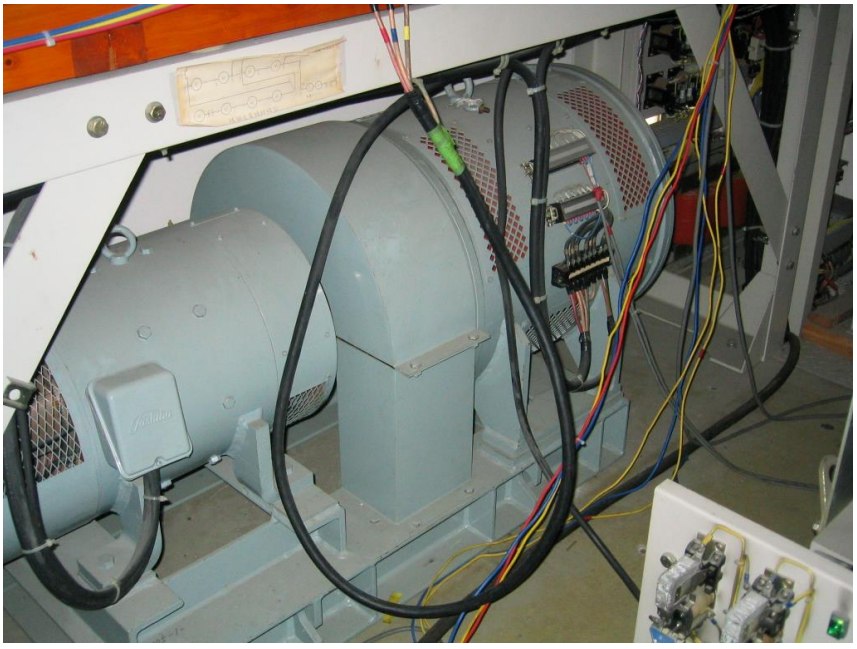

Fig. 3.25 Photo of synchronous generator moved by a dc motor.

Fig. 3.26 Photos of the load systems.

TABLE 3.3 Experimental Parameters for the Case of Single Inverter Operation

Parameter	Value	Parameter	Value
E_{dg}	207 V	J_0	0.2815 kg·m^2
S_{base_dg}	5 kVA	D_0^*	17 pu
P_{0_dg}	1 pu	δ_{dg}	0
ω_0	376.99 rad/s	V_{bus}	447.05 V
$k_{p\_dg}^*$	20 pu	ΔP_{load}	0.34 kW

TABLE 3.4 Experimental Parameters for the Case of Parallel Operation with a SG

Parameter	Value	Parameter	Value
V_{base_sg}	230 V	X_q	1.31 pu
S_{base_sg}	10 kVA	X'_q	0.55 pu
$P_{0\_sg} = P_{0\_dg}$	0 pu	X''_q	0.27 pu
ω_0	376.99 rad/s	T''_d	0.01 s
J_{sg}	0.563 kg·m2	T''_q	0.02 s
$k_{p\_sg}^*$	20 pu	I_{sg}	4.77 A
X_d	1.35 pu	φ_{sg}	0.76 rad
X'_d	0.48 pu	V_{bus}	454.8 V
X''_d	0.27 pu	ΔP_{load}	1.29 kW

Other DG parameters are the same as those in Table 3.3

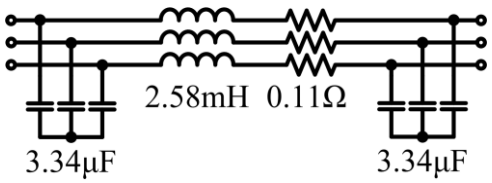

Fig. 3.27 Transmission Unit (TU).

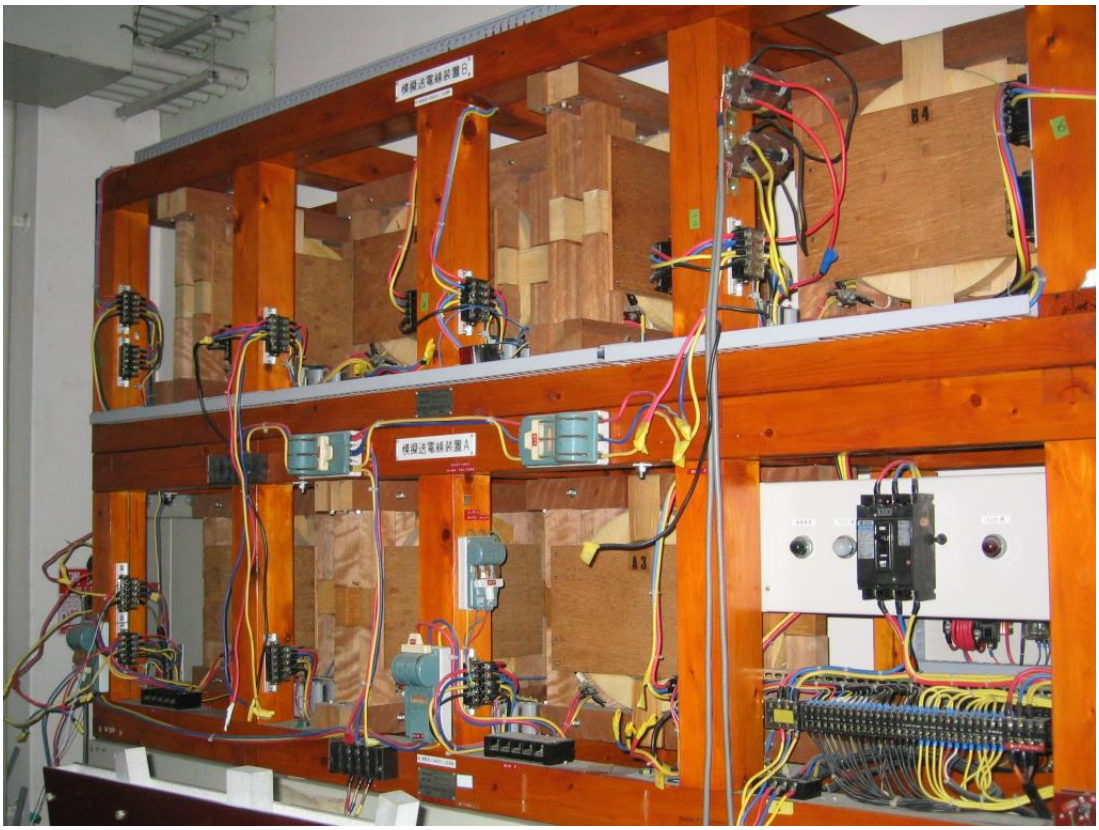

Fig. 3.28 Photo of Transmission Units.

Three-phase power supply rectified by a diode bridge is used to imitate the dc output of a DG. The block "transmission unit (TU)" in these graphs is a Π circuit to simulate a section of 40 km HV transmission line, which is illustrated in Fig. 3.27 and its photo is shown in Fig. 3.28. Parameters of the case of single inverter operation and that of parallel operation with a SG are listed in Tables 3.3 and 3.4, respectively, and the results are shown in Figs. 3.29–3.33.

For the case of single inverter operation, experimental results (solid lines) coincide with corresponding theoretical results (dotted lines). This proves again that the small-signal models and the conclusions discussed in Section 3.3 are correct.

For the case of parallel operation with a SG, by comparing each case of experimental results, the same conclusions can be drawn as those in Section 3.3. In Fig. 3.31, system with VSG control still results in slower frequency change than that with droop control, and the frequency changes faster when J_{dg} decreases. In Fig. 3.32 it can still be noticed that the delay ($T_{d\_dg} = 0.1$ s) makes the fre-

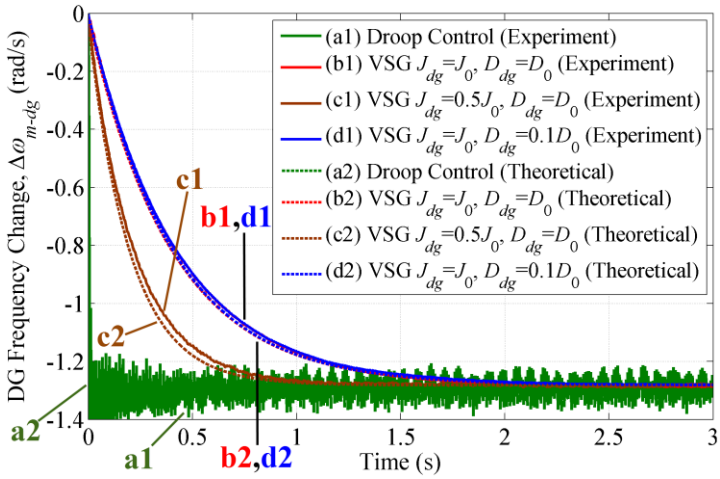

Fig. 3.29 Experimental results for the case of single inverter operation to verify effects of parameters.

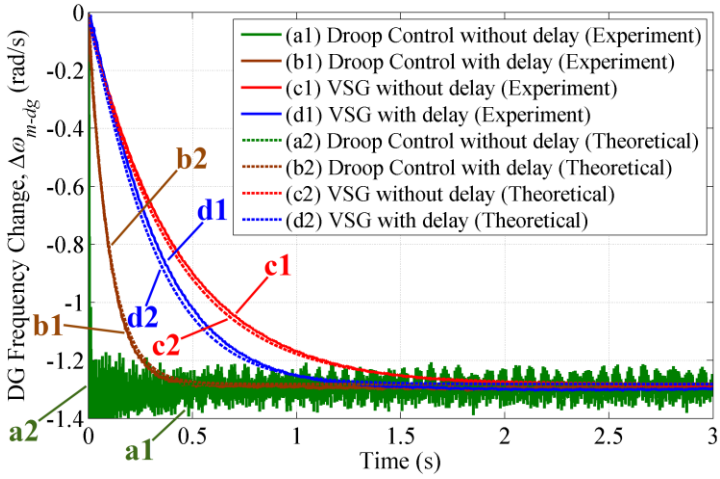

Fig. 3.30 Experimental results for the case of single inverter operation to verify effects of delays.

quency change faster in VSG control, but makes the frequency change more slowly in droop control. Similarly, in Fig. 3.33, with specified lag unit or lead-lag unit, droop control has similar dynamic response to VSG. Although in experimental results, it is difficult to confirm the difference in amplitude of oscillations due to noises and insufficient measurement resolution, simulation results are enough to confirm author's points.

3.7 Conclusion

In this chapter, small-signal models of VSG control and of droop control were built, for both cases of single inverter operation and parallel operation with a SG, to compare the dynamic responses of the two control methods. All results were verified by simulations and experiments. Oscillation phenomena were studied through state-space models. Results are summarized as follows.

(1) It was demonstrated that VSG has larger inertia than droop control and therefore better frequency stability, and the amount of inertia depends on virtual moment of inertia J whereas the damping ratio depends on damping factor D and output reactance X. It was also proved

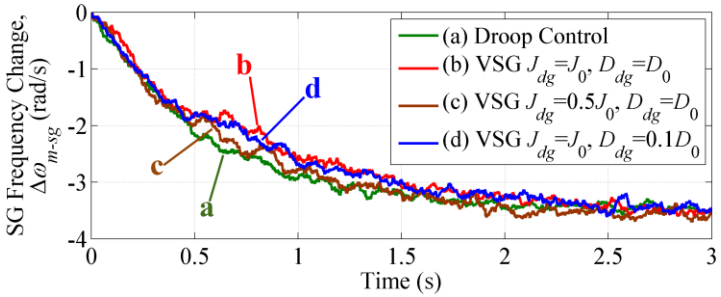

Fig. 3.31 Experimental results for the case of parallel operation with a SG to verify effects of parameters.

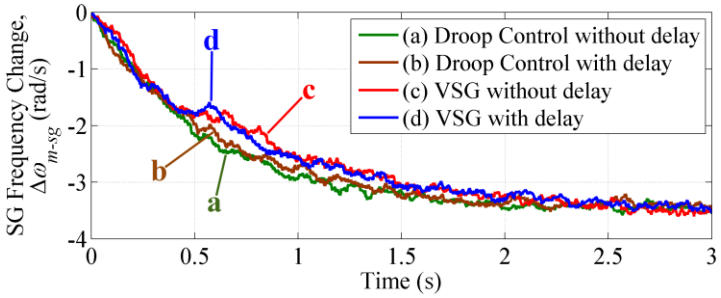

Fig. 3.32 Experimental results for the case of parallel operation with a SG to verify effects of delays.

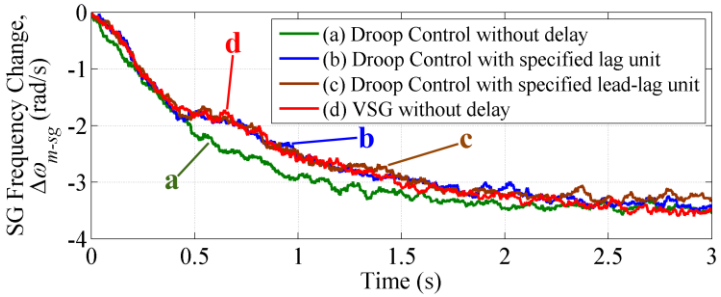

Fig. 3.33 Experimental results for the case of parallel operation with a SG to verify inertial droop control.

that the delay in governor of VSG reduces the inertia and amplifies oscillation. As a result, it is recommended to remove governor delay from VSG control. Contrarily, delay in *P* droop controller of droop control can increase the inertia.

(2) It was shown that droop control with a well-designed first-order lead-lag unit in *P* droop controller has equivalent small-signal model to that of VSG control. This modified droop control, which can be called inertial droop control, provides a novel solution of virtual inertia, which is more familiar to engineers working on UPS and microgrid applications.

(3) It was also pointed out that the output active power of VSG is more oscillatory than that of droop control, but this problem can be solved by tuning the damping factor and/or the output

reactance. Besides, it was proved that active power controls of both VSG control and droop control are stable.

(4) It was shown that VSG control and the proposed inertial droop control inherit the advantages of droop control, and in addition, provides inertia support for the system. This implies that in the applications where inertia is an important index, e.g. in microgrids, VSG control and the proposed inertial droop control have the potential to replace conventional inertia-less droop control.

(5) The small-signal models and state-space models presented in this chapter provide novel analytical approaches for understanding the dynamic characteristics of VSG and droop control, which may stimulate new ideas on improving dynamic performances of both control methods, e.g. the method to improve transient active power performance of parallel inverters presented in next chapter.

References

[1] J. Liu, Y. Miura, and T. Ise, "Dynamic characteristics and stability comparisons between virtual synchronous generator and droop control in inverter-based distributed generators," in *Proc. Int. Power Electron. Conf. (IPEC-Hiroshima ECCE-Asia)*, 2014, pp. 1536–1543.

[2] J. Liu, Y. Miura, and T. Ise, "Comparison of dynamic characteristics between virtual synchronous generator and droop control in inverter-based distributed generators," *IEEE Trans. Power Electron.*, vol. 31, no. 5, pp. 3600–3611, May 2016.

[3] M. Guan, W. Pan, J. Zhang, Q. Hao, J. Cheng, and X. Zheng, "Synchronous generator emulation control strategy for voltage source converter (VSC) stations," *IEEE Trans. Power Syst.*, vol. 30, no. 6, pp. 3093–3101, Nov. 2015.

[4] Y. Du, J. M. Guerrero, L. Chang, J. Su, and M. Mao, "Modeling, analysis, and design of a frequency-droop-based virtual synchronous generator for microgrid applications," in *Proc. IEEE ECCE Asia Downunder*, 2013, pp. 643–649.

[5] M. C. Chandorkar, D. M. Divan, and R. Adapa, "Control of parallel connected inverters in standalone ac supply systems," *IEEE Trans. Ind. Appl.*, vol. 29, no. 1, pp. 136–143, Jan./Feb. 1993.

[6] K. Debrabandere, B. Bolsens, J. Van den Keybus, A.Woyte, J. Driesen, and R. Belmans, "A voltage and frequency droop control method for parallel inverters," *IEEE Trans. Power Electron.*, vol. 22, no. 4, pp. 1107–1115, Jul. 2007.

[7] H. Nikkhajoei and R. H. Lasseter, "Distributed generation interface to the CERTS microgrid," *IEEE Trans. Power Del.*, vol. 24, no. 3, pp. 1598–1608, Jul. 2009.

[8] A. Engler and N. Soultanis, "Droop control in LV-grids," in *Proc. Int. Conf. Future Power Syst.*, 2005, pp. 1–6.

[9] J. M. Guerrero, J. Matas, L. G. De Vicuña, M. Castilla, and J. Miret, "Decentralized control for parallel operation of distributed generation inverters using resistive output impedance," *IEEE Trans. Ind. Electron.*, vol. 54, no. 2, pp. 994–1004, Apr. 2007.

[10] T. L. Vandoorn, B. Meersman, L. Degroote, B. Renders, and L. Vandevelde, "A control strategy for islanded microgrids with dc-link voltage control," *IEEE Trans. Power Del.*, vol. 26, no. 2, pp. 703–713, Apr. 2011.

[11] T. L. Vandoorn, B. Meersman, J. D. M. De Kooning, and L. Vandevelde, "Analogy between conventional grid control and islanded microgrid control based on a global DC-link voltage droop," *IEEE Trans. Power Del.*, vol. 27, no. 3, pp. 1405–1414, Jul. 2012.

[12] Y. Li and Y. W. Li, "Power management of inverter interfaced autonomous microgrid based on virtual frequency-voltage frame," *IEEE Trans. Smart Grid*, vol. 2, no.1, pp. 30–40, Mar. 2011.

[13] J. A. Peças Lopes, C. L. Moreira, and A. G. Madureira, "Defining control strategies for MicroGrids islanded operation,"," *IEEE Trans. Power Syst.*, vol. 21, no. 2, pp. 916–924, May 2006.

[14] J. C Vasquez, J. M. Guerrero, M. Savaghebi, J. Eloy-Garcia, and R. Teodorescu, "Modeling, analysis, and design of stationary-reference-frame droop-controlled parallel three-phase voltage source inverters," *IEEE Trans. Ind. Electron.*, vol. 60, no. 4, pp. 1271–1280, Apr. 2013.

[15] J. M. Guerrero, J. C. Vasquez, J. Matas, L. G. De Vicuña, and M. Castilla, "Hierarchical control of droop-controlled DC and AC microgrids—A general approach towards standardization," *IEEE Trans. Ind. Electron.*, vol. 58, no. 1, pp. 158–172, Jan. 2011.

[16] A. Bidram and A. Davoudi, "Hierarchical structure of microgrids control system," *IEEE Trans. Smart Grid*, vol. 3, no. 4, pp. 1963–1976, Dec. 2012.

[17] Q. Shafiee, J. M. Guerrero, and J. C. Vasquez, "Distributed secondary control for islanded microgrids — a novel approach," *IEEE Trans. Power Electron.*, vol. 29, no. 2, pp. 1018–1031, Feb. 2014.

[18] A. Micallef, M. Apap, C. Spiteri-Staines, J. M. Guerrero, and J. C. Vasquez, "Reactive power sharing and voltage harmonic distortion compensation of droop controlled single phase islanded microgrids," *IEEE Trans. Smart Grid*, vol. 5, no. 3, pp. 1149–1158, May 2014.

[19] J. He and Y. W. Li, "An enhanced microgrid load demand sharing strategy," *IEEE Trans. Power Electron.*, vol. 27, no. 9, pp. 3984–3995, Sept. 2012.

[20] J. He, Y. W. Li, and F. Blaabjerg, "An enhanced islanding microgrid reactive power, imbalance power, and harmonic power sharing scheme," *IEEE Trans. Power Electron.*, vol. 30, no. 6, pp. 3389–3401, Jun. 2015.

[21] H. Mahmood, D. Michaelson, and J. Jiang, "Accurate reactive power sharing in an islanded microgrid using adaptive virtual impedances," *IEEE Trans. Power Electron.*, vol. 30, no. 3, pp. 1605–1617, Mar. 2015.

[22] H. Han, Y. Liu, Y. Sun, M. Su, and J. M. Guerrero, "An improved droop control strategy for reactive power sharing in islanded microgrid," *IEEE Trans. Power Electron.*, vol. 30, no. 6, pp. 3133–3141, Jun. 2015.

[23] J. He, Y. W. Li, J. M. Guerrero, F. Blaabjerg, and J. C. Vasquez, "An islanding microgrid power sharing approach using enhanced virtual impedance control scheme," *IEEE Trans. Power Electron.*, vol. 28, no. 11, pp. 5272–5282, Nov. 2013.

[24] Y. W. Li and C.-N. Kao, "An accurate power control strategy for power-electronics-interfaced distributed generation units operating in a low-voltage multibus microgrid," *IEEE Trans. Power Electron.*, vol. 24, no. 12, pp. 2977–2988, Dec. 2009.

[25] W. Yao, M. Chen, J. M. Guerrero, and Z.-M. Qian, "Design and analysis of the droop control method for parallel inverters considering the impact of the complex impedance on the power sharing," *IEEE Trans. Ind. Electron.*, vol. 58, no. 2, pp. 576–588, Feb. 2011.

[26] Q.-C. Zhong, "Robust droop controller for accurate proportional load sharing among inverters operated in parallel," *IEEE Trans. Ind. Electron.*, vol. 60, no. 4, pp. 1281–1290, Apr. 2013.

[27] C-.T. Lee, C-.C. Chu, and P-.T. Cheng, "A new droop control method for the autonomous operation of distributed energy resource interface converters," *IEEE Trans. Power Electron.*, vol. 28, no. 4, pp. 1980–1993, Apr. 2013.

[28] Y. Zhu, Z. Fang, F. Wang, B. Liu, and Y. Zhao, "A wireless load sharing strategy for islanded microgrid based on feeder current sensing," *IEEE Trans. Power Electron.*, vol. 30, no. 12, pp.6706–6719, Dec. 2015.

[29] M. B. Delghavi and A. Yazdani, "Islanded-mode control of electronically coupled distributed-resource units under unbalanced and nonlinear load conditions," *IEEE Trans. Power Del.*, vol. 26, no. 2, pp. 661–673, Apr. 2011.

[30] T.-L. Lee and P.-T. Cheng, "Design of a new cooperative harmonic filtering strategy for distributed generation interface converters in an islanding network," *IEEE Trans. Power Electron.*, vol. 22, no. 5, pp. 1919–1927, Sept. 2007.

[31] J. Hu, J. Zhu, D.G. Dorrell, and J. M. Guerrero, "Virtual flux droop method — a new control strategy of inverters in microgrids," *IEEE Trans. Power Electron.*, vol. 29, no. 9, pp. 4704–4711, Sept. 2014.

[32] I.-Y. Chung, W. Liu, D. A. Cartes,, E. G. Jr. Collins, and S.-I. Moon, "Control methods of inverter-interfaced distributed generators in a microgrid system," *IEEE Trans. Ind. Appl.*, vol. 46, no. 3, pp. 1078–1088, May/Jun. 2010.

[33] R. Majumder, B. Chaudhuri, A. Ghosh, R. Majumder, G. Ledwich, and F. Zare, "Improvement of stability and load sharing in an autonomous microgrid using supplementary droop control loop," *IEEE Trans. Power Syst.*, vol. 25, no. 2, pp. 796–808, May 2010.

[34] J. M. Guerrero, L. G. De Vicuña, J. Matas, M. Castilla, and J. Miret, "Output impedance design of parallel-connected UPS inverters with wireless load-sharing control," *IEEE Trans. Ind. Electron.*, vol. 52, no. 4, pp. 1126–1135, Aug. 2005.

[35] J. M. Guerrero, L. Hang, and J. Uceda, “Control of distributed uninterruptible power supply systems,” *IEEE Trans. Ind. Electron.*, vol. 55, no. 8, pp. 2845–2859, Aug. 2008.

[36] J. Machowski, J. Bialek, and J. R. Bumby, *Power System Dynamics and Stability*. New York: John Wiley & Sons, 1997, pp. 141–182.

[37] T. Shintai, Y. Miura, and T. Ise, “Oscillation damping of a distributed generator using a virtual synchronous generator,” *IEEE Trans. Power Del.*, vol. 29, no. 2, pp. 668–676, Apr. 2014.

Chapter 4

Parallel Operation of Multiple VSGs in Microgrids

4.1 Introduction

In this chapter, the application of VSG control in a microgrid composed of parallel inverter-interfaced DGs is discussed [1]. As it is discussed in Chapter 3, VSG control can be considered as a potential upgrade for the communication-less control method of a microgrid thanks to its inertia support feature. However, when VSG control is applied in microgrids, several problems have been noticed, such as oscillation in active power during a disturbance, inappropriate transient active power sharing during loading transition and errors in reactive power sharing.

Active power oscillation during a disturbance is introduced by the well-known feature of the swing equation, thus it is an inherent feature for a real SG as well as a VSG. It is not a critical problem for SGs because they usually have considerable overload capabilities, but the overload capabilities of inverter-interfaced DGs are not high enough to ride though a large oscillation. However, this oscillation can be damped by properly increasing the damping ratio [2] or using alternating moment of inertia [3]. Using smaller inertia may also lead to reduced oscillation [4]; however, it is not encouraged because providing a large amount of virtual inertia is an advantage that distinguishes VSG control from other control methods.

In this chapter, a novel method for oscillation damping is proposed based on increasing the virtual stator reactance. Due to the oscillatory feature of VSG, inappropriate transient active power sharing during loading transition may also cause oscillation, which is avoidable if the swing equation and output impedance are designed properly, as it is analyzed in this chapter. This inappropriate transient active power sharing is also reported in [5]; however, proper solution is not proposed. Sharing transient loads between SG and DG is addressed in [6]; however, theoretical analysis is not provided.

The inaccurate reactive power sharing is a well-known problem in conventional $Q-V$ droop control, and the same problem is reported in active power sharing of $P-V$ droop control. In $Q-V$ or $P-V$ droop control, output voltage is regulated according to reactive/active power sharing, but the output voltage of each DG is not equal due to unequal line voltage drop. This problem has received considerable attention in the literature, and many control strategies are proposed to address this issue [7]–[23]. A comprehensive solution is to eliminate the mismatch of DG output impedance [7], [8]; however, this method cannot guarantee accurate reactive power sharing if active power is not shared according to the power rating ratio. An approach based on line voltage drop compensation is proposed in [9]. However, a grid-connected mode operation is required for the

evaluation of line parameters, which is not feasible for an isolated microgrid. Other communication-less approaches, e.g. $Q-\mathrm{d}V/\mathrm{d}t$ droop control [10], adaptive voltage droop [11], and virtual capacitor control [12] are also proposed. However, the reactive power sharing errors cannot be completely eliminated by these methods, as it is demonstrated in respective experimental results. In some approaches, communication is used to improve reactive power sharing accuracy, such as secondary control signals from MGCC [13]–[18], master-slave communication [19], and communication between DGs [20]. However, as accurate reactive power sharing is a basic function of a microgrid, it is always preferred to solve this problem in a communication-less manner considering the probable communication fault.

In this chapter, a communication-less approach is proposed based on the inversed voltage droop ($V-Q$ droop) feature of VSG control and common ac bus voltage estimation. By applying the proposed method, reactive power sharing is immune to line impedance mismatch and active power sharing change. The idea to use ac bus voltage as a common reference shares some similarities with the approaches presented in [21]–[23]. However, in these works, measured bus voltage is used directly, whereas it may not be feasible in microgrid applications if DGs are not installed in the proximity of the ac bus. In this chapter, bus voltage is estimated based on the available local measurement, thus there should be no installation difficulty in field applications.

The rest of this chapter is organized as follows. In Section 4.2, a state-space model of islanded microgrid using VSG control is built, and the principle of the proposed oscillation damping method is derived from eigenvalue analysis of this model. Proper parameter design for appropriate transient load sharing based on poles-zeros cancellation is also discussed based on the same model. In Section 4.3, the cause of reactive power sharing errors is discussed and a novel accurate reactive power sharing method is proposed. The enhanced VSG control strategy based on aforementioned discussion is presented in Section 4.4. Simulation and experiment results are shown in Sections 4.5 and 4.6, respectively. Finally, conclusions are given in Section 4.7.

4.2 Analyses of Transient Active Power Performance

4.2.1 Closed-Loop State-Space Model

In this chapter, an islanded microgrid which consists of two DGs using VSG control is studied, as it is shown in Fig. 4.1. The DGs are connected to a common ac bus via distribution lines, to supply the loads inside the microgrid. Note that the capacitor of the DG output LC filter in Fig. 2.2 is neglected, as its susceptance is usually negligible at fundamental frequency.

In order to understand the causes of active power oscillation and to find proper solutions, a state-space model for the closed-loop active power control of the microgrid shown in Fig. 4.1 can be obtained as given in (4.1)–(4.8) with a deduction process same as that shown in Section 3.4. As it is concluded that the governor delay should be removed in Chapter 3, the governor first-order lag unit

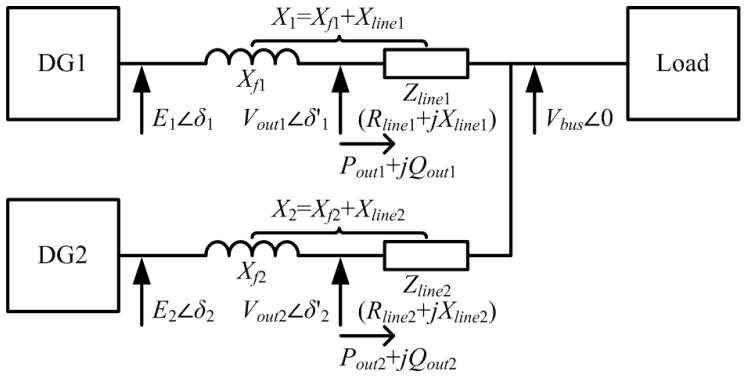

Fig. 4.1 Structure of a microgrid composed of two DGs in islanded mode.

is removed by setting $T_d = 0$ in this chapter. Therefore, the rank of the state-space model is reduced to 3 as shown in the following equations.

$$\begin{cases} \dot{\boldsymbol{x}} = \boldsymbol{A}\boldsymbol{x} + \boldsymbol{B}\boldsymbol{w} \\ \boldsymbol{y} = \boldsymbol{C}\boldsymbol{x} + \boldsymbol{D}\boldsymbol{w} \end{cases}, \tag{4.1}$$

where

$$\boldsymbol{w} = [\Delta P_{load} \quad \Delta P_{0\_1} \quad \Delta P_{0\_2}]^T \tag{4.2}$$

$$\boldsymbol{y} = [\Delta\omega_{m1} \quad \Delta\omega_{m2} \quad \Delta P_{out1} \quad \Delta P_{out2}]^T \tag{4.3}$$

$$\boldsymbol{x} = \begin{bmatrix} \Delta\omega_{m1} + \dfrac{D_1}{J_1\omega_0(K_1+K_2)}\Delta P_{load} \\ \Delta\omega_{m2} + \dfrac{D_2}{J_2\omega_0(K_1+K_2)}\Delta P_{load} \\ \Delta\delta_1 - \dfrac{1}{K_1+K_2}\Delta P_{load} \end{bmatrix} \tag{4.4}$$

$$\boldsymbol{A} = \begin{bmatrix} -\dfrac{D_1K_2}{J_1\omega_0(K_1+K_2)} - \dfrac{k_{p1}}{J_1\omega_0} & \dfrac{D_1K_2}{J_1\omega_0(K_1+K_2)} & -\dfrac{K_1}{J_1\omega_0} \\ \dfrac{D_2K_1}{J_2\omega_0(K_1+K_2)} & -\dfrac{D_2K_1}{J_2\omega_0(K_1+K_2)} - \dfrac{k_{p2}}{J_2\omega_0} & \dfrac{K_1}{J_2\omega_0} \\ \dfrac{K_2}{K_1+K_2} & -\dfrac{K_2}{K_1+K_2} & 0 \end{bmatrix} \tag{4.5}$$

$\boldsymbol{B}$

$$= \begin{bmatrix} -\dfrac{K_1}{J_1\omega_0(K_1+K_2)} - \dfrac{D_1D_2K_2}{J_1J_2\omega_0^2(K_1+K_2)^2} + \dfrac{D_1^2K_2}{J_1^2\omega_0^2(K_1+K_2)^2} + \dfrac{D_1k_{p1}}{J_1^2\omega_0^2(K_1+K_2)} & \dfrac{1}{J_1\omega_0} & 0 \\ -\dfrac{1}{J_2\omega_0} + \dfrac{K_1}{J_2\omega_0(K_1+K_2)} - \dfrac{D_1D_2K_1}{J_1J_2\omega_0^2(K_1+K_2)^2} + \dfrac{D_2^2K_1}{J_2^2\omega_0^2(K_1+K_2)^2} + \dfrac{D_2k_{p2}}{J_2^2\omega_0^2(K_1+K_2)} & 0 & \dfrac{1}{J_2\omega_0} \\ -\dfrac{D_1K_2}{J_1\omega_0(K_1+K_2)^2} + \dfrac{D_2K_2}{J_2\omega_0(K_1+K_2)^2} & 0 & 0 \end{bmatrix} \tag{4.6}$$

$$\boldsymbol{C} = \begin{bmatrix} 1 & 0 & 0 \\ 0 & 1 & 0 \\ 0 & 0 & K_1 \\ 0 & 0 & -K_1 \end{bmatrix} \tag{4.7}$$

$$\boldsymbol{D} = \begin{bmatrix} -\dfrac{D_1}{J_1\omega_0(K_1+K_2)} & 0 & 0 \\ -\dfrac{D_2}{J_2\omega_0(K_1+K_2)} & 0 & 0 \\ \dfrac{K_1}{K_1+K_2} & 0 & 0 \\ \dfrac{K_2}{K_1+K_2} & 0 & 0 \end{bmatrix} \tag{4.8}$$

where subscript $i = 1,2$ indicates the ith DG. Here, $K_i = (E_i V_{bus}\cos\delta_i)/X_i$, and $X_i \approx X_{f\,i} + X_{line\,i}$, as it is discussed in Section 3.3.1.

Analyses of transient active power control performance in the following parts of present section are based on this model, as it describes the transient performance of variables in $\boldsymbol{y}$ after a given disturbance $\boldsymbol{w}$.

4.2.2 Oscillation Damping

It is a known conclusion in the control theory that the poles of transfer function of $Y_j(s)/W_k(s)$ are available in the eigenvalues of $\boldsymbol{A}$, for any j, k Therefore, the studies on eigenvalues of $\boldsymbol{A}$ should give some clues to damping methods for oscillations in $\Delta P_{out\,i}$.

The loci of eigenvalues of $\boldsymbol{A}$ with a variation of D_1 or X_1 are shown in Fig. 4.2. Nominal parameters for the eigenvalue loci plots are listed in Table 4.1.

In the eigenvalue loci plots, radial dash lines indicate damping ratio ζ, and circle dash lines indicate undamped natural frequency ω_n. As it is shown in Fig. 4.2, damping ratio of the complex-conjugate eigenvalues increases if the damping factor D_i and/or the output reactance impedance X_i are increased. It should be pointed out that increasing X_i causes a decrease in damped natural frequency ω_d, which is indicated by the distance between eigenvalue and the real axis. This may result in longer settling time compared with the method of increasing D_i. However, the approach of increasing output reactance has other merits as follows.

(1) The state-space model is obtained under the assumption that the output impedance of DGs is inductive, as it is discussed in Section 3.3.1. This assumption is less valid if X_i is small, especially in a LV microgrid in which line impedances are mainly resistive [24]. If this assumption is not valid, the active power and reactive power control cannot be decoupled correctly and the system may become more oscillatory and even unstable.

(2) To share transient active power properly, output reactance of each DG should be designed equally in per unit value, as it is discussed in next part of this section. Therefore, the problem

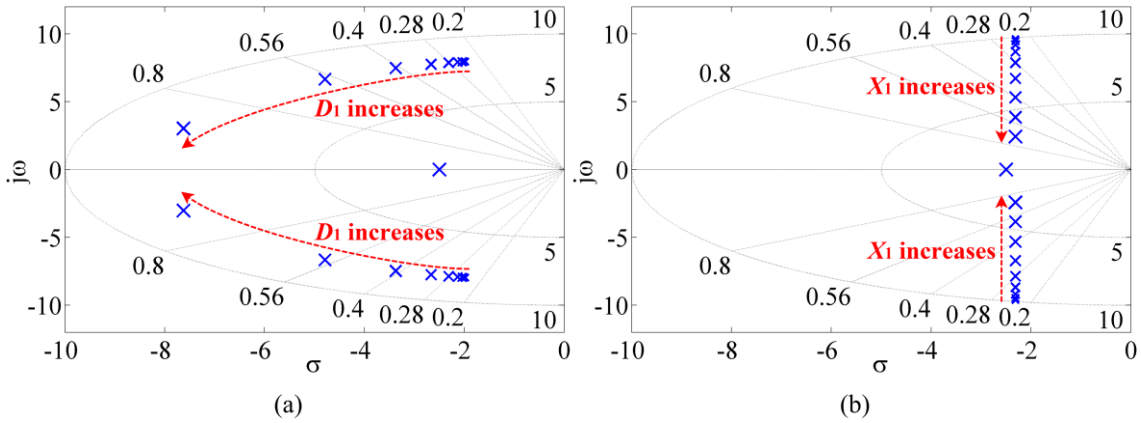

Fig. 4.2 Eigenvalue loci with a variation of

(a) D_1^* ($2^{-4} \times 17$ pu ~ $2^5 \times 17$ pu) or (b) X_1^* ($2^{-4} \times 0.7$ pu ~ $2^5 \times 0.7$ pu).

TABLE 4.1 State-Space Model Parameters

Parameter	Value	Parameter	Value
S_{base1}	10 kVA	M_i^*	8 s
S_{base2}	5 kVA	D_i^*	17 pu
E_0	200 V	$k_{p\,i}^*$	20 pu
ω_0	376.99 rad/s	X_i^*	0.7 pu
$E_i = V_{bus}$	200 V	$\cos\theta_i$	≈1

of oscillation and that of transient active power sharing can be solved simultaneously by proper stator reactance design.

(3) Moreover, the influence of output reactance mismatch on transient active power sharing becomes smaller if output reactance of DGs is increased, owing to decreased relative errors.

4.2.3 Transient Active Power Sharing

If the disturbance comes from a loading transition, the disturbance vector can be written as $\boldsymbol{w} = [\Delta P_{load} \quad 0 \quad 0]^{\mathrm{T}}$. The output vector at $t = 0^+$ can be calculated through (4.9).

$$\boldsymbol{y}(0^+) = \boldsymbol{D}\boldsymbol{w} \tag{4.9}$$

From (4.9), the transient active power sharing at $t = 0^+$ is obtained as

$$\Delta P_{out1}(0^+) = \frac{K_1}{K_1 + K_2}\Delta P_{load}, \tag{4.10}$$

$$\Delta P_{out2}(0^+) = \frac{K_2}{K_1 + K_2}\Delta P_{load}. \tag{4.11}$$

The output vector at steady state can be calculated through (4.12).

$$\boldsymbol{y}(\infty) = (\boldsymbol{D} - \boldsymbol{C}\boldsymbol{A}^{-1}\boldsymbol{B})\boldsymbol{w} \tag{4.12}$$

From (4.12), the steady-state active power sharing is obtained as

$$\Delta P_{out1}(\infty) = \frac{k_{p1}}{k_{p1} + k_{p2}} \Delta P_{load}. \tag{4.13}$$

$$\Delta P_{out2}(\infty) = \frac{k_{p2}}{k_{p1} + k_{p2}} \Delta P_{load}. \tag{4.14}$$

The transient power sharing should be equivalent to the steady-state power sharing, in order to avoid unnecessary transient oscillation. Therefore,

$$\frac{k_{p1}}{k_{p2}} = \frac{K_1}{K_2} = \frac{(E_1 V_{bus} \cos\delta_1)/X_1}{(E_2 V_{bus} \cos\delta_2)/X_2}. \tag{4.15}$$

Knowing that $k_{p\,i}^* = (k_{p\,i}\omega_0)/S_{base\,i}$, $X_i^* = (X_i S_{base\,i})/E_0^2$, and supposing $E_i \approx V_{bus} \approx E_0$, $\cos\delta_i \approx 1$, thus

$$\frac{X_1^*}{X_2^*} = \frac{k_{p2}^*}{k_{p1}^*}. \tag{4.16}$$

As it is mentioned in Section 2.3.2, $k_{p\,i}^*$ is designed equally so that the active power is shared according to power ratings of DGs in steady state [25]. Therefore,

$$X_1^* = X_2^*. \tag{4.17}$$

Equation (4.17) is the condition for appropriate transient power sharing at $t = 0^+$. This conclusion can be verified by evaluating the poles and zeros of $\frac{\Delta P_{out1}(s)}{\Delta P_{load}(s)}$ and $\frac{\Delta P_{out2}(s)}{\Delta P_{load}(s)}$, as it is demonstrated in Fig. 4.3(a). $\frac{\Delta P_{out1}(s)}{\Delta P_{load}(s)}$ and $\frac{\Delta P_{out2}(s)}{\Delta P_{load}(s)}$ can be obtained as the elements $G_{31}(s)$ and $G_{41}(s)$ of the matrix $\boldsymbol{G}(s)$ shown in (4.18), respectively.

$$\boldsymbol{G}(s) = \boldsymbol{C}(s\boldsymbol{I} - \boldsymbol{A})^{-1}\boldsymbol{B} + \boldsymbol{D} \tag{4.18}$$

Fig. 4.3(a) shows that if (4.17) holds, all poles of $\frac{\Delta P_{out1}(s)}{\Delta P_{load}(s)}$ and $\frac{\Delta P_{out2}(s)}{\Delta P_{load}(s)}$ are cancelled by zeros, and if (4.17) does not hold, this cancellation does not happen for the complex-conjugate poles. The cancellation of all poles implies a desirable step change of ΔP_{out1} and ΔP_{out2} directly to their respective steady-state values without any oscillation during a loading transition.

However, (4.17) can only guarantee appropriate power sharing at $t = 0^+$. The transient state during the first several seconds after $t = 0^+$ depends on the swing equation parameters, i.e. moment of inertia and damping factor. As it is shown in Figs. 4.3(b) and 4.3(c), if the inertia constant M_i^* and the per unit damping ratio D_i^* are not designed equally, the cancellation of poles and zeros

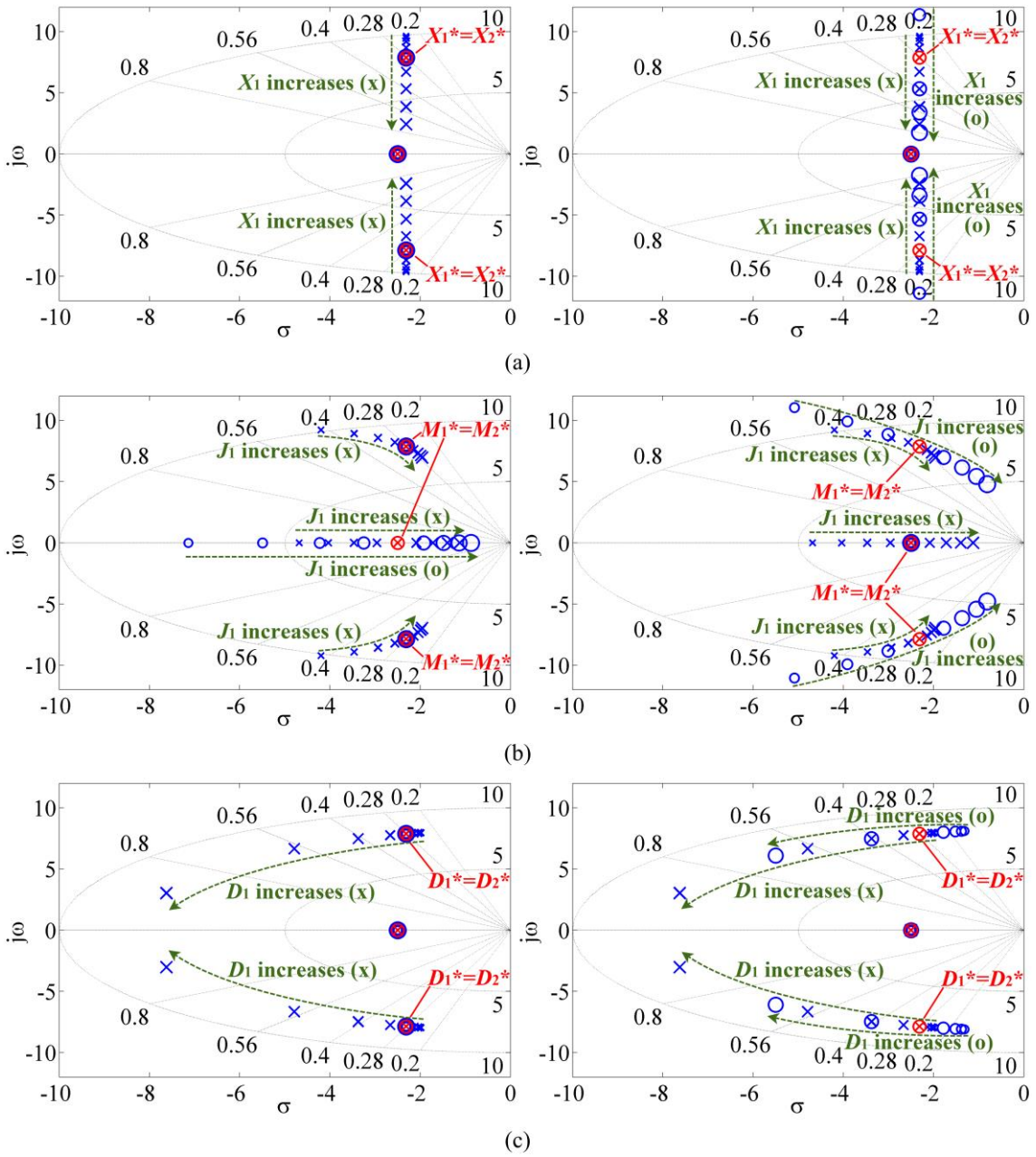

Fig. 4.3 Poles and zeros of $\frac{\Delta P_{out1}(s)}{\Delta P_{load}(s)}$ in the left column and $\frac{\Delta P_{out2}(s)}{\Delta P_{load}(s)}$ in the right column with a variation of (a) X_1^* ($2^{-4} \times 0.7$ pu ~ $2^5 \times 0.7$ pu) (b) M_1^* ($1.3^{-4} \times 8$ s ~ $1.3^5 \times 8$ s) or (c) D_1^* ($2^{-4} \times 17$ pu ~ $2^5 \times 17$ pu).

does not happen, either. That is to say, to obtain ideal transient active power sharing, (4.19) and (4.20) should also be guaranteed.

$$M_1^* = M_2^*. \tag{4.19}$$

$$D_1^* = D_2^*. \tag{4.20}$$

Equations (4.19) and (4.20) are not difficult to realize since M_i^* and D_i^* are virtual parameters that can be easily changed in the control program. As for (4.17), a control method to adjust stator reactance is presented in Section 4.4.

4.3 Improvement of Reactive Power Sharing

Fig. 4.4 shows the principles of $\omega - P$ and $V - Q$ droop controls in the "Governor Model" and "Q Droop" blocks shown in Figs. 2.5 and 2.6, for the case of $S_{base1}: S_{base2} = 2:1$. As discussed in Section 2.3.2, k_p^*, k_q^*, P_0^* and Q_0^* are designed equally. Based on the predefined linear droop control laws, the desired power sharing $P_{in1}: P_{in2} = 2:1$ can be obtained because the governor input is ω_m, and $\omega_{m1} = \omega_{m2}$ is guaranteed in steady state.

Following the same principle, to share the reactive power according to the power rating ratio, an equal voltage reference is required. However, for the $V - Q$ droop in the basic VSG control shown in Fig. 2.6, the voltage reference is the line-to-line RMS value of the inverter output voltage, which may be a different value for each DG even in steady state due to the line voltage drop. As most of previous studies are based on $Q - V$ droop, in which the output voltage $V_{out\,i}$ should be regulated based on measured reactive power $Q_{out\,i}$, the basic idea to address this problem is to equalize $V_{out\,i}$ by equalizing the output impedance [7], [8], or by compensating the line voltage drop [9]. Both methods need great effort in design process and complex computations in DG control programs, whereas the resulted reactive power sharing is still influenced by active power sharing. As the voltage does not need to be controlled directly in a $V - Q$ droop control scheme shown in Fig. 2.2, the reference voltage can be chosen other than inverter output voltage. If the line-to-line RMS value of the common ac bus voltage V_{bus} is used instead of the inverter output voltage $V_{out\,i}$, equal reactive power reference value $Q_{ref1} = Q_{ref2}$ can be guaranteed, as it is illustrated in Fig. 4.4. Therefore, accurate reactive power sharing $Q_{out1} = Q_{out2}$ should be obtained through the using of reactive power PI controller. Moreover, unlike the inverter output voltage, the bus voltage is not influenced by line voltage drop, which is determined by both active and reactive power. Therefore, reactive power sharing according to the bus voltage is independent from active power.

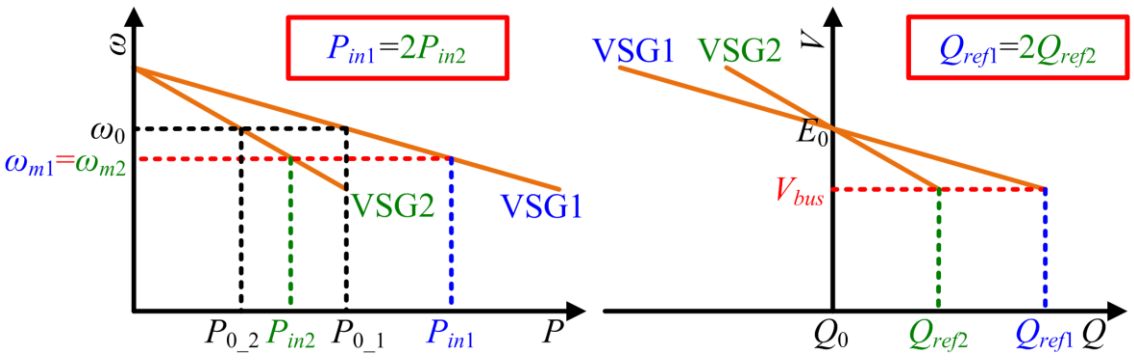

Fig. 4.4 Principles of $\omega - P$ and $V - Q$ droop control.

In some previous researches [21]–[23], direct bus voltage measurement is suggested. However, in field applications, it is difficult to measure V_{bus} directly, as DGs may be installed far away from the common ac bus, and the utilization of communication is not preferred for reliability reason. Therefore, a bus voltage estimation method using local measurement is proposed in next section.

4.4 The Proposed Enhanced VSG Control Scheme

The proposed enhanced VSG control scheme is shown in Fig. 4.5. Compared with the basic VSG control, two major modifications are made, i.e., the stator impedance adjuster and the bus voltage estimator, as shown in Figs. 4.6 and 4.7, respectively.

In order to facilitate the algorithm in the stator impedance adjuster and the bus voltage estimator, the measured three-phase output voltage and current are converted to αβ frame. As a result, the calculation in the power meter should be based on αβ-frame components instead of three-phase components. Therefore, (2.6) and (2.7) should be replaced by (4.21) and (4.22).

$$P_{out} = v_{out\_\alpha} i_{out\_\alpha} + v_{out\_\beta} i_{out\_\beta} \tag{4.21}$$

$$Q_{out} = -v_{out\_\alpha} i_{out\_\beta} + v_{out\_\beta} i_{out\_\alpha} \tag{4.22}$$

The function of stator impedance adjuster shown in Fig. 4.6 is to adjust the output reactance of the DG freely. It is operating as a virtual impedance controller. The transformation from ρθ frame to αβ frame and the inverse transformation used in Fig. 4.6 and the following part of this dissertation are defined in (4.23) and (4.24).

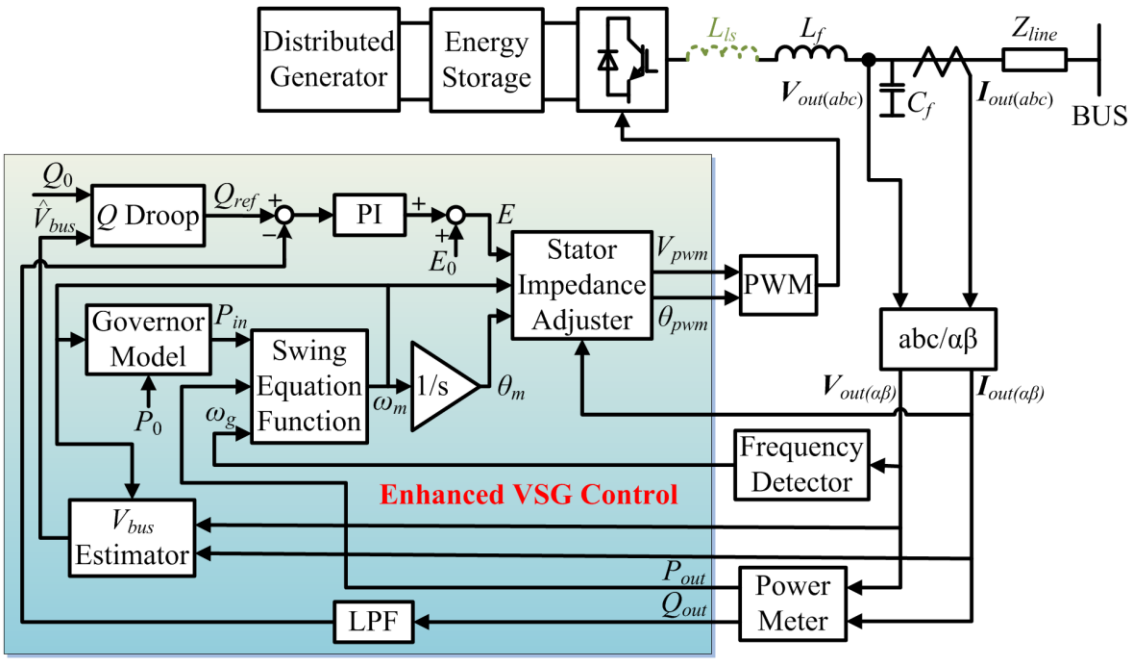

Fig. 4.5 Block diagram of the proposed enhanced VSG control.

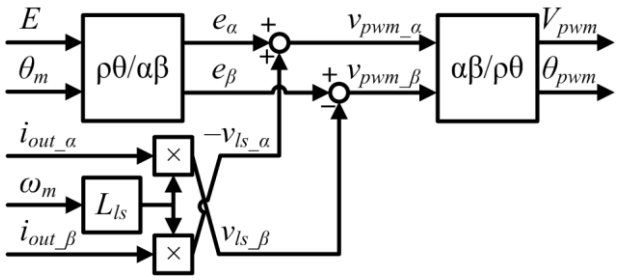

Fig. 4.6 Block diagram of the "Stator Impedance Adjuster" block of the enhanced VSG control.

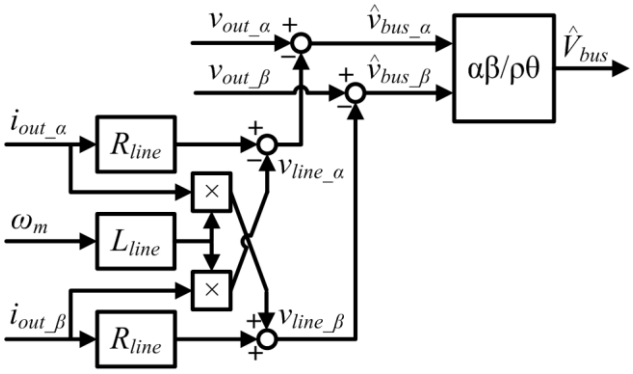

Fig. 4.7 Block diagram of the "V_{bus} Estimator" block of the enhanced VSG control.

$$\begin{bmatrix}\alpha\\ \beta\end{bmatrix} = \begin{bmatrix}\rho\cos\theta\\ \rho\sin\theta\end{bmatrix} \tag{4.23}$$

$$\begin{bmatrix}\rho\\ \theta\end{bmatrix} = \begin{bmatrix}\sqrt{\alpha^2+\beta^2}\\ \tan^{-1}\dfrac{\beta}{\alpha}\end{bmatrix} \tag{4.24}$$

The virtual stator inductor is realized by multiplying output current by the virtual stator inductor L_{ls} in αβ frame. It will be more accuracy if inductor current through L_f is used. However, this will increase the number of current sensors, which is not necessary. As the current flowing into C_f at fundamental frequency is less than few percent of the inductor current, using output current instead of inductor current does not affect the performance of the control scheme.

Based on the given analyses in Section 4.2, tuning method of virtual stator inductor L_{ls} is suggested to set total output reactance X_i^* for both DGs in same large per unit value, as shown in (4.25). This approach increases active power damping ratio and shares transient load without oscillation. The target value is proposed to be 0.7 pu because it is a typical value for the total direct-axis transient reactance X'_d of a real SG.

$$X_i^* = S_{base\,i}\omega_{m\,i}(L_{ls\,i} + L_{f\,i} + L_{line\,i})/E_0^2 = 0.7 \text{ pu} \tag{4.25}$$

The $L_{f\,i}$ and $Z_{line\,i}$ $(R_{line\,i} + jL_{line\,i})$ are considered as known parameters in this paper. As the scale of microgrid is usually small, the line distance is easily to be measured or fed by the planner.

Even if it is not the case, several online measurement or intelligent tuning methods for $Z_{line\,i}$ are available in [24] and [26].

With the proposed design of stator impedance adjustment, oscillation in a VSG-control-based microgrid should be almost eliminated during a loading transition in islanded mode. Particularly, transition from grid-connected mode to islanded mode can also be considered as a loading transition; therefore, the oscillation during an islanding event should also be eliminated with the proposed control strategy, as it is proved by simulation results in next section. As for other disturbances in islanded mode during which the power sharing ratio is changed, e.g. change of active power set value of DG(s), connection/disconnection of DG(s), etc., oscillation cannot be completely eliminated with the proposed solution, but can still be damped owing to the increased total output reactance.

The principle of the bus voltage estimator shown in Fig. 4.7 is similar to that of the stator impedance adjuster shown in Fig. 4.6. By calculating the line voltage drop in αβ frame using measured output current and line impedance data, the bus voltage can be estimated from the difference of output voltage and calculated line voltage drop. Since the line-to-line RMS value of estimated bus voltage $\hat{V}_{bus}$ for each DG should be approximately equal, as it is discussed in last section, accurate reactive power sharing can be obtained by using estimated bus voltages as the input references of "*Q* Droop" instead of respective output voltages of DGs. Although the principle of presented bus voltage estimator is not new, the idea of using this estimator to realize communication-less accurate reactive power sharing can be considered as a contribution in the present work.

The modified *Q* droop controller is shown in Fig 4.8 and can be expressed as

$$Q_{ref} = Q_0 - k_q(\hat{V}_{bus} - E_0). \tag{4.26}$$

However, if there is an estimation error in $\hat{V}_{bus}$, it will cause a reactive power sharing error. Supposing $\hat{V}^*_{bus1} = V^*_{bus} + \Delta\hat{V}^*_1$ and $\hat{V}^*_{bus2} = V^*_{bus} + \Delta\hat{V}^*_2$, substitute them into (4.26),

$$Q^*_{ref1} - Q^*_{ref2} = -k^*_q(\Delta\hat{V}^*_1 - \Delta\hat{V}^*_2). \tag{4.27}$$

In steady state, as $Q^*_{ref\,i} = Q^*_{out\,i}$,

$$Q^*_{out1} - Q^*_{out2} = -k^*_q(\Delta\hat{V}^*_1 - \Delta\hat{V}^*_2). \tag{4.28}$$

That is to say, the reactive power sharing error caused by estimation errors is determined by the *V*-*Q* droop gain k^*_q. The design of k^*_q is a well-known trade-off between voltage deviation and reactive power control accuracy. Considering the probable ripples in the measured RMS value of $\hat{V}_{bus}$, k^*_q is recommended to be 5 pu for the present example.

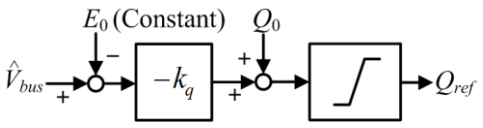

Fig. 4.8 Block diagram of the "*Q* Droop" block of enhanced VSG control.

It should be pointed out that the increased output reactance by adding the virtual stator inductor L_{ls} causes a decrease in the reactive control plant gain. From (3.7),

$$Q_{out\,i} = \frac{E_i(E_i - V_{bus}\cos\delta_i)}{X_i}. \tag{4.29}$$

The small-signal model of (4.29) is

$$\Delta Q_{out\,i} = \frac{(E_i - V_{bus}\cos\delta_i)\Delta E_i + E_i(\Delta E_i - \Delta V_{bus}\cos\delta_i)}{X_i}. \tag{4.30}$$

As $\cos\delta_i \approx 1$, $E_i \approx V_{bus} \approx E_0$, (4.30) can be simplified as

$$\Delta Q_{out\,i} = \frac{E_0(\Delta E_i - \Delta V_{bus})}{X_i}. \tag{4.31}$$

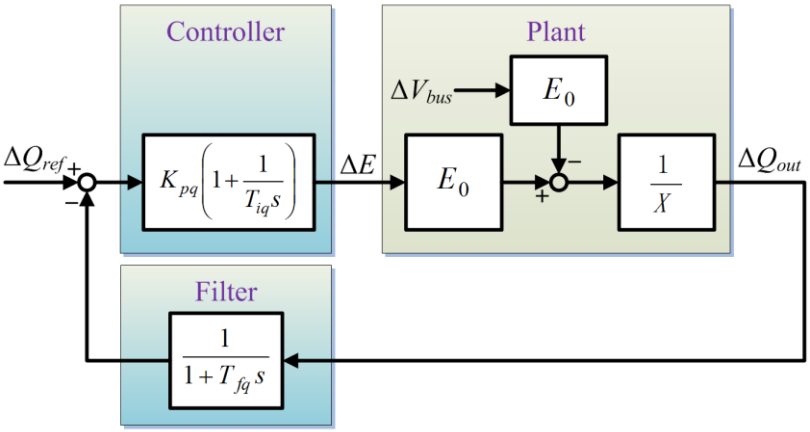

Fig. 4.9 Small-signal model of reactive power control loop.

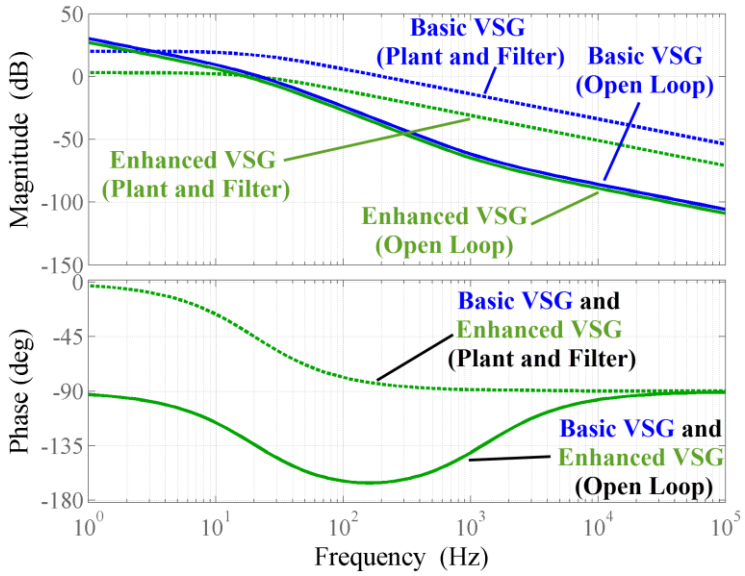

Fig. 4.10 Bode plot of reactive power control loop.

With (4.31), the small-signal model of the reactive power control part can be illustrated as Fig. 4.9. Therefore, in the enhanced VSG control where X_i is largely increased, in order to keep the bandwidth of the reactive power control loop to be 20 Hz, the gain of PI controller should be increased to compensate the decreased plant gain, as illustrated in Fig. 4.10. The parameters used to plot Fig. 4.10 are related to DG1, which are shown in Fig. 4.11 and Table 4.2. The 20Hz bandwidth is relatively low compared with control methods working on instantaneous value; however, it is fast enough to track the reactive power and regulate the output voltage as it is demonstrated in the simulation and experimental results.

4.5 Simulation Results

Simulations are executed in PSCAD/EMTDC environment to verify the effectiveness of the pro-

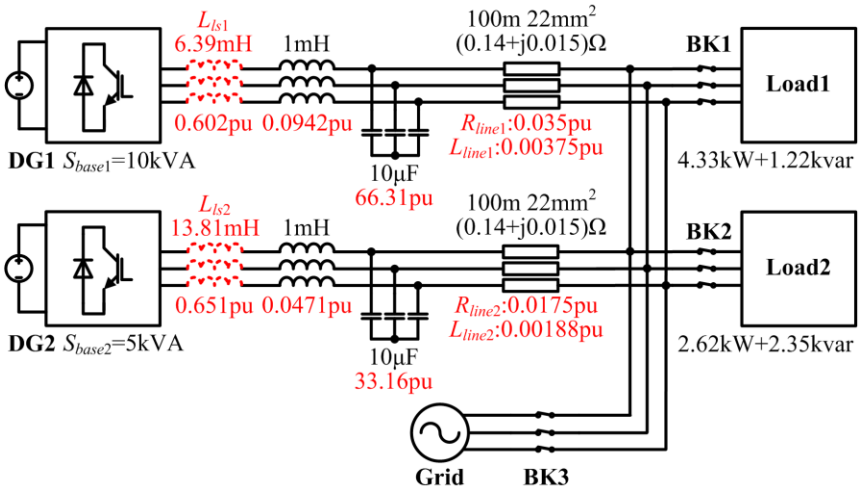

Fig. 4.11 Simulation circuit.

TABLE 4.2 Simulation Parameters

Common Parameters			
Parameter	Value	Parameter	Value
S_{base1}	10 kVA	M_i^*	8 s
S_{base2}	5 kVA	D_i^*	17 pu
$E_0 = V_{grid}$	200 V	$k_{p\,i}^*$	20 pu
$\omega_0 = \omega_{grid}$	376.99 rad/s	$k_{q\,i}^*$	5 pu
$P_{0\,i}^*$	1 pu	$T_{fq\,i}$	7.96×10^{-3} s
$Q_{0\,i}^*$	0 pu		
The Basic VSG control			
$K_{pq\,i}^*$	0.0025 pu	$T_{iq\,i}$	1.25×10^{-4} s
The Enhanced VSG control			
$K_{pq\,i}^*$	0.0125 pu	$T_{iq\,i}$	1.25×10^{-4} s

TABLE 4.3 Simulation Sequence

Time	Grid	$P^*_{0\_1}$	$P^*_{0\_2}$	Load
t < 21 s	Connected	1 pu	1 pu	Load1
21 s ≤ t < 24 s	Disconnected	–	–	–
24 s ≤ t < 27 s	–	–	–	Load1+2
27 s ≤ t < 30 s	–	–	0.6 pu	–

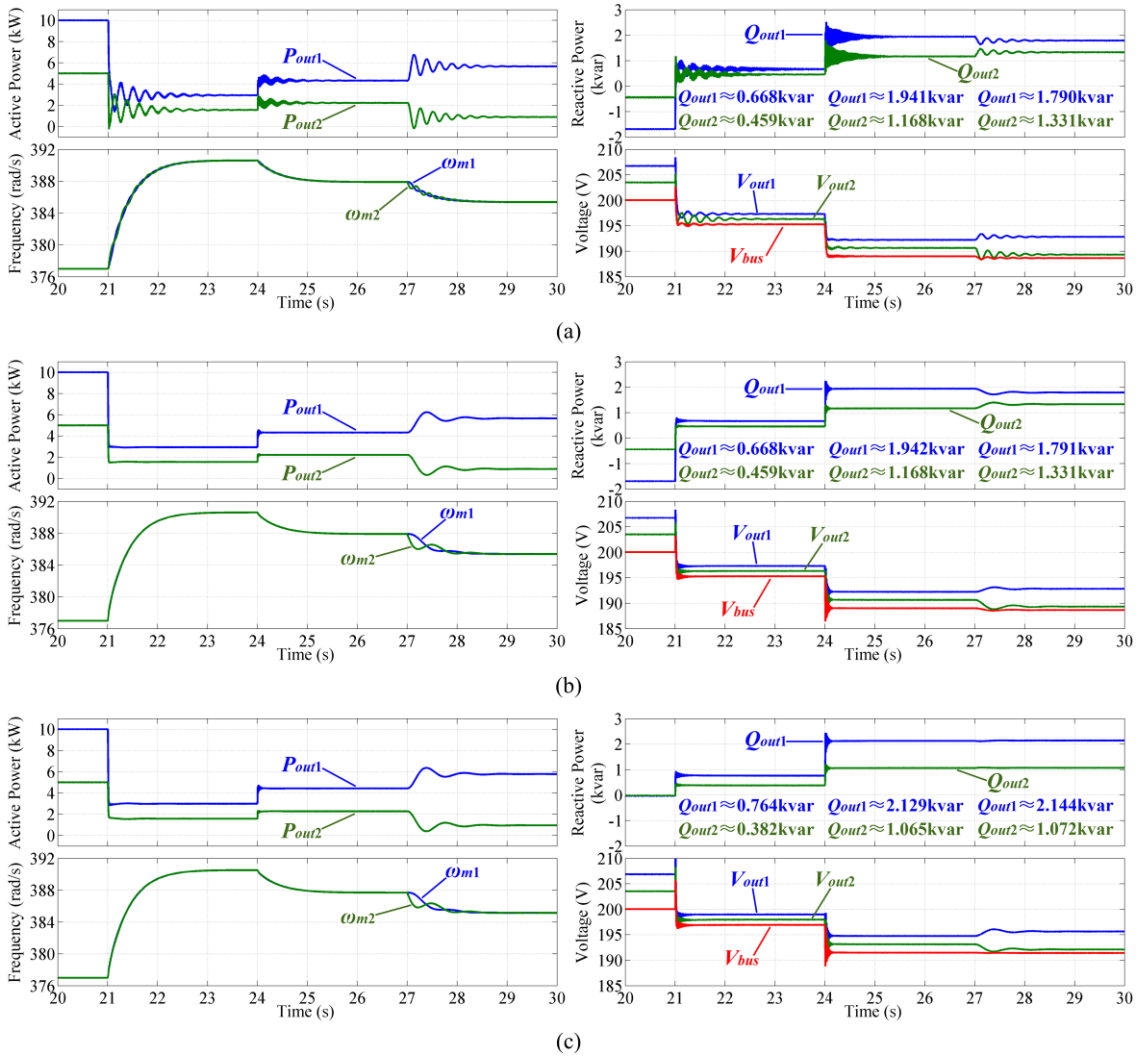

Fig. 4.12 Simulation results of active power and frequency in the left column and reactive power and voltage in the right column when both DGs are controlled by (a) the basic VSG control, (b) the basic VSG control + the proposed stator impedance adjuster, (c) the complete proposed enhanced VSG control.

posed enhanced VSG control scheme. A microgrid shown in Fig. 4.11 is studied. As it is shown in Fig. 4.11, impedances of output filters and distribution lines of each DG differ in per unit values. Other main parameters are listed in Table 4.2, and the sequence of simulation is shown in Table 4.3. Events of islanding from main grid, loading transition, and intentional active power sharing change are simulated at 21 s, 24 s, and 27 s, respectively. The simulation results are shown in Fig. 4.12.

As it is illustrated in Fig. 4.12(a), when the microgrid is islanded at 21 s, and when load 2 is connected at 24 s, oscillation can be observed in active power when the basic VSG control is applied for both DGs. This oscillation is almost eliminated by applying the proposed stator impedance adjuster in Figs. 4.12(b) and 4.12(c). As the disturbance at 27 s is caused by change of active power set value of DG1, which is not a loading transition, active power oscillation cannot be eliminated in this case. However, the proposed stator impedance adjuster increases the damping ratio; therefore, the overshoots in Figs. 4.12(b) and 4.12(c) are smaller than that in Fig. 4.12(a). Meanwhile, the oscillation periods become longer, because the damped natural frequencies are decreased as it is discussed in Section 4.2.2. Note that the rate of change of frequency remains the same in all cases, which suggests that the proposed enhanced VSG control has no influence on the inertia support feature of VSG control.

Moreover, in Figs. 4.12(a) and 4.12(b), reactive power is not shared properly in islanded mode, and is not controlled at set value in grid-connected mode, due to the voltage drop through the line impedance. Besides, reactive power control is not independent from active power control, as a change of set value of active power at 27 s also causes a change of reactive power sharing. These problems are all solved in the complete enhanced VSG control by applying the proposed bus voltage estimator, as shown in Fig. 4.12(c). It is also noteworthy that the steady-state deviations of DG voltage and bus voltage become smaller when the enhanced VSG control is applied.

Fig. 4.13 illustrates the dynamic performance of reactive power and voltage during the loading transition at 24 s. Although the virtual internal emf E_1 becomes much higher in the proposed enhanced VSG control owing to large voltage drop on the virtual stator inductance L_{ls}, the maximum voltage sag of PWM inverter reference V_{pwm1} and output voltage V_{out1} are kept within the same level as the basic VSG control. This implies that the voltage drop on L_{ls} is compensated well by the reactive power PI controller. Besides, although in the enhanced VSG control, the voltages become slightly oscillatory, the reactive power oscillations converge within 0.1 s.

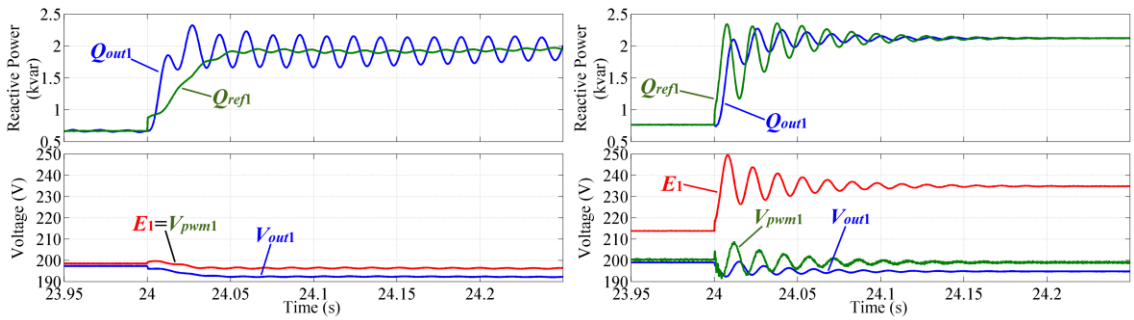

Fig. 4.13 Zoom-in simulation results of reactive power and voltage of DG1 at 24 s.
(a) The basic VSG control; (b) the proposed enhanced VSG control.

4.6 Experimental Results

Experiments are executed in an islanding microgrid, of which the circuit is the same as that of simulation shown in Fig. 4.11, except that instead of dc sources, ac supply rectified by diode bridge is used to imitate the dc output of DGs, and the breaker BK3 is opened, as shown in Fig. 4.14. The experiment setup is the same as those shown in Section 3.6. Experiment sequence is described in Table 4.4. Control Parameters are the same as those listed in Table 4.2, and the experimental results are shown in Fig. 4.15.

Experimental results verify again the effectiveness of the proposed enhanced VSG control. First, by comparing Figs. 4.15(b) and 4.15(c) with Fig. 4.15(a), it can be observed that with the proposed stator impedance adjuster, the oscillation due to loading transition at 0.5 s is eliminated, and the oscillation due to change of set value of acitive power at 3.0 s is damped. It implies that the VSG control with the proposed stator impedance adjuster is able to track the loading transition rapidly and accurately without oscillation; meanwhile, the inertia support of the basic VSG control is kept. Even when an oscillation occurs, the overshoot is suppressed owing to increased system damping.

Furthermore, by comparing Fig. 4.15(c) with Figs. 4.15(a) and 4.15(b), it can be concluded that by applying the proposed bus voltage estimator, the reactive power is shared according to the power rating ratio, and is immune to active power sharing change and line impedance mismatch in per unit values. Although ripples in RMS value of output voltage can be observed due to a slight load unbalance, the reactive power is controlled well when the enhanced VSG control is applied.

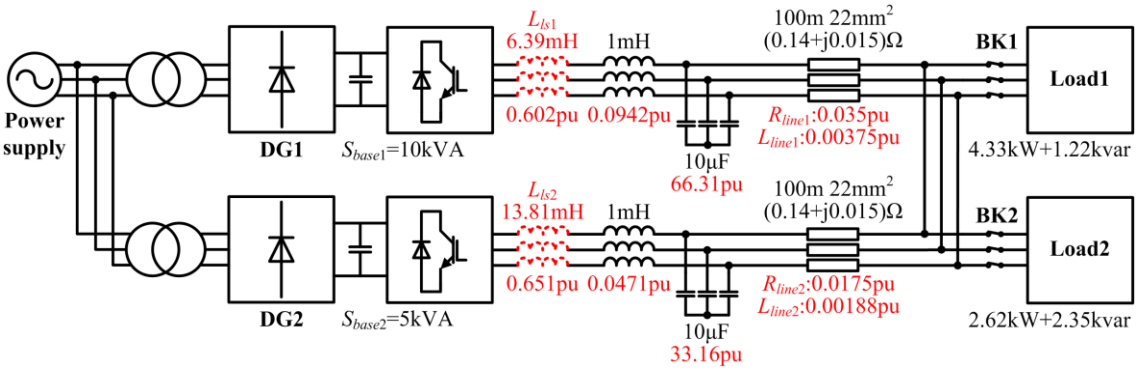

Fig. 4.14 Experiment circuit.

Table 4.4 Experiment Sequence

Time	$P^*_{0\_1}$	$P^*_{0\_2}$	Load
t < 0.5 s	1 pu	1 pu	Load1
0.5 s ≤ t < 3 s	–	–	Load1+2
3 s ≤ t < 5 s	–	0.6 pu	–

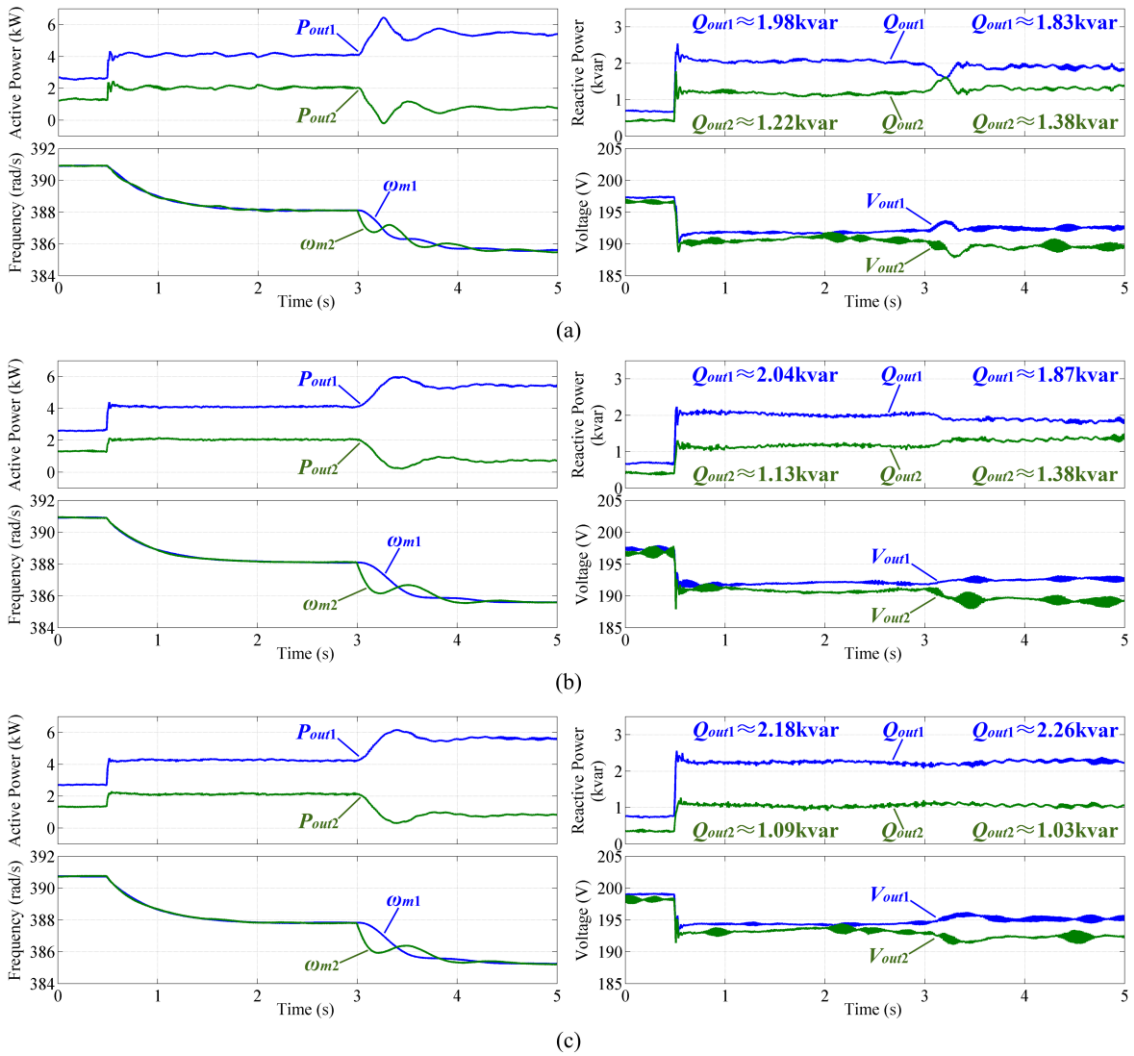

Fig. 4.15 Experimental results of active power and frequency in the left column and reactive power and voltage in the right column when both DGs are controlled by (a) the basic VSG control, (b) the basic VSG control + the proposed stator impedance adjuster, (c) the complete proposed enhanced VSG control.

4.7 Conclusion

In this chapter, an enhanced VSG control was proposed as a novel communication-less control method in a microgrid. A stator impedance adjuster was developed based on state-space analyses, in order to increase the active power damping and to properly share transient active power. A novel communication-less reactive power control strategy based on inversed voltage droop control ($V-Q$ droop control) and common ac bus voltage estimation was also proposed to achieve accurate reactive power sharing, which is immune to active power sharing change and line impedance mismatch. Simulation and experimental results demonstrated that the proposed enhanced VSG control achieves desirable transient and steady-state performances, and keeps the inertia support feature of VSG control. As a result, the proposed enhanced VSG control is a preferable choice for the control system of DGs in microgrids.

References

[1] J. Liu, Y. Miura, H. Bevrani, and T. Ise, "Enhanced virtual synchronous generator control for parallel inverters in microgrids," *IEEE Trans. Smart Grid*, doi: 10.1109/TSG.2016.2521405.

[2] T. Shintai, Y. Miura, and T. Ise, "Oscillation damping of a distributed generator using a virtual synchronous generator," *IEEE Trans. Power Del.*, vol. 29, no. 2, pp. 668–676, Apr. 2014.

[3] J. Alipoor, Y. Miura, and T. Ise, "Power system stabilization using virtual synchronous generator with alternating moment of inertia," *IEEE J. Emerg. Sel. Topics Power Electron.*, vol. 3, no. 2, pp. 451–458, Jun. 2015.

[4] C. Cheng, Z. Zeng, H. Yang, and R. Zhao, "Wireless parallel control of three-phase inverters based on virtual synchronous generator theory," in *Proc. Int. Conf. Elect. Mach. Syst. (ICEMS)*, 2013, pp. 162–166.

[5] K. Sakimoto, Y. Miura, and T. Ise, "Characteristics of parallel operation of inverter-type distributed generators operated by a virtual synchronous generator," *IEEJ Trans. Power and Energy*, vol. 133, no. 2, pp. 186–194, Feb. 2013 (in Japanese). or *Electrical Engineering in Japan*, vol. 192, no. 4, pp. 9–19, Sep. 2015 (in English).

[6] A. D. Paquette, M. J. Reno, R. G Harley, and D. M. Divan, "Sharing transient loads: causes of unequal transient load sharing in islanded microgrid operation," *IEEE Ind. Appl. Mag.*, vol. 20, no. 2, pp. 23–34, Mar./Apr. 2014.

[7] J. He, Y. W. Li, J. M. Guerrero, F. Blaabjerg, and J. C. Vasquez, "An islanding microgrid power sharing approach using enhanced virtual impedance control scheme," *IEEE Trans. Power Electron.*, vol. 28, no. 11, pp. 5272–5282, Nov. 2013.

[8] Y. Zhu, Z. Fang, F. Wang, B. Liu, and Y. Zhao, "A wireless load sharing strategy for islanded microgrid based on feeder current sensing," *IEEE Trans. Power Electron.*, vol. 30, no. 12, pp.6706–6719, Dec. 2015.

[9] Y. W. Li and C.-N. Kao, "An accurate power control strategy for power-electronics-interfaced distributed generation units operating in a low-voltage multibus microgrid," *IEEE Trans. Power Electron.*, vol. 24, no. 12, pp. 2977–2988, Dec. 2009.

[10] C-.T. Lee, C-.C. Chu, and P-.T. Cheng, "A new droop control method for the autonomous operation of distributed energy resource interface converters," *IEEE Trans. Power Electron.*, vol. 28, no. 4, pp. 1980–1993, Apr. 2013.

[11] E. Rokrok and M. E. H. Golshan, "Adaptive voltage droop scheme for voltage source converters in an islanded multibus microgrid," *IET Gener. Transm. Distrib.*, vol. 4, no. 5, pp. 562–578, May 2010.

[12] H. Xu, X. Zhang, F. Liu, R. Shi, C. Yu, W. Zhao, Y. Yu, and W. Cao, "A reactive power sharing method based on virtual capacitor in islanding microgrid," in *Proc. Int. Power Electron. Conf. (IPEC-Hiroshima ECCE-Asia)*, 2014, pp. 567–572.

[13] J. He and Y. W. Li, "An enhanced microgrid load demand sharing strategy," *IEEE Trans. Power Electron.*, vol. 27, no. 9, pp. 3984–3995, Sept. 2012.

[14] J. He, Y. W. Li, and F. Blaabjerg, "An enhanced islanding microgrid reactive power, imbalance power, and harmonic power sharing scheme," *IEEE Trans. Power Electron.*, vol. 30, no. 6, pp. 3389–3401, Jun. 2015.

[15] H. Mahmood, D. Michaelson, and J. Jiang, "Accurate reactive power sharing in an islanded microgrid using adaptive virtual impedances," *IEEE Trans. Power Electron.*, vol. 30, no. 3, pp. 1605–1617, Mar. 2015.

[16] H. Han, Y. Liu, Y. Sun, M. Su, and J. M. Guerrero, "An improved droop control strategy for reactive power sharing in islanded microgrid," *IEEE Trans. Power Electron.*, vol. 30, no. 6, pp. 3133–3141, Jun. 2015.

[17] Q. Shafiee, J. M. Guerrero, and J. C. Vasquez, "Distributed secondary control for islanded microgrids — a novel approach," *IEEE Trans. Power Electron.*, vol. 29, no. 2, pp. 1018–1031, Feb. 2014.

[18] A. Micallef, M. Apap, C. Spiteri-Staines, J. M. Guerrero, and J. C. Vasquez, "Reactive power sharing and voltage harmonic distortion compensation of droop controlled single phase islanded microgrids," *IEEE Trans. Smart Grid*, vol. 5, no. 3, pp. 1149–1158, May 2014.

[19] Y. Zhang and H. Ma, "Theoretical and experimental investigation of networked control for parallel operation of inverters," *IEEE Trans. Ind. Electron.*, vol. 59, no. 4, pp. 1961–1970, Apr. 2012.

[20] T. Shintai, Y. Miura, and T. Ise, "Reactive power control for load sharing with virtual synchronous generator control," in *Proc. 7th Int. Power Electron. Motion Control Conf.*, 2012, pp. 846–853.

[21] Q.-C. Zhong, "Robust droop controller for accurate proportional load sharing among inverters operated in parallel," *IEEE Trans. Ind. Electron.*, vol. 60, no. 4, pp. 1281–1290, Apr. 2013.

[22] C. K. Sao and P. W. Lehn, "Autonomous load sharing of voltage source converters," *IEEE Trans. Power Del.*, vol. 20, no. 2, pp. 1009–1016, Apr. 2005.

[23] Q.-C. Zhong, P.-L. Nguyen, Z. Ma, and W. Sheng, "Self-synchronized synchronverters: inverters without a dedicated synchronization unit," *IEEE Trans. Power Electron.*, vol. 29, no. 2, pp. 617–630, Feb. 2014.

[24] H. Bevrani, S. Shokoohi, "An intelligent droop control for simultaneous voltage and frequency regulation in islanded microgrids," *IEEE Trans. Smart Grid*, vol. 4, no. 3, pp. 1505-1513, Sept. 2013.

[25] J. Rocabert, A. Luna, F. Blaabjerg, and P. Rodríguez, "Control of power converters in AC microgrids," *IEEE Trans. Power Electron.*, vol. 27, no. 11, pp. 4734–4749, Nov. 2012.

[26] L. Asiminoaei, R. Teodorescu, F. Blaabjerg, and U. Borup, "A digital controlled PV-inverter with grid impedance estimation for ENS detection," *IEEE Trans. Power Electron.*, vol. 20, no. 6, pp. 1480–1490, Nov. 2005.

Chapter 5

A VSG Paralleled with a Synchronous Generator in Microgrids

5.1 Introduction

In a remote microgrid where the main grid is not available, a dispatchable small synchronous generator (SG) using a diesel engine or a gas engine is usually used as the main power supply. Meanwhile, to save the fuel consumption, an inverter-interfaced DG using RES, e.g. photovoltaic, can be used as the secondary supply. Therefore, the control method of the inverter-interfaced DG for parallel operation with a SG should be established.

However, the dynamic performances of a small SG are usually poor due to relatively smaller moment of inertia and slow governor response. As a result, large rotor speed deviation during loading transition can be observed even for single SG operation. A method using back-to-back converter and electric double-layer capacitor (EDLC) is proposed to address this issue [1]; however, additional back-to-back converter is needed for SG. Another issue for a small SG is the operation under three-phase unbalanced loading condition. As three-phase unbalanced current will heat the SG and give rise to torsional stresses, the negative sequence current from the SG should be prevented. Parallel operation of a SG and an inverter-interfaced DG is studied in [2], [3]. However, a motor-generator set is used in these works, in which the response of governor is faster than that in a diesel or gas engine. Moreover, operation under unbalanced loading condition is not discussed in these works.

As it is demonstrated in Chapter 3, VSG control is able to improve the transient performance of rotor speed of the SG paralleled with it. Therefore, in this chapter, a modified VSG control scheme is proposed for the parallel operation of a SG and an inverter-interfaced DG. It is shown that the transient rotor speed deviation of a small SG is improved by the parallel operation of a VSG-control-based inverter. Moreover, a modification of VSG control based on double decoupled synchronous reference frame (DDSRF) is proposed, in order to deal with the unbalanced loading condition and to compensate the negative-sequence current of the SG. Although a VSG control method using DDSRF is proposed in [4] for the normal operation of a single-phase inverter, the idea to use it for unbalanced three-phase operation is a new challenge. Transient virtual stator impedance proposed in [3] is also introduced in the control scheme to limit the overcurrent during a large loading transition. Tuning methods of major control parameters are discussed based on eigenvalue analyses and simulation results executed in PSCAD/EMTDC, and the overall performance of the proposed modified VSG control is verified by simulation results, which demonstrate that the issues of

SG rotor speed deviation, unbalanced SG current, and overcurrent limiting are properly addressed with the proposed control method.

5.2 System Description

An islanded microgrid composed of a SG and an inverter-based DG is shown in Fig. 5.1. An LC filter is installed at the output terminal of the inverter to filter the higher order harmonic, and an additional reactor L_{ad_sg} is installed at the output terminal of the SG, whose function is discussed in Section 5.4.3. In the present application, it is assumed that the generators and the ac bus are installed in the same power plant. As a result, the short distribution lines (10 m with cross-section area of 8 mm^2) between the generators and the ac bus are negligible. Three-phase and single-phase loads representing the residential consumptions are installed at a distance, and are connected to the ac bus through a distribution line of 100 m with a cross-section area of 22 mm^2.

A round-rotor SG with a primary mover of gas engine is discussed in the present work, of which the main parameters are listed in Table 5.1. The control system of the SG is shown in Fig. 5.2, which is composed of a governor to adjust the shaft power and an automatic voltage regulator (AVR) to regulate the exciting voltage. Droop coefficients $k^*_{p\_sg}$ and $k^*_{q\_sg}$, and set value of active and reactive power $P^*_{0\_sg}$ and $Q^*_{0\_sg}$ are designed equally to those of DG, in order to share the active and

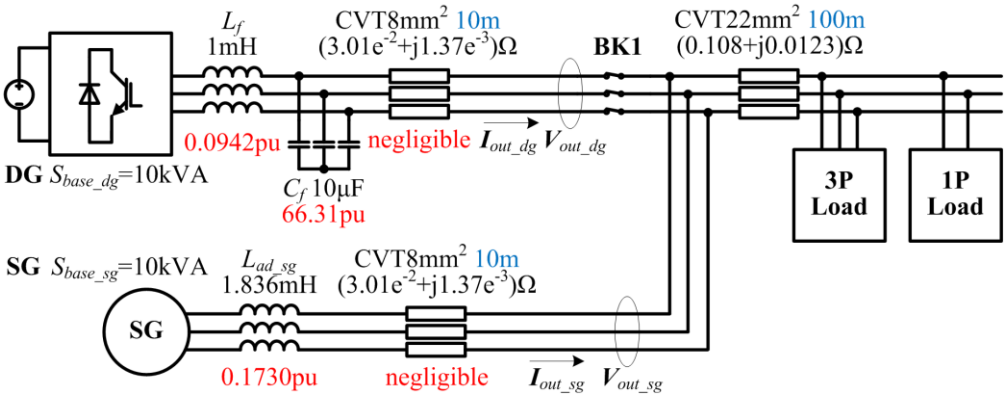

Fig. 5.1 An islanded microgrid composed of a SG and an inverter-interfaced DG.

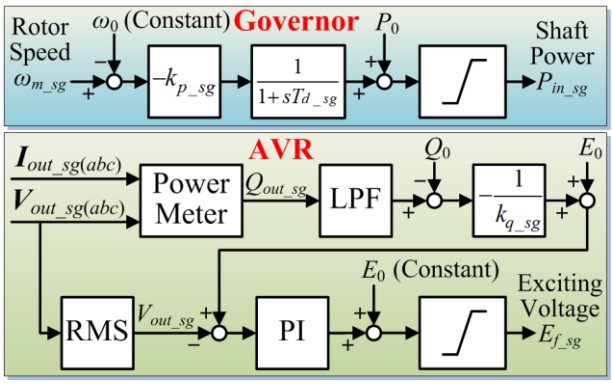

Fig. 5.2 Control system of the SG.

Table 5.1 SG Parameters

Parameter	Value	Parameter	Value
Rated voltage E_0	200 V	Set value of active power $P^*_{0\_sg}$	1 pu
Rated power S_{base_sg}	10 kVA	Set value of reactive power $Q^*_{0\_sg}$	0 pu
Nominal frequency ω_0	376.99 rad/s	$\omega - P$ droop coefficient $k^*_{p\_sg}$	20 pu
Inertia constant M^*_{sg}	0.16 s	$V - Q$ droop coefficient $k^*_{p\_sg}$	5 pu
AVR PI K^*_{pAVR}	20 pu	Governor time constant T_{d_sg}	1 s
AVR PI T_{iAVR}	0.025 s	AVR LPF cut-off frequency	20 Hz
Impedance Model			
$X^*_d = X^*_q$	0.219 pu	$X'^*_d = X'^*_q$	0.027 pu	$X''^*_d = X''^*_q$	0.01 pu
T'_{do}	6.55 s	T''_{do}	0.039 s	T'_{qo}	0.85 s	T''_{qo}	0.071 s

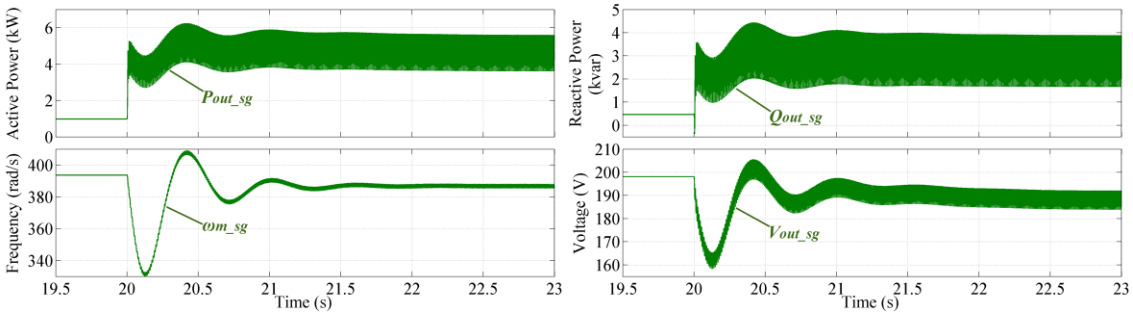

Fig. 5.3 Simulation results of single SG operation

with active power and frequency in the left column and reactive power and voltage in the right column.

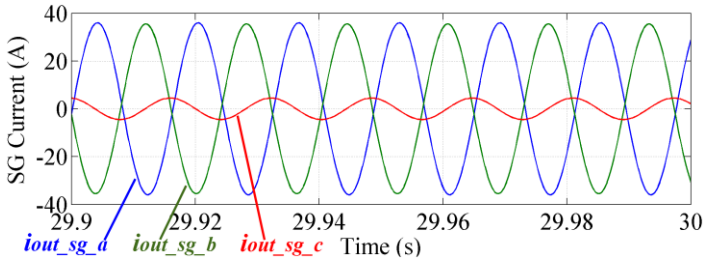

Fig. 5.4 Simulation results of steady-state SG current waveforms in single SG operation.

reactive power according to generator power rating ratio, as it is discussed in Section 2.3.2. Here, subscript "*sg*" indicates parameters related to SG. A first-order lag unit with time constant T_{d_sg} is presented in the governor to indicate the response delay of the mechanical system of the governor. As it is shown in Table 5.1, the inertia constant M^*_{sg} is very small (0.16 s) compared with large power rating SG of MVAs (usually several seconds), and the governor response is very slow in view of the fact that T_{d_sg} is 1 s. This implies that during a loading transition, the shaft power cannot be adjusted immediately to catch up the load power, and the kinetic energy stored in the rotating mass of the SG is not sufficient to compensate the transient power shortage/surplus. As a result, a large

deviation of rotor speed can be observed, as shown in the simulation results of a single SG operation (Fig. 5.3). In order to be compared with DG frequency in the following discussion, SG rotor speed ω_{m_sg} shown in simulation results is multiplied by the number of pairs of poles.

In Fig. 5.3, SG is initially operated with a three-phase load of 1 kW, 0.5 kvar. At 20 s, a single-phase load of 4.8 kW, 2.1 kvar is connected, which leads to a large rotor speed drop down to around 330 rad/s. Besides, large ripples can be observed in the steady-state output voltage, rotor frequency, and active and reactive power of SG due to the three-phase unbalance introduced by the single-phase load. This is verified by the steady-state three-phase output current waveforms of the SG shown in Fig. 5.4, in which a large three-phase unbalance can be observed.

5.3 The Proposed Modified VSG Control Scheme

The control scheme of the proposed modified VSG control is shown in Fig. 5.5. As shown in the figure, the measured three-phase DG and SG output voltage and current are firstly transformed into αβ frame, and then decomposed into positive and negative sequence dq frame using the algorithm shown in Fig. 5.6 [4]. For simplification, the $\boldsymbol{V}_{\alpha\beta}$ in Fig. 5.6 stands for both $\boldsymbol{V}_{out\_sg(\alpha\beta)}$ and $\boldsymbol{V}_{out\_dg(\alpha\beta)}$ and so does $\boldsymbol{I}_{\alpha\beta}$, as this algorithm is applied for both SG and DG output voltage and current. Here, subscript "*dg*" indicates parameters related to DG. The transformation matrices $\boldsymbol{T}^{\pm} = \boldsymbol{T}(\pm\theta_g)$ and $\boldsymbol{T}^{\pm\mathbf{2}} = \boldsymbol{T}(\pm 2\theta_g)$ are defined as (5.1), and the low pass filter is a first-order filter with a cut-off frequency at 40 Hz.

$$\boldsymbol{T}(\theta_g) = \begin{bmatrix} \cos\theta_g & \sin\theta_g \\ -\sin\theta_g & \cos\theta_g \end{bmatrix} \tag{5.1}$$

The DG output active and reactive power P_{out_dg} and Q_{out_dg} and line-to-line RMS value of

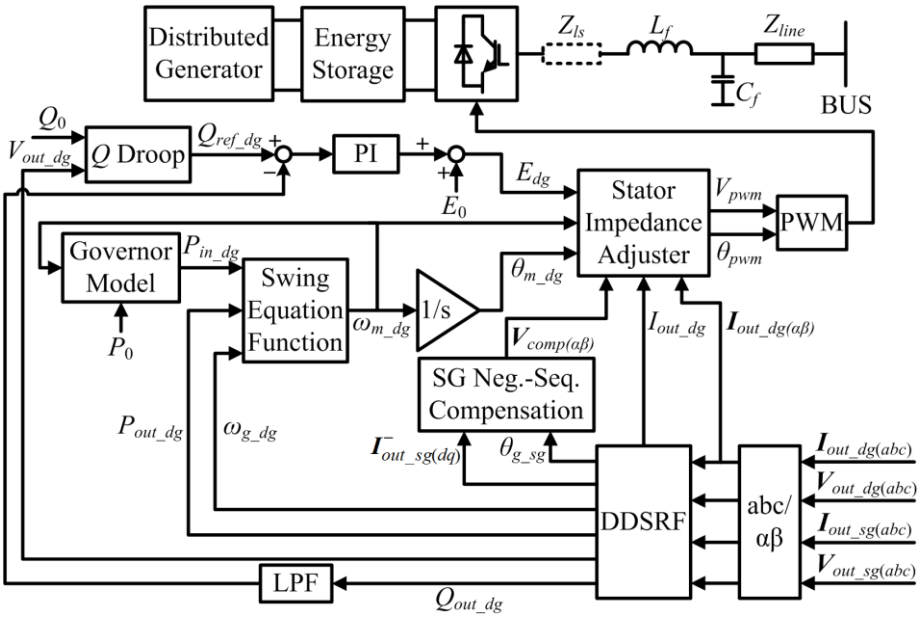

Fig. 5.5 Block diagram of the proposed modified VSG control.

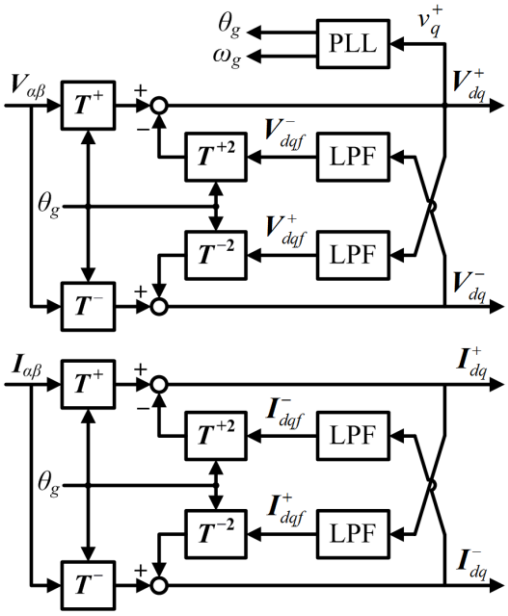

Fig. 5.6 DDSRF algorithm [4].

output voltage and current V_{out_dg} and I_{out_dg} used for the rest part of control are calculated based on only the positive-sequence components, as shown in (5.2)–(5.5). If αβ-frame or three-phase components are used directly for these calculations, i.e. using (4.21), (4.22) for the calculations of the output active and reactive power and using (2.8) for the calculation of the line-to-line RMS value of output voltage, negative-sequence components will be included in these calculated variables during unbalanced loading condition. These negative-sequence components will present as large ripples with oscillation frequency at twice synchronous frequency, thus will consequently result in oscillations in output voltage and frequency through the control algorithm in the swing equation function and the *Q* Droop and *Q* PI controller. Therefore, calculations based on only the positive-sequence components shown in (5.2)–(5.5) are quite important for the present application.

$$P_{out\_dg} = v^{+}_{out\_dg\_d} i^{+}_{out\_dg\_d} + v^{+}_{out\_dg\_q} i^{+}_{out\_dg\_q} \tag{5.2}$$

$$Q_{out\_dg} = -v^{+}_{out\_dg\_d} i^{+}_{out\_dg\_q} + v^{+}_{out\_dg\_q} i^{+}_{out\_dg\_d} \tag{5.3}$$

$$V_{out\_dg} = \sqrt{(v^{+}_{out\_dg\_d})^2 + (v^{+}_{out\_dg\_q})^2} \tag{5.4}$$

$$I_{out\_dg} = \sqrt{(i^{+}_{out\_dg\_d})^2 + (i^{+}_{out\_dg\_q})^2} \tag{5.5}$$

The SG negative-sequence current compensator is shown in Fig. 5.7. Conventional PI control is used to eliminate the SG negative-sequence current. The output $\boldsymbol{V}_{comp(\alpha\beta)}$ is a counter-rotating voltage vector, which is added to the forward-rotating output voltage reference for the PWM inverter in Fig. 5.8.

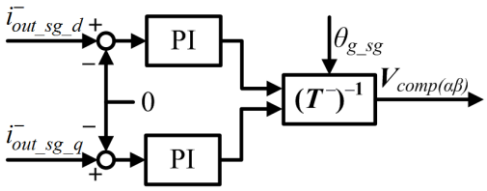

Fig. 5.7 Block diagram of the "SG Neg.-Seq. Compensation" block of the modified VSG control.

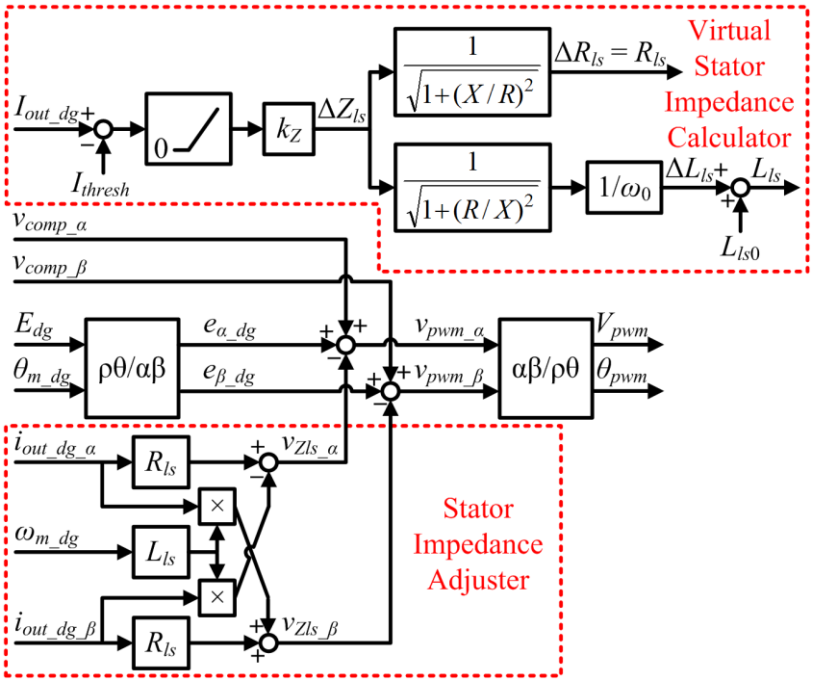

Fig. 5.8 Block diagram of the "Stator Impedance Adjuster" block of the modified VSG control.

The stator impedance adjuster shown in Fig. 5.8 is used to set the total output impedance to a desired value. The virtual stator impedance is composed of two parts, the constant virtual stator inductance L_{ls0} and the transient virtual stator impedance $\Delta Z_{ls} = \Delta R_{ls} + \omega_0 \Delta L_{ls}$. The constant virtual stator inductance L_{ls0} follows the same principle as that of the virtual stator inductance L_{ls} discussed in Section 4.4, and its tuning method is discussed in Section 5.4.3. The transient virtual stator impedance ΔZ_{ls} is proposed in [3] to limit the DG overcurrent during a large loading transition. The transient virtual impedance only functions when the line-to-line RMS value of output current I_{out_dg} exceeds the predefined threshold value I_{thresh}. As I_{thresh} is normally set to 1 pu, this implies an overcurrent condition. The transient virtual impedance is designed proportionally to the amount of overcurrent. Tuning methods of the proportional gain k_Z and the reactance/resistance ratio X/R are discussed in Section 5.4.4.

It is noteworthy that the bus voltage estimator proposed in Section 4.4 is omitted in the proposed modified VSG control, as the output voltages of the DG and the SG are measured in the proximity of

the common ac bus, as shown in Fig. 5.1. Therefore, based on the discussion in Section 4.3, accurate steady-state reactive power sharing is guaranteed even without common ac bus voltage estimation.

5.4 Discussions on Tuning Methods of Parameters

The control parameters used in the proposed modified VSG control are listed in Table 5.2. As mentioned previously, droop coefficients $k_{p\_dg}^*$ and $k_{q\_dg}^*$, and the set values of active and reactive power $P_{0\_dg}^*$ and $Q_{0\_dg}^*$ are designed equally to those of SG for active and reactive sharing. Tuning methods of other main parameters are discussed in the following part of this section. Unless otherwise specified, the eigenvalue analyses and simulations shown in this chapter are based on the system shown in Fig. 5.1, and parameters are listed in Tables 5.1 and 5.2. It is noteworthy that the transient virtual stator impedance ΔZ_{ls} is set to 0 in the eigenvalue analyses and simulations presented in Sections 5.4.2 and 5.4.3.

5.4.1 Swing Equation Parameters

As it is analyzed in Section 4.2.3, to share the transient active power properly, the swing equation parameters of VSG should be set to the same per unit value as those of SG. That is to say, M_{dg}^* should be set to 0.16 s. As for damping factor, from (2.3), the average damping factor of a SG can be calculated through (5.6).

$$D_{av\_sg} \approx \frac{E_0^2}{2}\left[\frac{T''_d X'_d (X'_d - X''_d)}{X''_d \left(X'_d + X_{ad\_sg}\right)^2} + \frac{T''_q X'_q \left(X'_q - X''_q\right)}{X''_q \left(X'_q + X_{ad\_sg}\right)^2}\right] \tag{5.6}$$

From parameters listed in Table 5.1 and Fig. 5.1, $D_{av\_sg}^*$ is 8.7 pu. Therefore, D_{dg}^* should be set to 8.7 pu.

Table 5.2 DG Control Parameters

Parameter	Value	Parameter	Value
E_0	200 V	$P_{0\_dg}^*$	1 pu
S_{base_dg}	10 kVA	$Q_{0\_dg}^*$	0 pu
ω_0	376.99 rad/s	$k_{p\_dg}^*$	20 pu
M_{dg}^*	0.16 s	$k_{q\_dg}^*$	5 pu
D_{dg}^*	8.7 pu	T_{d_dg}	0 s
L_{ls0}	1.122 mH	k_Z^*	0.69 pu
L_{ad_sg}	1.836 mH	X/R	5
PI Controller for Reactive Power			
K_{pq}^*	0.05 pu	T_{iq}	1.25×10^{-2} s
PI Controller for SG Neg.-Seq. Compensation			
$K_{p\_neg}^*$	0.1 pu	T_{i_neg}	0.01 s
Cut-off frequency of LPF for Q_{out_dg}			20 Hz

5.4.2 Governor Delay

As it is discussed in Chapter 3, the governor delay T_{d_dg} reduces the total inertia of microgrids and amplifies oscillations. As a result, it is removed in Chapter 4. In [2], it is suggested to set T_{d_dg} to the same value as T_{d_sg}, i.e. 1 s, in order to share the transient active power properly. However, based on the steady-state model presented in Section 3.4, if T_{d_dg} is set to 1 s, a very oscillatory pair of conjugated eigenvalues could be observed near the origin, with a damping ratio ζ less than

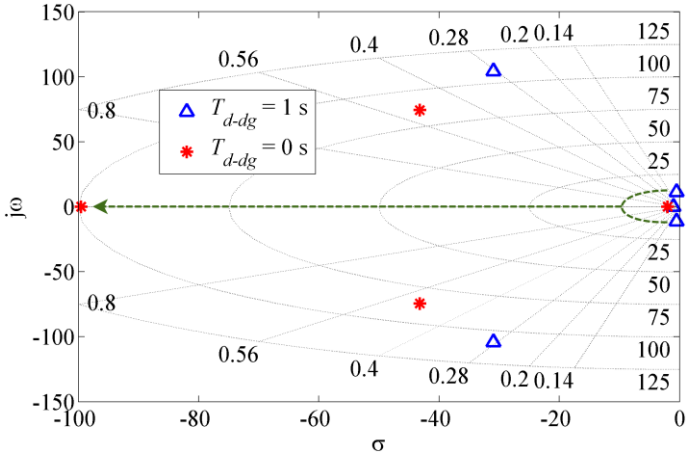

Fig. 5.9 Eigenvalue loci with a variation of T_{d_dg}.

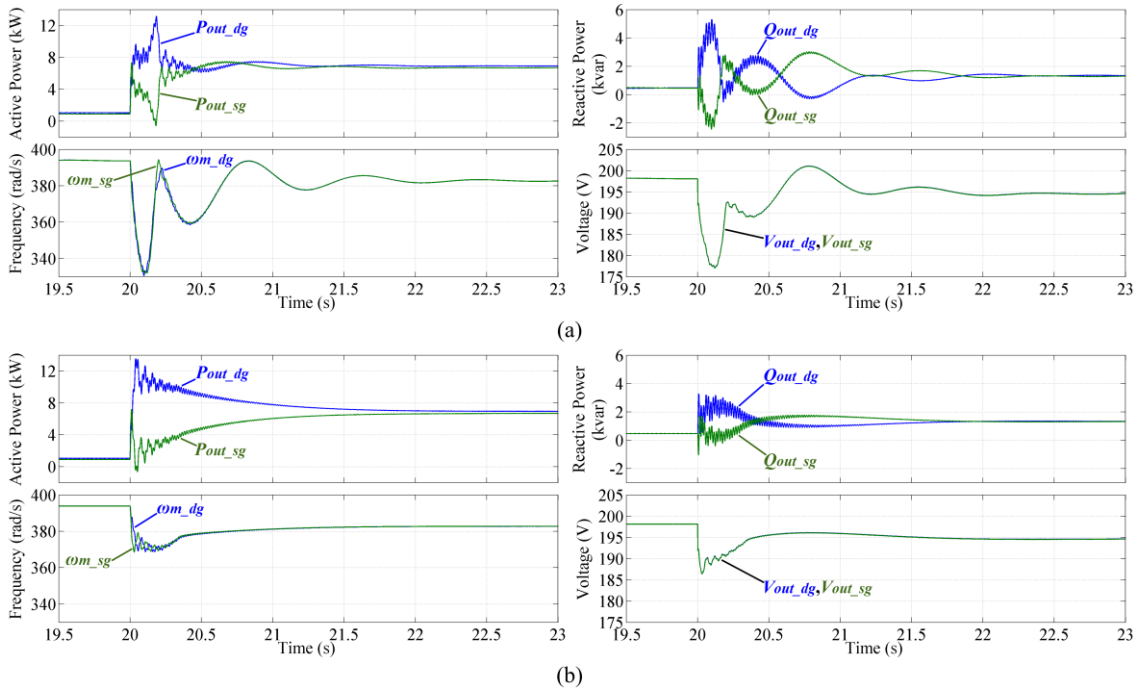

Fig. 5.10 Simulation results for the governor delay design
with active power and frequency in the left column and reactive power and voltage in the right column when (a) $T_{d\_dg} = 1$ s, (b) $T_{d\_dg} = 0$ s.

0.14, as depicted in Fig. 5.9. These oscillatory eigenvalues indicate large oscillations in output variables shown in (3.36), including the output active power and the frequency of both the DG and the SG. These eigenvalues become a fast non-conjugated eigenvalue if T_{d_dg} is set to 0 s. To verify this point, simulation results with both $T_{d\_dg} = 1$ s and $T_{d\_dg} = 0$ s during a three-phase loading transient from 2 kW, 1 kvar to 15 kW, 3 kvar are shown in Figs. 5.10(a) and 5.10(b), respectively. It is clear that in the case of $T_{d\_dg} = 1$ s, large oscillations with a period around 1 s can be observed in all presented parameters, which coincide with the oscillatory eigenvalues near the origin shown in Fig. 5.9. These oscillations result in much larger frequency and voltage deviations and poorer active and reactive power transient performances than the case of $T_{d\_dg} = 0$ s. Therefore, the governor delay T_{d_dg} is set to 0 s in the present work.

5.4.3 Constant Virtual Stator Reactance

From the principle of a round-rotor SG, the synchronizing power coefficient of the SG shown in Fig. 5.1 can be calculated through (5.7) [5].

$$K_{sg} \approx \frac{E'_q V_{bus}}{X'_d + X_{ad\_sg}} \cos \delta'_{sg}, \tag{5.7}$$

where δ'_{sg} is the transient power angle of SG.

As it is discussed in Section 4.2.3, the per unit value of synchronizing power coefficient of the DG and the SG should be designed equally to provide a proper immediate active power sharing after a loading transition. Defining $X_{sg} = X'_d + X_{ad\_sg}$ and supposing $E'_q \approx E_{dg}$, $\cos \delta'_{sg} \approx \cos \delta_{dg}$, by comparing (3.9) with (5.7), the key is to guarantee $X^*_{sg} = X^*_{dg}$. Knowing that $X_{dg} = X_f + X_{ls0}$, and X'_d of the SG and X_f of the DG are fixed, $X^*_{sg} = X^*_{dg}$ can be guaranteed by tuning X_{ls0} and X_{ad_sg}.

It should be pointed out that a small value of X leads to an unstable system, as demonstrated in Fig. 5.11 (a) by eigenvalue analyses based on the steady-state model presented in Section 3.4. As X^*

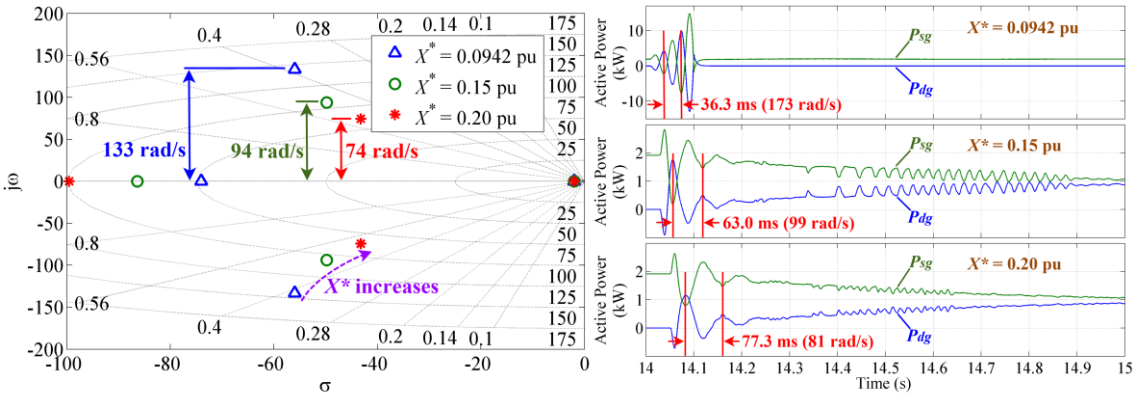

(a) (b)

Fig. 5.11 Analysis of different values of total output reactance.

(a) Loci of eigenvalue. (b) Simulation results.

gets small, the damped natural frequency of a pair of conjugated eigenvalues moves towards the synchronous frequency, which implies a probable resonance near synchronous frequency. The simulation results of the synchronization process shown in Fig. 5.11 (b) verify this point. In these simulations, the SG operates with a three-phase load of 2 kW, 1 kvar and the DG is connected at around 14 s. In the case where $X_{ls0} = 0$ and X_{ad_sg} is tuned to make $X_{sg}^* = X_{dg}^* = 0.0942$ pu, a divergent oscillation occurs after the connection of the DG. The system becomes unstable, and the DG is finally tripped due to overcurrent. This issue can be solved by increasing X^* up to 0.15 pu, and the performance is even better in the case of 0.20 pu, as it is shown in Fig. 5.11 (b). This is because the damped natural frequency of the conjugated eigenvalues becomes smaller thus difficult to be excited by the disturbances at synchronous frequency. It is noteworthy that the oscillation frequencies in the simulation results coincide with the damped natural frequencies in eigenvalue analyses.

As a result, $X_{sg}^* = X_{dg}^* = 0.20$ pu is suggested for the present application. For the DG, the constant virtual stator inductance L_{ls0} is set to 1.122 mH ($X_{ls0}^* = 0.1057$ pu), and for the SG, an additional inductor L_{ad_sg} of 1.836 mH ($X_{ad\_sg}^* = 0.1730$ pu) is added to the output of the SG as shown in Fig. 5.1.

5.4.4 Transient Virtual Stator Impedance for Current Limiting

The voltage drop through the transient virtual stator impedance should equal the nominal voltage during a three-phase fault, as given by (5.8) [3].

$$E_0^* = I_{max}^* \Delta Z_{ls}^*, \tag{5.8}$$

where I_{max}^* is the desired maximum RMS value of phase current in per unit value.

From Fig. 5.8 and (5.8), the proportional gain k_Z can be calculated through (5.9).

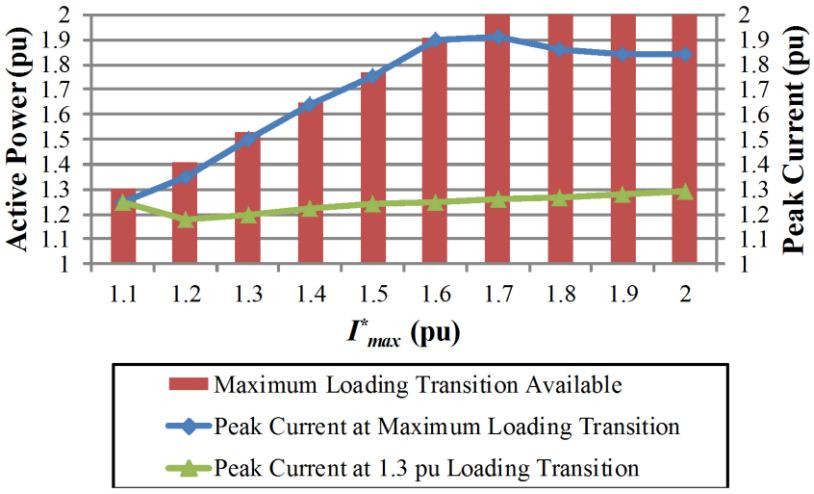

Fig. 5.12 Simulation results for tuning the proportional gain k_Z of transient virtual stator impedance.

$$k_Z^* = \frac{\Delta Z_{ls}^*}{(I_{max}^* - I_{thresh}^*)} = \frac{E_0^*}{I_{max}^*(I_{max}^* - I_{thresh}^*)} \tag{5.9}$$

As I_{thresh}^* is set to 1 pu and $E_0^* = 1$ pu, based on (5.9), k_Z^* can be determined by a given I_{max}^*.

To choose an appropriate value for I_{max}^*, a series of simulations are executed and the results are shown in Fig. 5.12. In these simulations, loading transitions from 0 pu to a specified active power loading are executed during the parallel operation of SG and DG. As the sum of power ratings of DG and SG is 2 pu (20 kW), loading transitions up to 2 pu are tested.

As it is illustrated in Fig. 5.12, if I_{max}^* is chosen less than 1.7 pu, the microgrid gets unstable during a 2 pu active power loading transition. For $I_{max}^* \geq 1.7$ pu, larger value of I_{max}^* leads to smaller peak current during a 2 pu active power loading transition, but larger peak current during a 1.3 pu active power loading transition. A compromise can be reached when $I_{max}^* = 1.8$ pu; there-

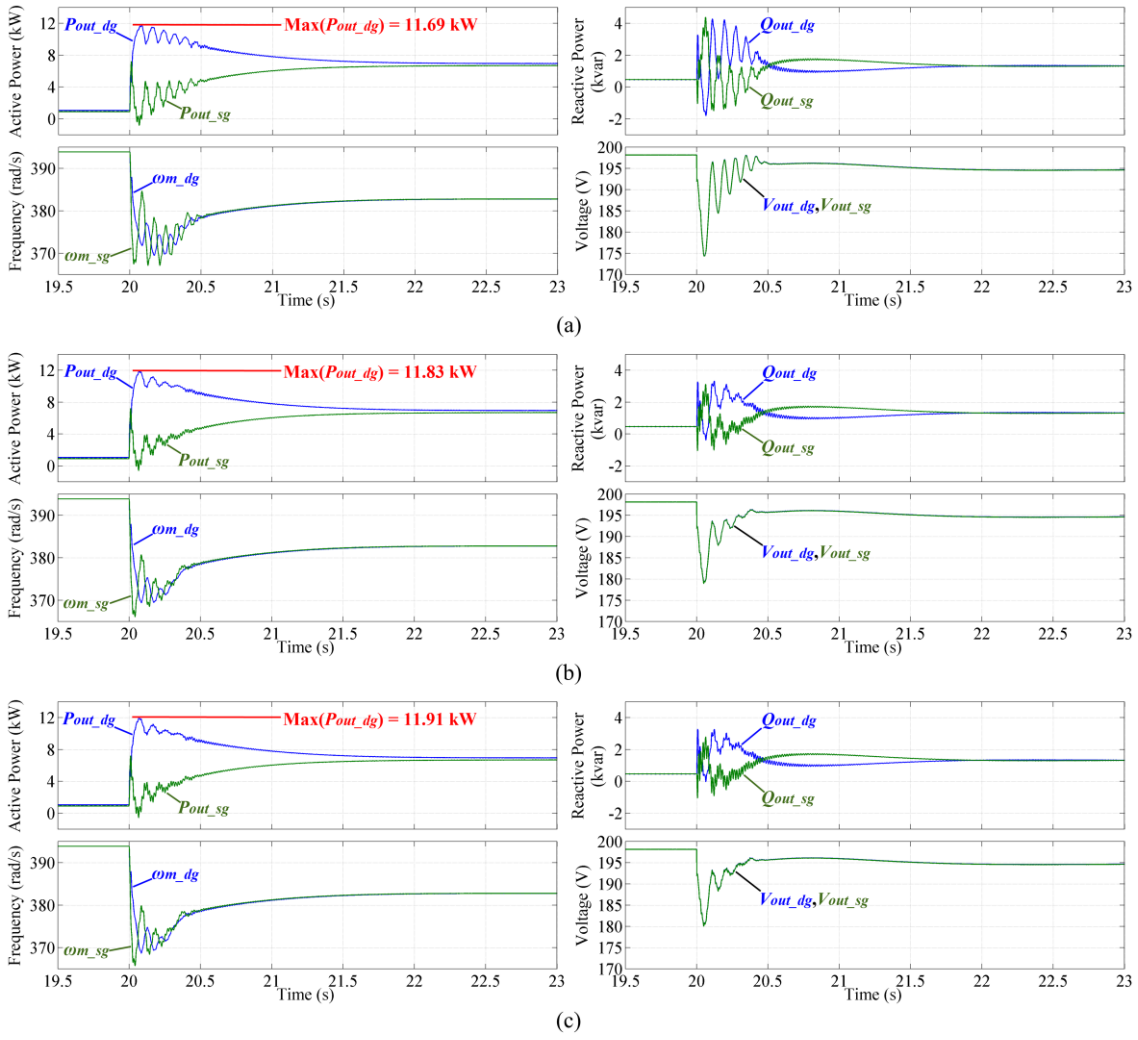

Fig. 5.13 Simulation results for tuning the X/R ratio of transient virtual stator impedance with active power and frequency in the left column and reactive power and voltage in the right column when (a) $X/R = 1$, (b) $X/R = 5$, (c) $X/R = 20$.

fore, according to (5.9), k_Z^* is set to 0.69 pu for the present application.

Another issue is the design of X/R ratio for the transient virtual stator impedance. A series of simulations are executed during a three-phase loading transition from 2 kW, 1 kvar to 15 kW, 3 kvar, with $k_Z^* = 0.69$ pu in all cases and X/R is set to 1, 5 and 20. The simulation results are shown in Fig. 5.13. It can be observed that the peak value of DG output active power is limited better with more resistive transient virtual stator impedance owing to the damping feature of resistance. However, resistive transient virtual stator impedance may deteriorate the transient reactive power and lead to larger voltage deviation, as it is illustrated in the right column of Fig. 5.13. Therefore, a trade-off should be made between the active power limiting and the transient performances of reactive power and voltage. In the present work, X/R is set to 5 to achieve a balanced overall performance.

5.5 Simulation Results

5.5.1 Unbalanced Loading Condition

Comparative simulations are executed in PSCAD/EMTDC environment, in order to verify the proposed modification on the VSG control. The results of first simulation group are shown in Figs. 5.14 and 5.15, whereas the control schemes are listed in Table 5.3. In these simulations, SG and DG

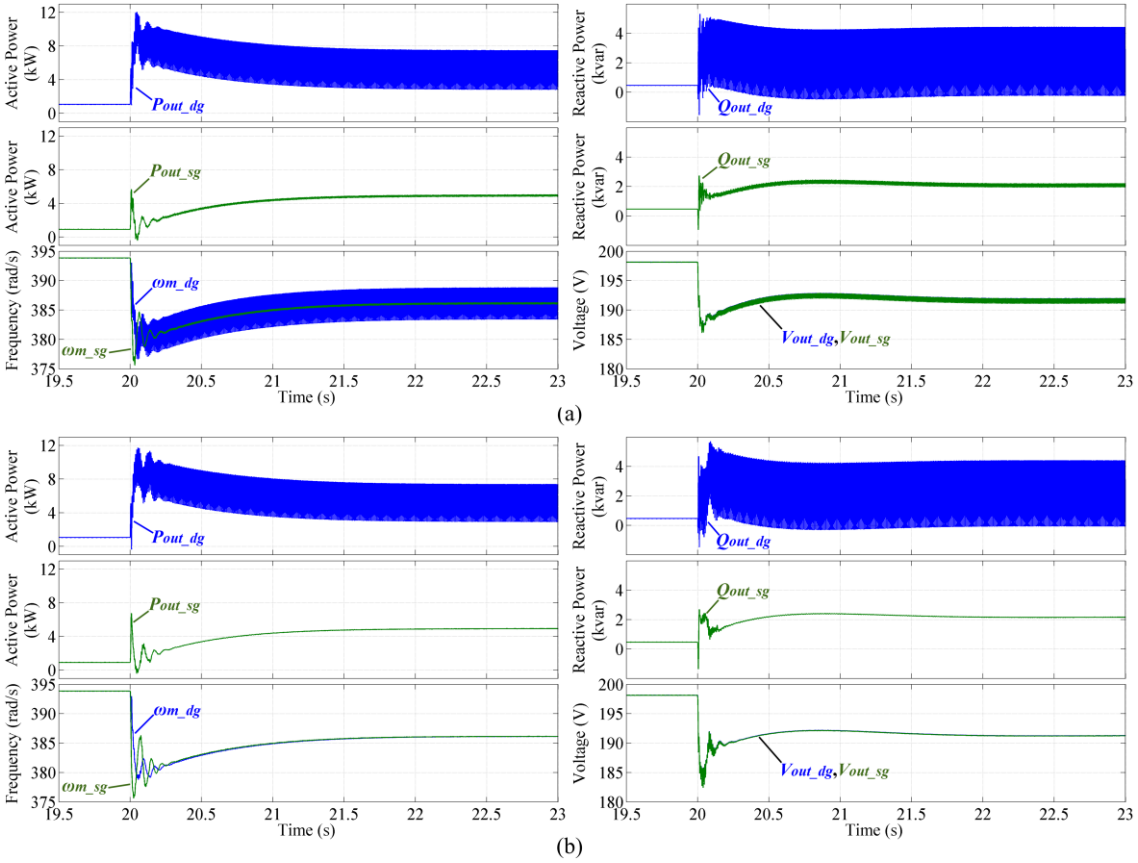

Fig. 5.14 Simulation results with active power and frequency in the left column and reactive power and voltage in the right column. (a) Case A. (b) Case C. (See Table 5.3)

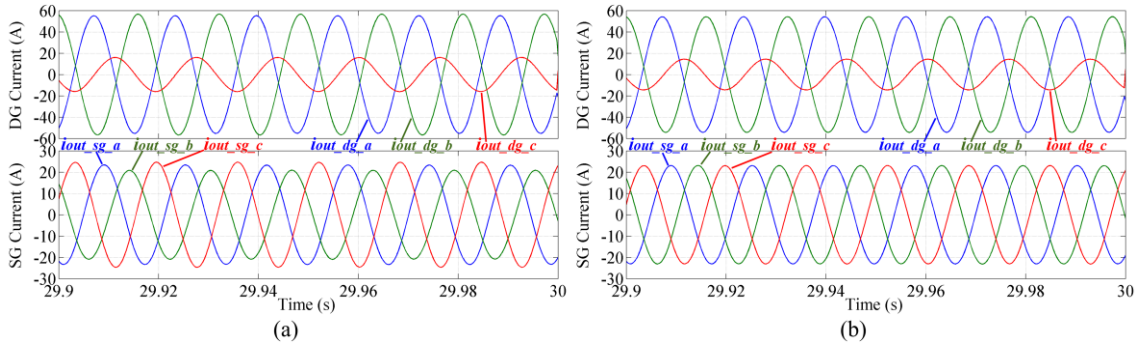

Fig. 5.15 Simulation results of steady-state SG and DG current waveforms.
(a) Case A. (b) Case C. (See Table 5.3)

Table 5.3 Control Schemes of Simulations

Control Part	Case A	Case B	Case C
Enhanced VSG control (Chapter 4)	✓	✓	✓
DDSRF + New power and voltage calculation	×	✓	✓
SG neg.-seq. compensation	×	✓	✓
Transient virtual stator impedance	×	×	✓

operate in parallel with an initial three-phase load of 2 kW, 1 kvar. At 20 s, a single-phase load of 9.6 kW, 4.2 kvar is connected. To be compared with the simulation results of the case of single SG operation discussed in Section 5.2, all loads are doubled compared with the corresponding loads mentioned in Section 5.2.

As it is shown in Fig. 5.14(a), without the proposed modification discussed in this chapter, slight ripples can be observed in the SG active and reactive power after the single-phase load is connected, due to a three-phase unbalance. This unbalance can be further confirmed in the steady-state SG current waveforms shown in Fig. 5.15(a). Moreover, due to the ripples in calculated active and reactive power, ripples can be observed in frequency and voltage of the DG, as well as those of the SG. These problems can be solved by the proposed DDSRF decomposition, the modified power and voltage calculations based on only positive-sequence components shown in (5.2)–(5.4), and the proposed SG negative-sequence current compensator, as shown in Fig. 5.14(b). The steady-state current waveforms of this case are shown in Fig. 5.15(b), in which no three-phase unbalance is observed in the SG current.

Furthermore, by comparing the simulation results of parallel operation of SG and VSG with the proposed modified VSG control shown in Fig. 5.14(b) with those of the single SG operation shown in Fig. 5.3, it can be observed that the SG rotor speed deviation is improved tremendously by the presence of the VSG. The 4.8 kW, 2.1 kvar single-phase load causes a transient rotor speed drop down to around 330 rad/s in Fig. 5.3, but when a doubled loading transition occurs during the parallel operation of SG and VSG, the minimum frequency is still higher than 375 rad/s. Moreover, by

comparing the SG current waveforms shown in Fig. 5.4 with those in Fig. 5.15(b), it is clear that the unbalanced SG current is compensated properly by the DG equipped with the proposed modified VSG control.

5.5.2 Large Loading Transition

Simulation results of a large three-phase loading transition from 2 kW, 1 kvar to 15 kW, 3 kvar are shown in Fig. 5.16, to illustrate the effectiveness of the current limiting method via the transient virtual stator impedance.

As it is shown in Fig. 5.16(a), without the transient virtual stator impedance, the maximum output active power of DG reaches up to 13.59 kW during the loading transition. This overshoot is limited to 11.83 kW when the transient virtual stator impedance is applied, at the cost of slightly larger transient voltage deviation, as it is depicted in Fig. 5.16(b). As a result, with the proposed modified VSG control, current stress imposed on the power devices of the DG during a large loading transition can be significantly alleviated.

5.6 Conclusion

Parallel operation of a SG and an inverter-interfaced DG in an islanded microgrid was studied in this chapter. A modified VSG control was proposed for the DG based on DDSRF decomposition and SG negative-sequence current compensation to establish an operation method under unbalanced loading condition. Transient virtual stator impedance was introduced to prevent overcurrent of the

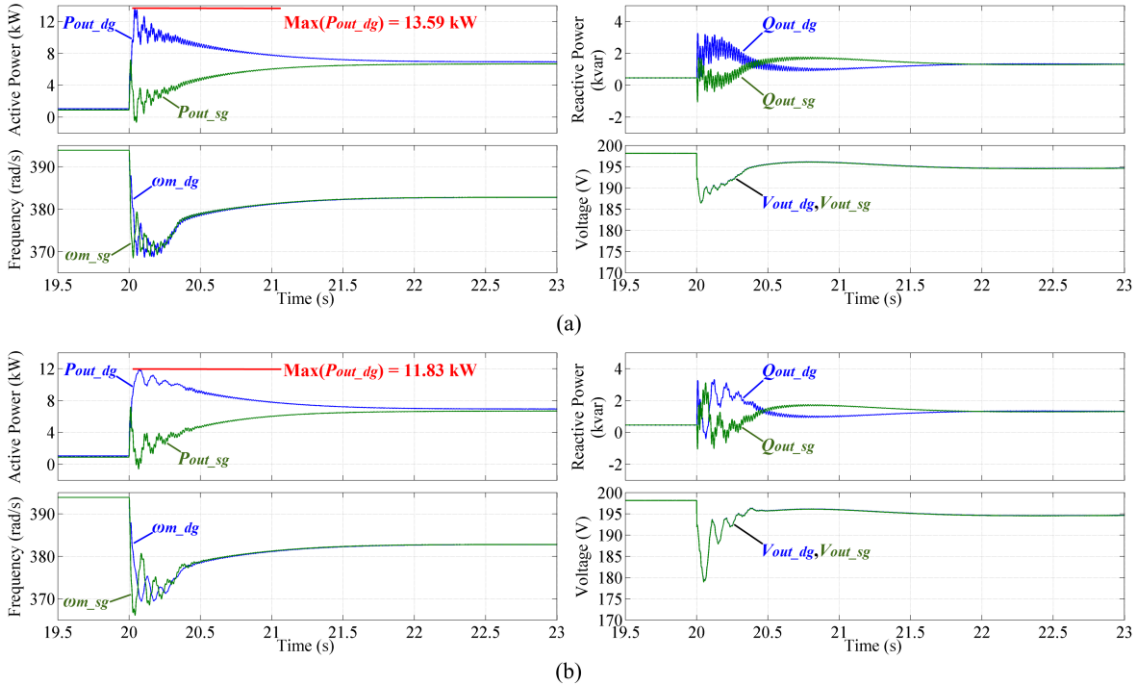

Fig. 5.16 Simulation results with active power and frequency in the left column and reactive power and voltage in the right column. (a) Case B. (b) Case C. (See Table 5.3)

inverter. Tuning methods of main parameters of VSG control were discussed from analytic viewpoints. Simulation results proved that DG with the proposed VSG control can alleviate SG rotor speed deviation, eliminate unbalance of SG output current, and limit active power overshoot during a large loading transition.

References

[1] Y., Banjo, Y. Miura, T. Ise, and T. Shintai, "Enhanced stand-alone operating characteristics of an engine generator interconnected through the inverter using virtual synchronous generator control," in *Proc. Int. Conf. Power Electron.*, 2015, pp.1003–1010.

[2] A. D. Paquette, M. J. Reno, R. G Harley, and D. M. Divan, "Sharing transient loads: causes of unequal transient load sharing in islanded microgrid operation," *IEEE Ind. Appl. Mag.*, vol. 20, no. 2, pp. 23–34, Mar./Apr. 2014.

[3] A. D. Paquette and D. M. Divan, "Virtual impedance current limiting for inverters in microgrids with synchronous generators," *IEEE Trans. Ind. Appl.*, vol. 51, no. 2, pp. 1630–1638, Mar./Apr. 2015.

[4] Y. Hirase, O. Noro, E. Yoshimura, H. Nakagawa, K. Sakimoto, and Y. Shindo, "Virtual synchronous generator control with double decoupled synchronous reference frame for single-phase inverter," *IEEJ J. Ind. Appl.*, vol. 4, no. 3, pp. 143–151, May 2015.

[5] J. Machowski, J. Bialek, and J. R. Bumby, *Power System Dynamics and Stability*. New York: John Wiley & Sons, 1997, pp. 141–182.

Chapter 6

Conclusions

In this dissertation, VSG control was applied to inverter-interfaced DGs, in order to provide inertia support and to improve the frequency stability in microgrids. The basic operation methods of parallel VSGs and a VSG paralleled with a synchronous generator were established through the studies in this dissertation.

In Chapter 2, the principles of the basic VSG control were described, and a brief survey of other existing control schemes providing virtual inertia for inverter-interfaced DGs were presented.

In Chapter 3, VSG control was compared with droop control, which is a conventional microgrid control method, to show the improved frequency stability introduced by the VSG control. Meanwhile, an improved droop control with virtual inertia, called inertial droop control, was proposed based on analogous analyses.

In Chapter 4, issues on parallel operation of VSGs such as the active power oscillation, inappropriate transient active power sharing and reactive power sharing error were addressed. An enhanced VSG control based on stator impedance adjuster and bus voltage estimator was proposed. The simulation and experimental results demonstrated that all these issues can be properly addressed by the proposed enhanced VSG control.

In Chapter 5, a modified VSG control was proposed to address the issue of parallel operation of a VSG and a SG under unbalanced loading condition. Double decoupled synchronous reference frame (DDSRF) decomposition and SG negative-sequence current compensation were proposed to eliminate the negative-sequence current of the SG, and transient virtual stator impedance was introduced to prevent overcurrent during a large loading transition. Simulation results demonstrated that these problems can be properly solved by the proposed modified VSG control, and the presence of VSG alleviates the deviation of SG rotor speed during a loading transition.

The basic ideas and control methods proposed in this dissertation may contribute to the development of microgrids and the integration of inverter-interfaced DGs. With the presented enhanced inertial microgrid control strategies, a “greener” and “smarter” future distribution network with high penetration rate of DGs using RES can be expected.

Still, there are several issues and challenges to be solved on the topic of operation of VSGs in microgrids. For example, if the sharing of unbalanced and harmonic current between parallel VSGs needs to be considered, the enhanced VSG control proposed in Chapter 4 should be further developed. For a microgrid composed of multiple SGs and multiple VSGs, the VSG control method proposed in Chapter 5 also needs to be further developed, as the sharing of negative current between VSGs should be addressed. Moreover, the swing equation parameters of VSGs in microgrids may be optimized by applying modern control theories. Besides, the operation of the VSG-control-based

microgrids under a fault condition is also to be analyzed and discussed. In addition, principles of swing equation may also stimulate new ideas in reactive power control part, which lead to better transient voltage and reactive power performances.

Acknowledgments

I would like to take this opportunity to express my best gratitude and appreciation to all the people who have helped me during the doctoral course study at Osaka University.

First, I would like to express my deep gratitude to my supervisor, Professor Toshifumi Ise in the Graduate School of Engineering, Osaka University, for his continuous support for my researches, for his appropriate guidance, and for his immense knowledge. I also present my sincere appreciation to Dr. Yushi Miura, associate professor in the Graduate School of Engineering, Osaka University, for his kindness, patience, and valuable advices on both my researches and daily life. Without the persistent help from my supervisors, this dissertation would not have been possible.

My sincere thanks also go to Professor Shigemasa Takai in the Graduate School of Engineering, Osaka University, for his careful review on this dissertation and valuable comments.

Besides, I would like to express my thanks to the other members of my dissertation committee: Professor Tetsuzo Tanino, Professor Tsuyoshi Funaki, and Professor Hiroyuki Shiraga in the Graduate School of Engineering, Osaka University, for their insightful comments and encouragement, and for their challenging questions which incented me to widen my research from various perspectives.

I would like to extend my sincere gratitude to Professor Hassan Bevrani in the Department of Electrical and Computer Engineering, University of Kurdistan, Iran, for his helpful advices on my researches and constructive guidance during the co-authoring of a journal paper.

My cordial appreciation is extended to Mr. Jin Yoshizawa and Dr. Kenichi Watanabe in the Core Technologies Development Center, Eco Solutions Company, Panasonic Corporation, for their valuable advices during a collaborative research project.

I am grateful for the help and advices from Dr. Yusuke Hayashi in the Environmental Electronics Institute, Industry and Economics Bureau, City of Kitakyushu, and Dr. Hiroaka Kakigano in the College of Science and Engineering, Ritsumeikan University, who were associate professors in the Graduate School of Engineering, Osaka University.

I would express my thanks to other staff at Osaka university for their helps and supports during the doctoral course study.

My thanks also go to all present and graduated members of Ise laboratory, Graduate School of Engineering, Osaka University, for their friendly helps and supports.

I am grateful to the funding received through the MEXT scholarship to undertake my doctoral course study.

I would like to say a heartfelt thank you to my parents and parents in law for always believing in me and encouraging me to follow my dreams.

And finally to my wife, Nan Ge, who has been by my side throughout these years. Without your love, support, sacrifice and encouragement, I would not have had the determination and the courage to embark on this journey in the first place.

List of Publications

Journal Publications (with review)

[1] Jia Liu, Yushi Miura, and Toshifumi Ise, "Comparison of dynamic characteristics between virtual synchronous generator and droop control in inverter-based distributed generators," *IEEE Transactions on Power Electronics*, vol. 31, no. 5, pp. 3600–3611, May 2016.

[2] Jia Liu, Yushi Miura, Hassan Bevrani, and Toshifumi Ise, "Enhanced virtual synchronous generator control for parallel inverters in microgrids," *IEEE Transactions on Smart Grid*, doi: 10.1109/TSG.2016.2521405.

Papers Presented at International Conferences (Oral presentation, with review)

[1] Jia Liu, Yushi Miura, and Toshifumi Ise, "Dynamic characteristics and stability comparisons between virtual synchronous generator and droop control in inverter-based distributed generators," in *Proceedings of International Power Electronics Conference (IPEC-Hiroshima)*, Hiroshima, Japan, 2014, pp. 1536–1543.

(Poster presentation, without review)

[1] Jia Liu, Yushi Miura, and Toshifumi Ise, "Parallel operation of virtual synchronous generators in a microgrid," presented at Aalborg 2015 Symposium on Microgrids, Aalborg, Denmark, 2015. [Online]. Available: http://microgrid-symposiums.org/wp-content/uploads/2015/09/Liu_Miura_Ise-poster_Aalborg2015.pdf

Papers Presented at Domestic Conferences (Oral presentation, without review)

[1] 劉佳，三浦友史，伊瀬敏史："インバータ連系分散電源における仮想同期発電機とドループ制御の動的特性および安定性の比較" 電気学会電力技術・電力系統技術・半導体電力変換合同研究会，PE–14–029，PSE–14–029，SPC–14–064，pp.13–18 (2014)

[2] 劉佳，三浦友史，伊瀬敏史："仮想インピーダンスによる仮想同期発電機の振動抑制方法" 電気学会電力技術・電力系統技術合同研究会, PE–14–124, PSE–14–124, pp.45–50 (2014)

[3] 劉佳，三浦友史，伊瀬敏史：“低圧配電網における仮想同期発電機の振動抑制および無効電力制御” 平成 27 年電気学会全国大会，7–089，pp.136–137 (2015)

Papers Presented at International Conferences (Co-author, with review)

[1] Bin Wu, Jia Liu, and Fang Zhuo, “The Micro-Grid fast simulation platform exploitation based on PSCAD,” in *Proceedings of 26th Annual IEEE Applied Power Electronics Conference and Exposition (APEC)*, Fort Worth, TX, USA, 2011, pp. 1737–1742.

[2] Yaoqin Jia, Dingkun Liu, and Jia Liu, “A novel seamless transfer method for a microgrid based on droop characteristic adjustment,” in *Proceedings of 7th International Power Electronics and Motion Control Conference (IPEMC)*, Harbin, China, 2012, pp. 362–367.

Patents

[1] Jia Liu, Yong-Qiang Lang, and Yu-Yang Mao, “Control device and control method during bypassing of power units,” U.S. Patent 8 942 015 B2, Jan. 27, 2015.